Ultrafast Nonlinear Optical Response of Low-Dimensional Semiconductors

Dissertation

zur
Erlangung des Doktorgrades
der Naturwissenschaften
(Dr. rer. nat)

dem Fachbereich 07
der Justus-Liebig-Universität Gießen

vorgelegt von

Felix Schäfer

aus
Marburg

Gießen, 2024

Vom Fachbereich 07 Mathematik und Informatik, Physik, Geographie der
Justus-Liebig-Universität Gießen als Dissertation angenommen am: 11.12.2024

Erstgutachter: Prof. Dr. Sangam Chatterjee
Zweitgutachter: Prof. Dr. Marina Gerhard

Tag der mündlichen Prüfung: 14.02.2025

Für Annelie und Lina

Abstract

This thesis investigates charge carrier dynamics and the nonlinear optical response of semiconductor heterostructures and monolayer transition metal dichalcogenides. For this purpose, an optical pump - optical probe setup was designed and constructed from scratch to study linear absorption and its changes as a function of various optical excitation conditions.

In my first project, I examine the dynamics of optical gain in a type-II semiconductor heterostructure, analyzing its behavior before, during, and after stimulated emission. To this end, I use a first optical pump pulse to excite charge carriers which in turn leads to gain inside the sample. A second optical laser pulse, resonant with the optical gain in the media, is then used to deplete the generated gain, and a third laser pulse generates white-light to probe the change in absorption on a picosecond time scale. I measure the dynamics of the excitation-induced changes in absorption under several excitation conditions. Type-II heterostructures possess certain advantages as active media in semiconductor laser devices due to their ability to provide spectrally broad, temperature-stable, and efficient gain, along with the potential for electrical injection pumping. The inherent charge carrier relaxation dynamics of active media inside semiconductor lasers impose limitations on the maximum achievable repetition rates, surpassing any constraints imposed by cavity design or heat dissipation. A recovery time of 5 ps is determined, establishing the theoretical limit for the maximum laser repetition rate achievable with this material system, which falls within the range of 100 GHz. These measurements pave the way for future semiconductor laser systems with high-repetition rate lasers tailored for technology sectors such as industry, medicine, or telecommunications.

In the second project of this work, I extend an optical pump - optical probe setup to perform polarization-sensitive measurements on another type-II semiconductor heterostructure that exhibits a charge-transfer exciton (CTX) resonance in its linear absorption. To measure the optical Stark effect on the CTX resonance, I use an optical pump pulse with an energy slightly lower than that of the CTX, ensuring that no excitons are generated. When the pump pulse is detuned 4.8 meV below the charge-transfer exciton resonance, the direct excitonic resonance shows either a redshift or a blueshift depending on the polarization configuration. In contrast, the CTX resonance always exhibits bleaching and a blueshift, regardless of whether co- or counter-circulary polarized excitation pulses are used.

In the third project, I measure the dynamic Rabi splitting of the absorption in a semiconductor heterostructure and a $MoSe_2$ monolayer on a subpicosecond time scale. Rabi splitting, a basic phenomenon of light-matter interaction in a two-level system, occurs when an intense laser field drives the system into resonance. This is achieved using by optical pump - optical probe setups and spectrally tailoring the excitation pulse, allowing for resonant and spectrally narrow excitation of a type-I semiconductor heterostructure as well as a $MoSe_2$ monolayer. In the time domain, a temporal oscillation is detected on the higher-energy branch of the heterostructure, which depends on the excitation density and photon energy. During the interaction of the pump pulse with the multiwell sample, a coherent gain signal at the $1s$ resonance is present.

Contents

List of Figures

List of Abbreviations

AC	alternating current
AFM	atomic force microscope
CB	conduction band
CCD	charge-coupled device
CT	charge transfer
CTX	charge-transfer exciton
DC	direct current
e	elementary charge
E_b	exciton binding energy
eV	electron volt
FWHM	full width at half maximum
FWM	four-wave mixing
GaAs	gallium arsenide
GaAsSb	gallium arsenide antimonide
GaAsP	gallium arsenide phosphide
GaSb	gallium antimonide
GaSe	gallium selenide
GaP	gallium phosphide
GaInAs	gallium indium arsenide
GaNAs	gallium nitride arsenide
Ge	germanium

HDD	hard disk drive
HF	Hartree-Fock
hh	heavy-hole
HR-XRD	high-resolution X-ray diffraction
lh	light-hole
MBE	molecular beam epitaxy
MQW	multiple quantum well
ML	monolayer
MOVPE	metal-organic vapor phase epitaxy
OPA	optical parametric amplifier
OPOP	optical pump - optical probe
QD	quantum dot
QW	quantum well
PDA	photodiode array
PL	photoluminescence
ROI	region of interest
SBE	semiconductor Bloch equations
SHG	second-harmonic generation
Si	silicon
TMDCs	transition metal dichalcogenides
TPA	two photon absorption
THz	terahertz
VB	valence band

1 Introduction

Semiconductors such as silicon (Si) or gallium arsenide (GaAs) have become indispensable in today's information age. Without semiconductor technology, there would be no powerful computers, smartphones, or microprocessors. Consequently, they are an integral part of almost everyone's daily life, form the backbone of modern technology, and are becoming increasingly important for our modern society.

Historically, some semiconductor materials have been known since the end of the 18th century [1] but the researchers at this time were unaware of their semiconducting properties. For example, Si and Ge were declared to be metals because they could not be produced in pure form at the time and, thus, had conductive properties. In the 1930s, A. Wilson predicted that in addition to insulators and conductors, there must also be semiconducting materials [2], which accelerated research into semiconductors and improved production methods. By the 1940s, the degree of purity was high enough to produce p-n junctions from semiconductors. Subsequently, electrical components such as semiconductor transistors were employed for processors, ushering in the age of computers. In 1947, J. Bardeen and W. H. Brattain invented a Ge-peak transistor [3] and a year later W. Shockley developed a Ge-bipolar junction transistor [4]. For these inventions, all three researchers were awarded the Nobel Prize in Physics in 1956 [5]. These breakthroughs became some of the most significant milestones of the digital age, laying the foundation for modern electronics, including computers, the internet, lasers, smartphones, and other digital devices.

The development processes of such components became more sophisticated, and transistors became smaller and more efficient. In 1965, Gordon Moore postulated the so-called Moore's Law, which states that the complexity of integrated circuits regularly doubles with minimum component costs [6]. This quasi-self-fulfilling law still plays an important role today, but it is becoming increasingly difficult to fulfill. As components become smaller and more complex, the influence of quantum mechanical effects, such as interference and the tunneling of electrons or holes, becomes progressively pronounced.

Semiconductors are essential not only in processors but also in the generation and detection of electromagnetic radiation, such as in lasers and charge-coupled devices (CCDs). Lasers are particularly important for medicine, industry, research and for the internet, where they are used in combination with fiber optic cables to connect continents via underwater networks.

Molecular-beam epitaxy (MBE, 1960s) [7, 8] and metal-organic chemical vapor phase epitaxy (MOVPE, 1980s) [9–11] made it possible to produce semiconductor samples with nanometer-thick layers of different materials, which can exhibit special properties. Many modern optoelectronic devices are made up of hundreds of layers of different materials, only a few nanometers thick, and are based on complicated heterostructures in which the transfer of charge carriers at interfaces plays a crucial role.

This thesis is structured around three main projects:

High-Repetition-Rate Semiconductor Lasers

Semiconductor lasers stand out as arguably the most versatile, compact, and energy-efficient sources of laser light in the present era. In particular, pulsed lasers are gaining increasing significance across all fields, especially for applications requiring extremely fast repetition rates with high peak pulse energy. Notable examples of such applications include materials processing in materials sciences and mechanical engineering [12, 13], surgical procedures in life sciences [14, 15], high-speed telecommunications [16–18], and transient spectroscopy in physical sciences [19, 20].

Significant research activities have been undertaken to develop lasers with ultra-high-repetition rates. Given the pivotal role of gain recovery dynamics in laser media, both theoretical and experimental studies have been conducted in quantum cascade lasers [21] and laser materials based on quantum dots (QD) [22–28]. Quantum dot-based structures have exhibited gain recovery dynamics that allow laser repetition rates beyond 200 GHz [29, 30]. In contrast, fewer experimental studies have been performed on quantum well (QW) structures, where the gain recovery dynamics are generally considered to be slower than those found in quantum dot structures [31–33]. Nevertheless, QW-based semiconductor lasers continue to be the dominant technology in many practical applications. They achieve similar maximum repetition rates and shorter pulse lengths during operation compared to quantum dot-based devices [34–37]. The highest fundamental laser repetition rates of QW-based lasers typically range from 50 to 100 GHz [38, 39], while quantum-dot based lasers exhibit similar orders of magnitude, ranging from 40 to 80 GHz [40–42].

Subpicosecond pulse durations are crucial in order to achieve ultra-high laser repetition rates in the hundred GHz range, making QW-based gain media potentially promising despite their slower gain recovery. Type-II heterostructure-based semiconductor lasers offer appealing features, such as a more flexible band structure engineering, wavelength versatility, and frequently demonstrate very broad gain spectra [43–45]. Nevertheless, the gain recovery dynamics in these type-II QW heterostructures remain mostly unexplored [46].

Optical Coherent Effects in Semiconductor Systems

The investigation of the nonlinear optical response of excitons has been a significant focus in condensed matter physics over the last several decades [47, 48]. Specifically, there has been extensive exploration into the nonlinear optical characteristics of spatially direct excitons. These quasiparticles play a crucial role in the spectral response in the proximity of the bandgap and exhibit notable prominence in low-dimensional systems, such as 2D materials, or in type-I semiconductor quantum well systems. The continuous refinement of these structures' quality has significantly contributed to a deeper understanding of the underlying microscopic physics, as demonstrated in studies such as Ref. [47, 49–51]. In recent developments, high-quality type-II heterostructures have emerged, exhibiting spatially indirect charge transfer excitons as the lowest-energy resonances [52–55].

These heterostructures consist of various materials with different bandgaps, and can create a type-II like band structure at the interface. The type-II samples used in this work feature a CTX transition which is visible in the linear absorption spectrum.

Such typs of structures are used for many laser applications in the near and mid-infrared as active media in W-type semiconductor lasers [43, 44, 56]. In particular, the type-II samples exhibit a broad gain bandwidth [55] while demonstrating lower Auger losses in the constituent materials [57–59]. Previous studies investigating the impact of carrier-order correlation effects have primarily utilized pump-probe experiments on type-I heterostructures [60–63]. Charge-transfer excitons possess a permanent dipole moment due to the spatial separation of the electron and hole wave functions. The CTXs demonstrate a finite coupling between excitons with opposite spins, a characteristic already evident at the Hartree-Fock (HF) level [64]. This coupling is vital for the observed absorption changes when employing opposite circularly polarized pump and probe pulses to investigate the optical Stark effect.

Conversely, in various switching applications, emphasis is placed on fast effects linked to the electric field, such as the quantum-confined Stark effect [65]. This phenomenon finds extensive application in electro-optic modulators [51, 66], optical switches [67, 68] and optoelectronic logic [69].

Coherent Dynamics in Low-Dimensional Semiconductor Systems

The realm of optical coherent effects constitutes a cornerstone in modern physics and technology [47, 70–72]. One of the most fundamental manifestations of light-matter interaction is the characteristic spectral signature termed Autler-Townes splitting. This has initially been observed for optically driven molecules in the gas phase [73]. The interaction of a light field in resonance with the energy difference of a two-level quantum system leads to the splitting of its absorption line into two distinct sidebands. These bands are separated by the Rabi energy. The effect is closely related to the dynamical or AC Stark effect, which results in spectral shifts of the absorption of a two-level system [50, 74–76]. Such Stark shifts occur when the detuning between the light field and the quantum system exceeds the Rabi energy. The Autler-Townes or dynamical Stark splitting prevails when the Rabi energy exceeds the detuning of the driving field [77].

Under the resonant excitation conditions used to measure the Stark effect, the high density of generated electron-hole pairs leads to both collisional broadening and excitation-induced dephasing [78–80]. Therefore, studying absorption line splittings for resonant light fields in solid-state systems, such as semiconductors, presents a significant challenge. The dynamical Stark splitting in semiconductors was first observed in semiconductor microcavity systems as these offer enhanced light-matter interaction on the one hand, while the spectral-filtering effect of the Fabry-Perot cavity prevents the excitation of dissociated electron-hole pairs [81, 82]. The corresponding effect in the time domain, i.e., Rabi oscillations, has been demonstrated on exciton resonances by exciting the heavy-hole resonance and probing the spectrally shifted light-hole resonance [83]. Later, the dynamical Stark splitting could also be observed in a conventional quantum well sample with a specially designed Bragg mirror enhancing the light-exciton interaction [77] as well as in intersubband transitions [84, 85]. Moreover, Rabi or dynamical Stark splitting occurs at exciton resonances under the impact of strong THz fields [86–90].

More recently, Rabi splitting was also observed for transition metal dichalcogenide monolayers (ML) for different cavity designs [91–96]. In addition, an Autler-Townes splitting of the $1s$ exciton resonance has been established in $MoSe_2$ monolayers when driving its intra-excitonic transitions in the infrared wavelength range [97].

2 Theoretical Background

This chapter provides a concise overview of the fundamental physical principles necessary to understand the experimental outcomes observed in this work. Topics covered include the solid-state physics of semiconductors and interactions between light and matter such as AC Stark effect and Rabi oscillations.

2.1 Semiconductors

Semiconductors have assumed a pivotal significance in modern society. Silicon, for example, is integral to the functionality of processors, and materials like lithium niobate ($LiNbO_3$) are used in semiconductor lasers, and those being used to transmit data via fiber optic cables.

Semiconductors are solid materials with electrical conductivity lying between that of conductors and insulators [98]. The electrical conductivity σ depends on temperature. As the temperature approaches zero, σ for intrinsic semiconductors approaches zero [99]. At room temperature, the electrical conductivity of semiconductors ranges approximately from 10^{-2} to $10^{9}\,\frac{\Omega}{\mathrm{cm}}$ [100]. An alternate definition of semiconductors is via their bandgap energy (E_g), the energy difference between the valence and conduction bands in the momentum ($\vec{k}$) space. For a semiconductor this bandgap energy E_g lies between the bandgap of insulators (greater than 4 eV [101]) and conductors, for which bands overlap [102]. Notably, at low temperatures, intrinsic semiconductors, which lack impurity doping, adopt insulator-like characteristics, whereas at room temperature, they manifest conductive traits.

In the realm of semiconductors, various systems can be categorized: zero-dimensional quantum dots, one-dimensional quantum wires, two-dimensional quantum films, and three-dimensional bulk semiconductors. This study specifically explores 2D heterostructure semiconductors.

2.2 Semiconductor Heterostructures

Within the scope of this study, most of the examined samples consist of monocrystalline layers of semiconductor materials stacked on top of each other. These distinct materials were methodically deposited in alternating sequences and different thicknesses in order to grow a heterostructure or quantum well.

2.2.1 Heterostructure Growth Methods

2D heterostructures can be grown by various methods, including molecular beam epitaxy and metal-organic vapor phase epitaxy. The (Ga,In)As heterostructures that are

the main subject of this study were grown using MOVPE [9–11]. In metal-organic vapor-phase epitaxy reactors, the semiconductor material is transported across a heated substrate via a carrier gas. This process involves the deposition of individual atoms of the semiconductor material onto the substrate's surface, facilitated by the thermal decomposition of metal-organic compounds. This gradual process results in the formation of a monocrystalline layer of the semiconductor material on the surface of the substrate [103]. The resulting composition of the layers can be adjusted based on environmental factors, such as temperature, pressure within the MOVPE reaction chamber, and the use of different carrier gases, enabling the creation of diverse semiconductor heterostructures with varying properties. The precision inherent in this technique makes it well-suited for producing semiconductor quantum films with well-defined interfaces [104].

2.2.2 Quantum Wells

In a quantum well, charge carriers are spatially confined by a surrounding potential. For example, in semiconductor heterostructures, potentials are created by inserting a different material between two semiconductor layers. These structures are used in devices such as quantum cascade lasers or diode lasers to generate light.

In a first approximation, a quantum well can be considered analogous to a quantum mechanical particle in a potential well with "infinitely" high barriers. Electrons and holes in a quantum well can move freely in two spatial directions, but the wave nature of the charge carriers must be taken into account.

To calculate the electronic energy levels E_n in a quantum well, the 1D Schrödinger equation is used [105]:

$$\frac{-\hbar^2}{2m}\frac{\partial^2\psi_n(z)}{\partial z^2} + V(z)\psi_n(z) = E_n\psi_n(z) \tag{2.1}$$

Here, $\hbar = \frac{h}{2\pi}$ denotes the reduced Planck constant, m is the effective mass of the particle, $V(z)$ the quantum well potential in the z-direction, derived from the band energies of the semiconductor heterostructure, and $\psi_n(z)$ is the wave function. Due to the boundary conditions of infinitely high barriers on both sides of thw well, a periodic wave function of the form

$$\psi_n = A\sin\left(\frac{n\pi z}{L_z}\right) \tag{2.2}$$

can be used to solve the equation and express the energy as

$$E_n = \frac{-\hbar^2}{2m}\left[\frac{n\pi}{L_z}\right]^2 \text{ with } n = 1, 2, ... \tag{2.3}$$

where L_z is the width of the well, as illustrated in Figure 2.1.

From Equation 2.3, it follows that the energy levels increase quadratically with n, and the wave functions in the z-direction are sinusoidal. The shape of these energy levels is schematically illustrated in Figure 2.1. For the lowest energy level with $n = 1$, the wave function consists of a single positive arc. Increasing the energy to $n = 2$ reveals a complete sine wave. As n increases, more oscillations occur between the barriers of the potential well.

In Figure 2.1 a comparison is made between "infinite" (left) and finite (right) potential barriers of a quantum well. For finite barriers, a portion of the wave function penetrates into the barrier region, where it exhibits an exponential decay.

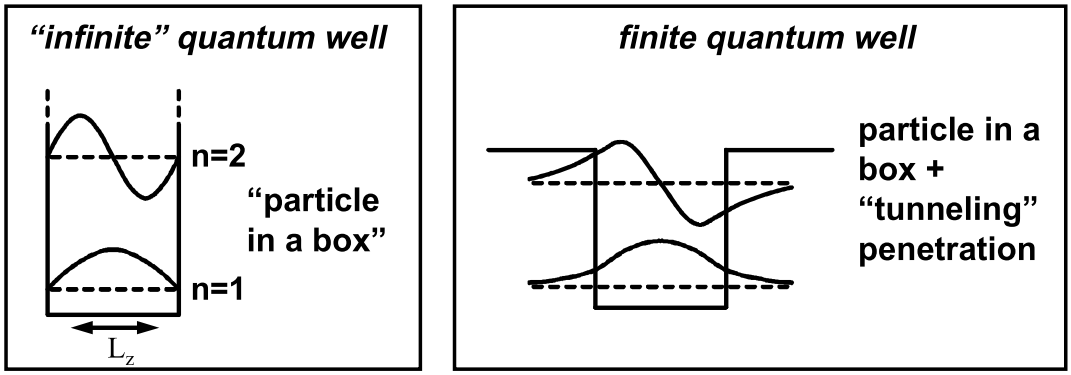

Figure 2.1: Schematic representation of "infinite" and finite high quantum wells with the corresponding wave functions. With "infinite" high barriers the wave function has to be zero at the L=0 and L_z. For finite high barriers the wave function can protrude into the barrier where it exponentially weakens inside it. Adapted with modifications from Ref. [106].

By varying several semiconductor materials while growing the sample, it becomes possible to grow type-I samples with a direct transition (see Figure 2.2 a)). Additionally, type-II structures can be grown, which in the samples used in this work consist of (Ga,In)As and Ga(As,Sb) layers, with GaAs barriers serving as separators between them. The wave functions of electrons and holes are exponentially decaying inside the barrier. However, there is still an overlap with the wave functions of the adjacent quantum wells, allowing for the existence of additional transitions. It can be argued that a hole can "tunnel" from the Ga(As,Sb) layer through the barrier into the (Ga,In)As layer.

Electrons and holes are attracted by the Coulomb force and can form a bound state called an exciton. In the case of type-II heterostructures the quasiparticle with the lowest energy is called the charge-transfer exciton as depicted in Figure 2.2 b).

2.3 Transition Metal Dichalcogenides

Transition Metal Dichalcogenides (TMDCs) are a class of two-dimensional materials characterized by the chemical formula MX_2, where M stands for a transition metal (such as Molybdenum, Tungsten) and X represents a chalcogen (Sulfur, Selenium, or Tellurium) [108]. TMDCs have gained considerable attention in recent years due to their unique electronic, optical, and mechanical properties, which are highly tunable at the monolayer level. Unlike their bulk counterparts, some monolayer TMDCs like MoS_2, WS_2, $MoSe_2$, WSe_2 and $MoTe_2$ [109–112] exhibit direct bandgaps, making them promising candidates for applications in nanoelectronics, optoelectronics, and photonics [113].

Molybdenum diselenide ($MoSe_2$) is one of the prominent members of the TMDC family. In its monolayer form, $MoSe_2$ consists of a single layer of molybdenum atoms sandwiched between two layers of selenium atoms. The Mo-Se bonding within the layer is covalent,

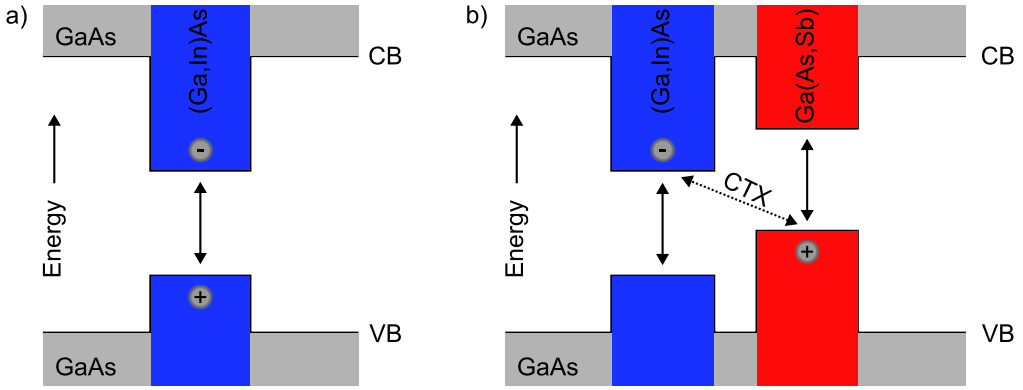

Figure 2.2: Schematic band structure of the semiconductor heterostructures under investigation. a) Type-I (Ga,In)As quantum film, surrounded by GaAs barriers, featuring a spatially direct transition (solid arrow) within the (Ga,In)As quantum films. b) Type-II like sample design made up of two different quantum films separated by thin GaAs layers [107]. Upon optical excitation of the quantum films, charge transfer can occur between adjacent layers. This involves the tunneling/relaxation of holes from the (Ga,In)As valence band into neighboring Ga(As,Sb) layers or electrons from the Ga(As,Sb) layers into adjacent quantum films, seeking a lower energy state. As a result, the semiconductor structure exhibits both spatially direct (solid arrows) and an indirect transition (dotted arrow), which is called the charge transfer exciton.

while the interaction between layers in the bulk form are weak van der Waals forces. This layered structure allows for convenient exfoliation of monolayers [114]. Alternatively $MoSe_2$ monolayer can also be grown by chemical vapor deposition [115].

Monolayer $MoSe_2$ has a hexagonal crystal structure with a lattice constant of approximately 3.29 Å [116]. The transition from bulk to monolayer $MoSe_2$ results in a shift from an indirect to a direct bandgap, with a bandgap energy of around 1.55 eV [117]. This direct bandgap is responsible for strong photoluminescence, making monolayer $MoSe_2$ attractive for optoelectronic applications such as light-emitting diodes (LEDs) and solar cells [113]. Optically, $MoSe_2$ exhibits strong excitonic effects due to the enhanced Coulomb interaction in two dimensions. The A and B excitonic peaks in $MoSe_2$'s optical absorption spectrum correspond to transitions from the split valence band to the conduction band [118].

One of the simplest and most widely used methods to obtain monolayer $MoSe_2$ is the mechanical exfoliation technique, often referred to as the "Scotch Tape method" [119]. This technique was used for exfoliating graphene monolayers, and it has since been adapted for other 2D materials, including TMDCs like $MoSe_2$. In the Scotch Tape method, a bulk $MoSe_2$ crystal is repeatedly cleaved using adhesive tape. Each time the tape is pulled away, it removes layers from the bulk crystal. By pressing the tape with the thin $MoSe_2$ layers onto a suitable substrate (such as silicon dioxide on silicon), and then carefully peeling it off, one can leave behind single layers of $MoSe_2$ on the substrate. It is also possible to grow TMDC monolayers by other fabrication methods, such as MBE and MOVPE [120].

Characterization of $MoSe_2$ monolayers commonly employs Raman spectroscopy to confirm the monolayer thickness by detecting its characteristic vibrational modes. Photo-

luminescence spectroscopy (PL) is also used to verify the material's direct bandgap by analyzing the shape and intensity of the PL peak. Additionally, the temperature dependence of the PL signal provides further insights into the material's properties. Atomic force microscopy (AFM) is also frequently used to measure the thickness and ensure the uniformity of the monolayers [117].

2.4 Light-Matter Interaction

The primary focus of this study is to gain an understanding of the interaction between light and matter. Light is traditionally conceptualized as an electromagnetic wave, with an associated energy of $E = h \cdot f = \frac{h \cdot c}{\lambda}$. In this expression, h is the Planck's constant, f represents the frequency, λ the wavelength of light and c is the speed of light. If this energy is equal or larger than the bandgap energy E_g, it becomes possible for photons to excite the matter, inducing transitions within the material.

The Beer-Lambert law is used to describe the reduction in irradiated intensity as a function of the medium's absorption coefficient and thickness [121]:

$$I(\lambda) = I_0(\lambda) e^{-\alpha(\lambda) L} \tag{2.4}$$

In this equation, $I_0(\lambda)$ represents the incident light's intensity, L is the sample's thickness, and $\alpha(\lambda)$ signifies the absorption coefficient. This equation can be rearranged to determine the product of absorption coefficient and thickness:

$$-\ln\left(\frac{I(\lambda)}{I_0(\lambda)}\right) = \alpha(\lambda) L \tag{2.5}$$

Besides the generation of free electrons and holes in the conduction or valence band, there can also exist electron-hole pairs that are bound together by Coulomb interaction. The binding energy E_B of these excitons can be approximated using a formula analogous to that of the hydrogen atom [122]:

$$E_B = \frac{\mu e^4}{8 h^2 \epsilon^2 \epsilon_0^2} \frac{1}{n^2} \tag{2.6}$$

Here, h denotes Planck's constant, e represents the elementary charge, ϵ_0 stands for the dielectric constant, and n is the quantum number. Considering the existence of excitons in a solid semiconducting material, it becomes crucial to consider for the material's dielectric surroundings, a factor addressed by the permittivity ϵ in the equation.

The effective masses of the electron m_e and hole m_h in the semiconductor are used to calculate the reduced effective mass μ of the electron-hole pair within the medium:

$$\mu = \frac{m_e m_h}{m_e + m_h} \tag{2.7}$$

This assumption allows for the calculation of the binding energy of an exciton. For example, in bulk GaAs, the binding energy is approximately 4.2 meV [123].

When a photon's energy is below the threshold to induce a transition, the sample may absorb two or more photons. If the combined energy of these photons exceeds the bandgap energy, a transition can occur (two photon absorption, **TPA**).

When a sample is excited and an electron is transferred from the valence to the conduction band, it can recombine with the hole in the valence band and can release energy in the form of heat via phonons (thermal recombination) or as photons (radiative recombination) [124]. Various phenomena can broaden and blur this emission line.

2.4.1 Line Broadening

A distinction is made between two types of broadening: **homogeneous** and **inhomogeneous**. In the case of homogeneous linewidth, the emission probability for a specific frequency is the same for all particles in the system. Homogeneous broadening is manifested as a Lorentzian line shape and encompasses phenomena such as pressure broadening, which arises from elastic and inelastic collisions between particles or lifetime broadening of excited states. In contrast, inhomogeneous linewidth is characterized by varying emission probabilities for different particles in the system. The line shape is best described by a Gaussian function and encompasses the optical Doppler effect and time-of-flight broadening. In the context of the measurements conducted within this study, it is primarily the inhomogeneities within the samples that contribute to the observed broadening effects [125].

2.4.2 Ultrafast Optical Excitation of a Semiconductor

A laser pulse can excite a semiconductor, generating a coherent, macroscopic polarization. However, this coherent polarization tends to dissipate within a specific timeframe due to Coulomb interactions and scattering. For a sample temperature of 4 K, this time span is typically on the order of a few picoseconds for excitonic resonances. The dephasing time, which is a measure of the time required for an exciton to lose its phase coherence, is dependent on a number of parameters. These include temperature, crystal structure, energy gap, dielectric function, and electron-phonon coupling [126].

In Figure 2.3 the electron distribution $f(\mathrm{E})$ for four timeframes as well as the band diagram with different scattering mechanisms are shown for a typical bulk III-V semiconductor excited by an ultrashort laser pulse [127]. Following the excitation, the photoexcited electrons and holes go through various nonequilibrium states before returning to thermal equilibrium. Initially, the electronic states retain their coherence for a short timeframe. If the coherence loss occurs faster than other relaxation processes, the carrier distribution remains nonthermal.

Subsequently, energy is redistributed mainly through carrier-carrier collisions, leading to a thermalized distribution with characteristic temperatures T_C for electrons and holes that differ from the lattice temperature T_L. Eventually, the electrons and holes cool down by interacting with phonons and reach the lattice temperature. Finally, the photoexcited carriers recombine on a timescale of several hundred picoseconds, bringing the semiconductor back to thermal equilibrium. It is important to note that the relevant time scales depend on numerous factors, such as carrier density and energy, and often overlap. As a result, the relaxation processes described above do not occur sequentially but rather simultaneously [127].

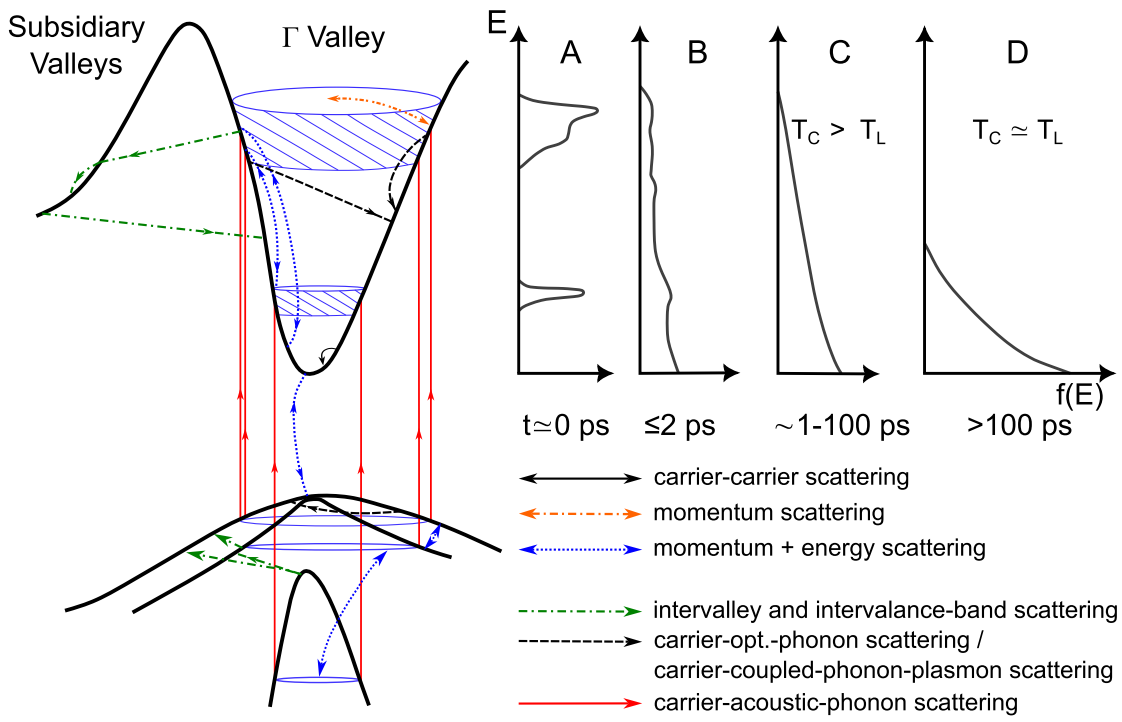

Figure 2.3: Schematic band diagram of a typical bulk III-V semiconductor excited by an ultrashort laser pulse. The energy of the pump laser pulse is such that all three valence bands are excited. Different scattering processes are indicated by arrows. On the right side of the diagram, the initial electron distribution and its temporal evolution are shown. Reproduced from Ref. [127].

2.4.3 Gain / Population Inversion

Population inversion is a fundamental concept in laser physics describing a non-equilibrium condition where a higher energy state in a quantum system is more populated than a lower energy state [128]. In semiconductor heterostructures, population inversion is critical for the operation of semiconductor lasers, quantum cascade lasers, and other optoelectronic devices.

In thermal equilibrium, the population of electrons in different energy states of a semiconductor follows the Fermi-Dirac distribution, where lower energy states are more populated than higher energy states. However, for lasing action to occur, this distribution must be inverted. Population inversion occurs when the population of electrons in the conduction band (higher energy state) exceeds that in the valence band (lower energy state), creating a condition where stimulated emission dominates over absorption.

Mathematically, the condition for population inversion can be expressed as:

$$f_c(E_c) > f_v(E_v) \tag{2.8}$$

where $f_c(E_c)$ and $f_v(E_v)$ are the Fermi-Dirac distribution functions for the conduction band and valence band, respectively, and E_c and E_v are the corresponding energy levels of the semiconductor.

In semiconductor heterostructures, such as quantum wells, quantum wires, and quantum dots, population inversion can be achieved through optical or electrical pumping [129].

For optical pumping, a high-intensity laser is used to excite electrons from the valence band to the conduction band, leading to a redistribution of carriers and, under certain conditions, population inversion. The use of heterostructures enables carrier confinement in low-dimensional systems, enhancing population inversion efficiency and making these structures well-suited for use as pump lasers.

In addition to lasers, population inversion is essential in the operation of optical amplifiers, where it is used to amplify weak optical signals. These amplifiers are integral components in fiber-optic communication systems.

2.4.4 Rabi Splitting

Rabi splitting is a fundamental quantum mechanical phenomenon observed in two-level systems. For instance, in semiconductor samples exhibiting excitonic resonance, interaction with an external field, such as an optical excitation pulse, can cause the absorption [130] or photoluminescence [131] spectrum to split into distinct higher and lower energy peaks. This split into two absorption branches is known as dynamical Stark effect, Rabi splitting or in three-level system as Autler-Townes effect.

Similar to the Zeeman effect, where atomic energy levels split under an external magnetic field, Rabi splitting occurs under the influence of a resonant laser pulse. This splitting is observable during the temporal overlap of pump and probe pulses.

The resulting two levels are at energies $E_1 + \hbar\Omega_R/2$ and $E_2 - \hbar\Omega_R/2$, with Ω_R being the Rabi frequency.

This Rabi frequency Ω_R describes the frequency at which a two-level system (e.g., an electron in a semiconductor) oscillates between two states when exposed to an external electromagnetic excitation, such as a laser field. This frequency is proportional to the strength of the electromagnetic field E and can be expressed as:

$$\Omega_R \propto \mu \cdot E \tag{2.9}$$

where μ is the transition dipole moment.

The excitation power P of a laser field is proportional to the square of the electric field strength E:

$$P \propto E^2 \tag{2.10}$$

Relating this to the Rabi frequency

$$\Omega_R \propto \sqrt{P} \tag{2.11}$$

which is proportional to the square root of the excitation power P. This can be seen in Figure 4.7 b) for a type-II sample resonantly excited at the $1s$ resonance.

The splitting was theoretically calculated for QDs in Ref. [132] and measured on InGaAs/AlInAs MQW samples in Ref. [84].

2.4.5 Rabi Oscillations

When examining two excited states driven resonantly, they can be modeled as a two-level quantum system. Rabi oscillations, a key quantum phenomenon in such systems, describe the periodic variation in the probability of finding the system in a particular quantum state. This oscillatory behavior occurs when the system is subjected to a resonant or near-resonant external field.

Rabi splitting and Rabi oscillations are essentially two sides of the same coin. Rabi oscillations are an analog of the Rabi splitting in the time domain [47]. When a state is split into two states by an external field, it can be observed in the nonlinear absorption [130]. These two states can interfere with each other and undergo periodic transitions between these states, leading to oscillations in the time domain. This should not be confused with coherent oscillations that occur when the probe pulse interacts with the sample before the excitation pulse [133], which have been observed in GaAs-AlGaAs MQW structures [134].

The splitting of the resonance leads to temporal oscillations, which were calculated and experimentally measured in semiconductor quantum wells, as reported in Ref. [83]. However, that study focused only on a narrow energy range of the heavy-hole excitons. In the investigations of the MQWs, a broader energy range was examined and resonantly excited, including the light-hole excitons.

The two-level system is driven resonantly with the energy E_1 and oscillates in amplitude over time, as shown in Figure 2.4 on the right side. The multi-quantum well samples I measured in this work serve as a model two-level system.

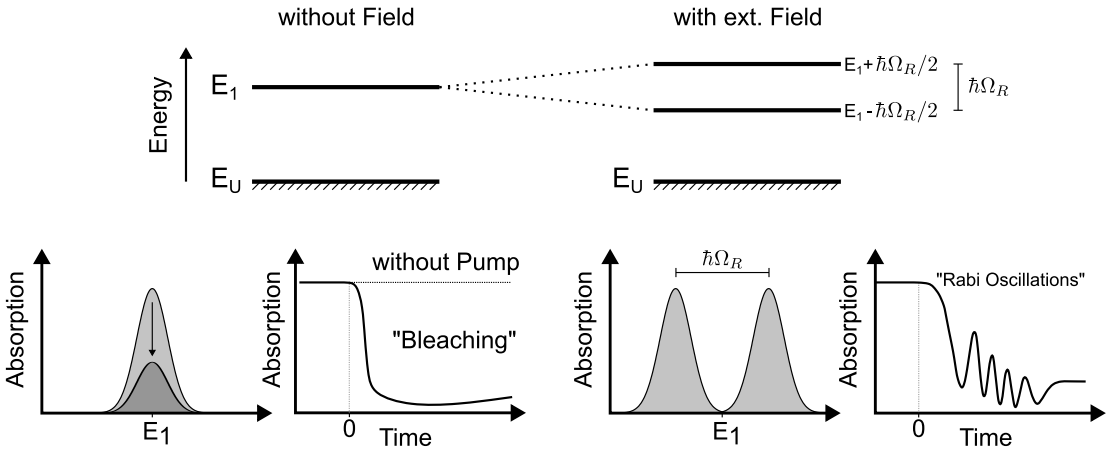

Figure 2.4: Energy level diagram of a two-level system without an external field (left) and with an external field (right), showing the splitting of the E_1 energy level. E_U is the unexcited state in this case. Below the diagrams, the absorption spectrum is illustrated, along with a schematic representation of changes in absorption when the system is resonantly excited. Without the external field, depending on the excitation parameters, bleaching and a slow recovery can be observed. When the two energy levels are separated by $\hbar\Omega_R$ and resonantly excited, Rabi oscillations may occur between the two states.

2.4.6 AC Stark Effect

The AC Stark effect, also known as the dynamic or optical Stark effect [73], describes the shift in energy levels of a quantum system due to interaction with a strong, oscillating electromagnetic field, typically a laser. This effect is crucial in semiconductor heterostructures for understanding light-matter interactions, especially when involving excitons.

Analogous to the DC Stark effect, where a static electric field shifts energy levels, the AC Stark effect involves a time-dependent, oscillating field, often at optical frequencies [47]. When a semiconductor heterostructure is exposed to such a field, the energy levels of the system's excitons are shifted. This shift depends on the intensity of the incident light and the detuning, which is the difference between the photon energy and the energy of the excitonic transition.

In structures like quantum wells or quantum dots, the AC Stark effect is pronounced due to quantized energy levels [106]. This effect is especially significant in systems with strong light-matter coupling, affecting optical properties like absorption, reflection, and photoluminescence.

The AC Stark effect can cause red- or blueshifts in excitonic resonances depending on laser detuning and polarization geometry [135], providing insight into the interaction between excitons and the electromagnetic field.

3 Experimental Techniques & Setup

This chapter provides a detailed overview of the samples and the experimental techniques essential for interpreting the measurement data presented in the subsequent chapter. These techniques were consistently employed throughout the thesis. The discussion begins with the samples, followed by a description of the experimental setups used, as well as the measurement software and data processing methods.

3.1 Samples under Investigation

The linear absorption of the samples was measured using the experimental setups built for this thesis, rather than a separate setup, to ensure the best data quality and to accurately measure absorption at the exact point where the pump and probe pulses impinge on the samples. Various methods were employed to measure linear absorption, tailored to the specific characteristics of each sample.

3.1.1 (Ga,In)As Multiple Quantum Well

The multiple quantum well (MQW) samples were designed and theoretically modeled by the research group of Prof. Dr. Stephan W. Koch[†] in collaboration with the experimentalists Dr. C. Lammers and Dr. M. Stein and were fabricated via MOVPE by the group of Prof. Dr. Volz & Prof. Dr. Stolz (Struktur- und Technologieforschungslabor, STRL) assigned to the University of Marburg.

One of these samples is described in detail in Ref. [52] and has the following specifications measured by high resolution X-ray diffraction (HR-XRD):

The active structure of the type-II MQW consists of (Ga,In)As and Ga(As,Sb) quantum wells, separated by a 1 nm thick GaAs interlayer. One type-II sample contains 3.3% antimony (Sb) composition, while the other contains 7.0% Sb. To compensate for strain, a 19.2 nm thick Ga(As,P) well was combined with a 4.6 nm thick GaAs well [52]. Both type-II samples were fabricated with 50 repetitions of these layers. A third sample, grown in a type-I configuration, lacked the Ga(As,Sb) layer and had 10 repetitions of the other layers. All samples were grown on a 500 µm thick GaAs substrate. Atomic force microscopy analysis revealed a root mean square surface roughness of 0.3 nm. The measured linear absorption, along with a schematic representation of the three MQW samples investigated in my work, is shown in Figure 3.1.

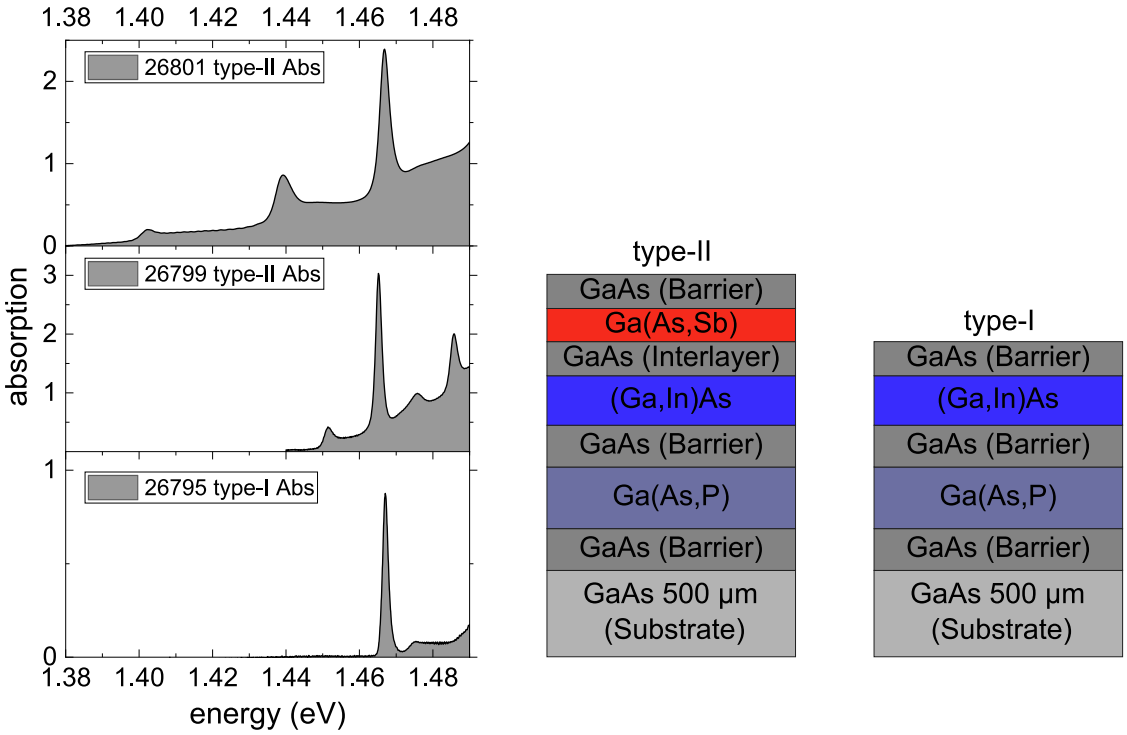

Figure 3.1: Linear absorption of three (Ga,In)As multi-quantum well samples which were used for several measurements. Left side top to bottom: A type-II sample with more Sb used for Paper I; a type-II sample with less Sb for the AC Stark effect in Paper II, each with 50 repetitions of the active layers; a type-I sample without the Ga(As,Sb) well used for Paper III with ten active layers. All feature a distinct absorption peak at 1.465 eV which is the direct (Ga,In)As transition. On the right, a schematic representation of both MQW sample types.

3.1.2 $MoSe_2$ TMDC Monolyer

The sample was prepared using the "Scotch Tape method" method by Marzia Cuccu from Alexey Chernikov's group[1]. In this technique, single layers were carefully peeled from the bulk material using tape and transferred onto a 50 nm thick layer of hexagonal boron nitride (hBN) provided by HQgraphene[2]. This hBN layer was then exfoliated onto a 4.9 mm x 4.9 mm diamond substrate with a thickness of 500 µm, and the TMDC was subsequently covered with an additional 10 nm layer of hBN to enhance the mechanical properties and protect the TMDC monolayer from environmental influences (see Figure 3.2 c)).

Because of the monolayer's limited size and the variability caused by small vibrations, the transmission spectra exhibit fluctuations, highlighting the sample's inherent inhomogeneity. Additionally, scattered light from the diamond substrate complicates the measurement, making it challenging to accurately determine linear absorption using the standard method described in Subsection 3.3.1. To estimate the absorption of the sample, the light transmitted through the sample (see Figure 3.2 a) in gray) with a visible

[1] Dresden Integrated Center for Applied Physics and Photonic Materials (IAPP) and Würzburg-Dresden Cluster of Excellence ct.qmat, Technische Universität Dresden

[2] https://www.hqgraphene.com/

dip in the white-light spectrum was recorded before and after each $\Delta\alpha$L measurement. After calculating the average of the transmitted spectra, an FFT filter was applied to reduce high-frequency fluctuations of the photodiode detector arrays. I fitted the resulting spectra with a polynomial fit (red) excluding the dip from the monolayer. This fit served as the reference light spectrum, which allowed a good estimation of the absorption (black) using Equation 2.5.

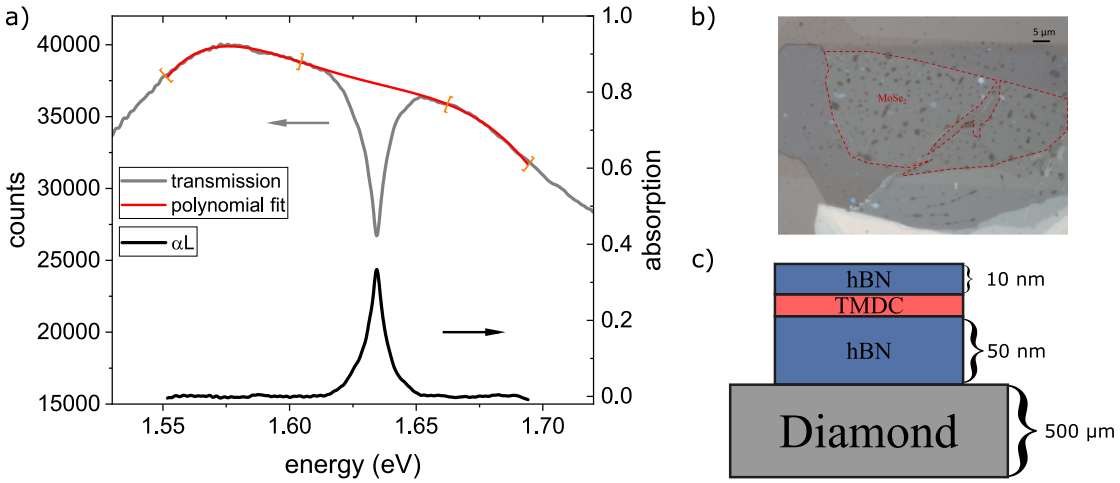

Figure 3.2: a) Transmission spectrum of the $MoSe_2$ monolayer. The transmitted light (gray) exhibits a dip at the excitonic 1*s* resonance. The polynomial fit (red) excludes this dip and acts as the reference spectrum for calculating linear absorption. The fit boundaries are indicated in orange, while the computed linear absorption is shown in black. b) Microscope image of the $MoSe_2$ sample by Marzia Cuccu[1]. The monolayer region is highlighted by a red dotted outline. c) Schematic diagram of the TMDC sandwiched between hexagonal boron nitride layers on a 4.9 mm × 4.9 mm × 500 µm diamond substrate.

3.2 Optical Pump - Optical Probe Spectroscopy

In an optical pump - optical probe (OPOP) experiment, the sample is subjected to an optical laser pulse for excitation, and a low-intensity white-light pulse to measure the transmission characteristics. The use of different mechanical linear stages, and femtosecond laser systems allows the study of the temporal evolution of the excitation with up to femtosecond delay time resolution. The experimental configuration I built is optimized for OPOP spectroscopy in transmission but can also be used to measure the reflection change of the sample. This setup can be used to study the dynamic change of interband absorption of samples as well as excitonic effects. For intraband transitions, optical pump - THz probe (OPTP) experiments can be performed to measure the dynamics of higher conduction band transitions [53, 136, 137].

3.2.1 Experimental Pump-Probe MHz Setup

The initial source of the laser pulses I used for the first study is a regenerative amplifier laser system from Light Conversion[3]. The setup employs a femtosecond laser[4] with a variable repetition rate ranging from a few Hz to a maximum of one MHz. It features a central wavelength of 1030 nm with a pulse duration of 207 fs. The laser has a peak output power of 20 W, of which 15 W is directed into an optical parametric amplifier[5] (OPA).

The OPA enables wavelength tuning of the pump pulse from 650 nm to 900 nm (signal) and 1200 nm to 2500 nm (idler). First, the 1030 nm pump pulse is divided into two branches inside the OPA using a beam splitter: One for second-harmonic generation (SHG) and the other for white-light generation. The SHG pulse is further split into two; one part is combined with the white-light pulse in a first amplification crystal stage. The output from this first amplification stage is then superimposed with the second SHG pulse in a second nonlinear crystal. Finally, a wavelength separator divides the amplified output into signal and idler pulses. For achieving lower wavelengths, two second-harmonic generation crystals can be integrated into the beam path. To obtain a shorter pulse, a compressor can be integrated into the beam path. The chosen pump pulse is focused to a spot size of 250 µm on the sample surface by using lenses to focus the beam before it reaches the sample (see Figure 3.3 orange beam).

The OPA incorporate a BBO crystal to generate frequency doubled light from the 1030 nm pump pulse. This green light with a wavelength of 515 nm serves as the initial excitation source for the sample in Paper I with a spot size of 250 µm on the sample. It follows an additional beam path with an adjustable time offset via an extra linear stage. The excitation beam is passed through an active beam stabilization system[6] to effectively reduce fluctuations due to laboratory temperature, laser instabilities, vibration of the optical stages, and any shifts in the optical path. This first pump pulse is depicted as green beam in Figure 3.3.

The active stabilization guarantees a precise dynamic measurement throughout the experiment. The arrows above the mirrors in Figure 3.3 illustrate the motorized mirrors, which are also equipped with piezo elements behind the mirrors. These, in combination with two detector units, compensate for drift in the laser pulses.

I directed the remaining 5 W of the amplifier pulse through a dedicated stabilized beam path (red lines in Figure 3.3) with a linear delay stage, before being focused into a 4 mm thick water-cooled sapphire crystal, which produces a broad supercontinuum spectrum in the energy range of interest.

The white-light crystal is bonded with silver conductive paint to a metal holder which in turn is inserted into a larger metal block with two perforations for active water cooling. The design of the holder, that accommodates inserts for white-light crystals of various thicknesses, ensures the generation of the broad probe pulse with maximum efficiency and minimal spectral fluctuations due to heating of the white-light crystal. A stable white-light source is critically important for all OPOP measurements.

[3] Light Conversion `https://lightcon.com/`
[4] Light Conversion Pharos
[5] Light Conversion Orpheus-F
[6] TEM Messtechnik GmbH - Alinga 4D BeamLock®System

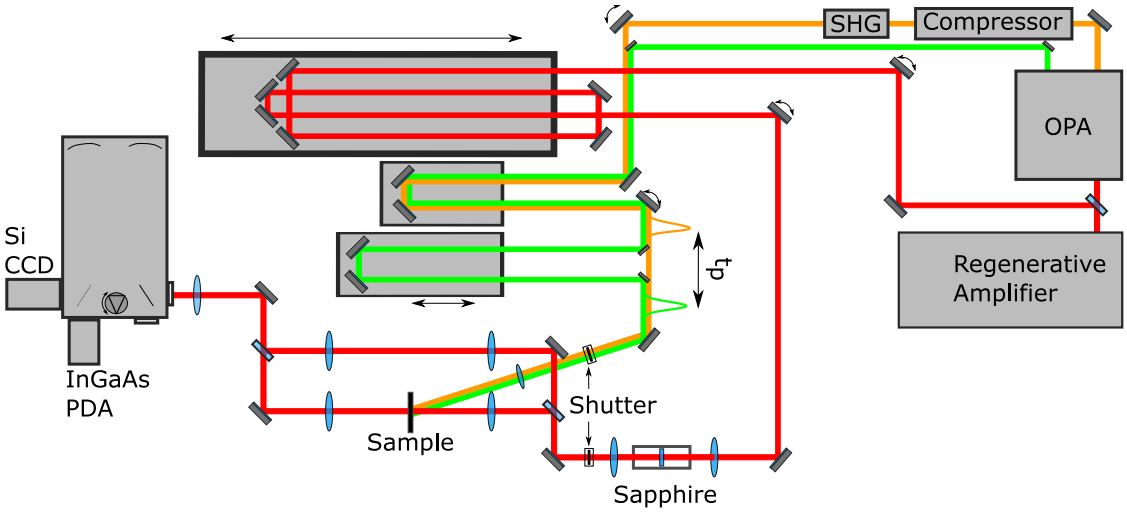

Figure 3.3: Schematic illustration of the experimental optical pump - optical probe MHz setup. The green and orange pulses have an adjustable time delay and are used to excite the sample, while the white-light pulses (red beampath) generated in the sapphire crystal probe the absorption of the sample. The illustration, with some modifications, was used in Ref. [138].

A portion of the white-light is focused onto a 140 µm spot on the sample, which is maintained at a temperature of 4 K in a liquid helium flow cryostat. To prevent the condensation of water or oxygen, a vacuum of approximately $1 \cdot 10^{-9}$ bar is created inside the cryostat using a turbomolecular pump. The other portion of the white-light is redirected by mirrors along a path parallel to the one containing the cryostat to a wedge beam splitter, as shown in the second red path above the sample in Figure 3.3. Here, the beam passing through the sample and the reference beam are aligned to have a small offset in height before entering the spectrometer. As a result, they hit different parts of the CCD chip, so the setup can measure both beams separately.

Both light pulses are focused into a grating spectrometer[7] equipped with three selectable gratings. A grating with 500 $^{1}/_{\mathrm{mm}}$ is used by default. The spectrally resolved light is directed to a Si CCD[8] with 1024 pixels on each of 256 lines. The utilization of multiple lines offers the advantage of capturing various, independent spectra on the CCD chip, enabling the simultaneous measurement of the reference white-light spectrum. A detailed description of this process is available in Subsection 3.3.2 regarding automated measurement routines. The CCDs contain peltier elements to keep the detectors at about -80°C for lower thermal noise. In addition, the reflection from the sample surface can be directed into the spectrometer using another beam splitter. However, this aspect was not further investigated in my work and is therefore not included in the schematic illustration.

Mechanical shutters[9] are positioned in all laser paths. These shutters can be remotely controlled by the measurement computer, which is important for subsequent differential measurements on the samples during the measurement process.

[7] Andor Shamrock SR-500i-D2-SIL
[8] Andor iDus Si DU420A-BEX2-DD
[9] Newport 846HP or HDD Shutter

3.2.2 Experimental Pump-Probe kHz Setup

For Paper II, I used a similar measurement configuration, though utilizing an amplifier system[10] and a fast sCMOS detector[11]. This system operates at a central wavelength of 800 nm, with a fixed repetition rate of 5 kHz delivering an output power of 8 W, with a pulse length of 50 fs. Once again, the output is divided, with 6 W directed into the OPA[12] to generate an excitation pulse wavelength range spanning from 240 nm to 2600 nm. The pump pulse is directed across an Aerotech linear stage[13] with a maximum time delay of 2 ns. Similar to the MHz setup, a beamlock system is employed to stabilize all laser beams.

A pulse shaper is built into the pump path. This shaper uses a grating and a mask to spectrally trim the pump pulse, providing energetically sharp excitation pulses. Because of the pulse bandwidth product, this approach extends the pulse duration and thus the temporal range for observing field effects, which is used in Paper II.

The pulse shaper mask consists of two adjustable razor blades, which, when almost fully closed, result in an excitation pulse with a spectral width of a few nm and a pulse duration of approximately 2 ps. Without the pulse shaper, and depending on the selected wavelength, the pump pulse has a duration of around 50 fs to 200 fs.

Repurposed hard drives in conjunction with an Arduino were employed to develop a cost-effective and rapid shutter system. The Arduino is responsible for switching a H-bridge, which in turn provides 12 V to the hard drives. This supplies power to the electric motor, which is responsible for moving the shutter to the closed position. In the absence of power, the hard drive head moves to the open position due to a magnet. The motors used in hard drives are designed to switch rapidly, with each action taking approximately 50 ms in this use case.

For Paper III the (Ga,In)As measurements were conducted using the kHz amplifier system with spot sizes of 300 µm for the pump and 200 µm for the probe pulse. For the $MoSe_2$ ML the MHz setup was optimized using additional lenses to focus the probe light down to spot size of approx 10 µm to measure only the monolayer.

3.3 Absorption Measurements with OPOP Setups

All absorption measurements were conducted using the two amplifier pump-probe setups described above, which feature white-light crystals as the broadband probing light source for measuring the samples' transmission and for probing light in the OPOP measurements.

3.3.1 Classical Absorption Measurement

A broadband white-light beam is passed through the sample and the spectrum of the transmitted white-light is measured. The sample is then removed from the beam path and only the spectrum of the white-light is measured. Using these two measurements, the

[10] Spectra-Physics Solstice®Ace™
[11] Andor Zyla 5.5 CMOS camera
[12] Topas Twin
[13] Aerotech ACT115DL

Beer-Lambert law (Equation 2.4) allows the absorption coefficient to be calculated. In order to reduce sources of noise, all external light in the lab is turned off and a background spectrum is measured to remove any hot pixels from the CCD.

The linear absorption of the sample $\alpha(\lambda)L$ is then calculated via:

$$-\ln\left(\frac{I(\lambda)-I_{BG}(\lambda)}{I_0(\lambda)-I_{BG}(\lambda)}\right)=\alpha(\lambda)L \tag{3.1}$$

Here, $I_0(\lambda)$ represents the white-light reference spectrum without the sample in the beam path, $I(\lambda)$ is the transmitted white-light spectrum through the sample, and $I_{\mathrm{BG}}(\lambda)$ denotes the background radiation measured with the white-light blocked.

To measure the pump induced change in linear absorption $\Delta\alpha$L, it is necessary to introduce an excitation pulse. This changes Equation 3.1 to:

$$\Delta\alpha L=-\ln\left(\frac{T_{\mathrm{P}}-T_{\mathrm{Pl}}}{T_0-T_{\mathrm{Bg}}}\right) \tag{3.2}$$

In this case, T_{P} is the spectrum of the excited sample when both the white-light and the excitation pulse hit the sample. T_{Pl} is the spectrum when only the pump pulse strikes the sample, which can lead to photoluminescence. T_0 is the transmitted white-light through the unexcited sample. A background measurement T_{Bg} with no laser light hitting the sample can be used to get a smoother signal and to compensate for other light radiation in the laboratory. These separate measurements have to be performed for each time step, using the shutter in the setup.

3.3.2 Differential Absorption with Transfer Function

With the help of a transfer function, only a pre-measurement has to be acquired, and then all shutters can stay open for each time step. The spectra of both pulses (from the reference path & the sample path) are compared, and a transfer function (T_{f}) is calculated to convert the spectrum of the reference pulse (T_{Ref}) into the spectrum of the pulse transmitted through the unexcited sample (T_0). The reference path then provides the spectrum of the unexcited sample, which always has the same white-light fluctuations as the probe pulse through the sample. With the help of the transfer function it is possible to obtain the transmission through the excited sample (T_{P}) and the transmission through the unexcited sample (T_0) simultaneously with one measurement. Before each measurement, the shutters in the experiments are used to obtain the spectra T_{Pl}, which is the photoluminescence of the sample while only the pump pulses impinges on the sample, which is then subtracted from the spectrum of the excited sample (T_{P}). Then all shutters are closed for the background spectrum T_{Bg}.

The differential absorption at each time step with the help of the transfer function is obtained according to:

$$\Delta\alpha L=-\ln\left(\frac{T_{\mathrm{P}}-T_{\mathrm{Pl}}}{T_{\mathrm{f}}\cdot(T_{\mathrm{Ref}}-T_{\mathrm{Bg}})}\right) \tag{3.3}$$

By measuring the transmitted light through the excited sample and the reference path simultaneously, the differential absorption can be calculated for each time step in real time without the need to shutter each path individually, reducing measurement time by a factor of two to three.

3.4 Pump-Probe & Transient Gain Mesurement Software

Accurate pump-probe data is essential for reliable gain measurements, as small spectral features of nonlinear absorption depend on precise measurements of linear absorption in the absence of the pump pulse. Inaccurate measurements can result in misleading signals, such as apparent spectral shifts or artificially high gain. To ensure accuracy, I measured the linear absorption using the same setups, maintaining identical optical components and measurement settings.

Given the significance of accurate sample absorption for gain measurements, a specific procedure can be employed. The pump shutter is kept closed and a pre-measurement is started. Since there is no excitation, the absorption is constant and a zero line is measured. By moving the sample out of the beam path and using the transfer function, the program records the linear absorption of the sample.

For time-dependent signal measurements, a file containing predetermined time steps is used to set the time delays of the white-light and pump pulses according to the specified measurement timeframe. The typical time steps are in the range from a few femtoseconds to picoseconds. The pump stages are able to delay the pulse up to 2 ns. If it is necessary to measure longer delay times, the white-light stages can be used for a delay of up to 22 ns.

The program calculates the change in absorption by using Equation 3.3 and all the spectra measured before. The resulting data is stored in a .sdf file containing all spectra for each time step, which can then be loaded by an evaluation program.

To account for fluctuations in laser output power due to variations in laboratory temperature, at least three consecutive measurements were taken and then averaged. This practice accounts for a complete temperature cycle within the laboratory when measuring around 100 time steps.

3.5 Data Processing and Visualization in LabVIEW

The LabVIEW-based evaluation program can load the .sdf files generated during the measurements. The acquired data is visualized by false-color 2D plots, where the x-axis represents either the wavelength or the energy, and the y-axis represents the time delay or time steps between the pump and the white-light pulse. The false-color scale reflects the signal strength of the change of absorption.

If the measured $\Delta\alpha$L spectra show a shift or tilt above or below zero at energies without absorption prior to excitation, likely due to fluctuations in the white-light source, a zero correction can be applied. This adjustment eliminates the shift, ensuring that these regions are set to a baseline value of zero. Although this should not occur when using the transfer function measurement routine, it could potentially occur when using the shutter method without transfer function at each time step.

Dispersion is the phenomenon where the phase velocity of a wave varies with its frequency [139]. All optical elements exhibit dispersion, meaning their ability to bend or refract light depends on the wavelength or frequency of the light passing through them. A chirp correction procedure can be used if different frequency parts of the probe pulse hit the sample at different times, resulting in a skewed line in the 2D plot. This happens because

the refractive index of light in matter is not the same for all wavelengths. Most optical elements, such as lenses or the cryostat windows, alter the arrival times of light due to the refractive index of the medium.

Additionally, the software includes a history file management to store various parameters such as excitation densities of different measurements, allowing quick comparison. In order to obtain the absorption of the excited samples, it is possible to load the linear absorption measurement and then add it to all $\Delta\alpha$L spectra. This feature is used in particular in Paper I and Paper III to observe and study the dynamic gain spectra as well as the Rabi splitting with oscillation of the higher energy branch.

A 2D false-color plot has the advantage of showing the dynamics of a signal in a single flat graph, but it can be difficult to interpret. Therefore, individual spectra are often extracted from the 2D data set, as shown on the right in Figure 3.4 (horizontal lines). Alternatively, individual transients at a specific energy (vertical lines) can be further examined to understand the temporal evolution.

Unfortunately, depending on the color scale used, some features such as small oscillations on top of an energy shift can be obscured in 2D (see Figure 3.4 on the top left), so viewing the data as a 3D false-color plot can help to observe such effects.

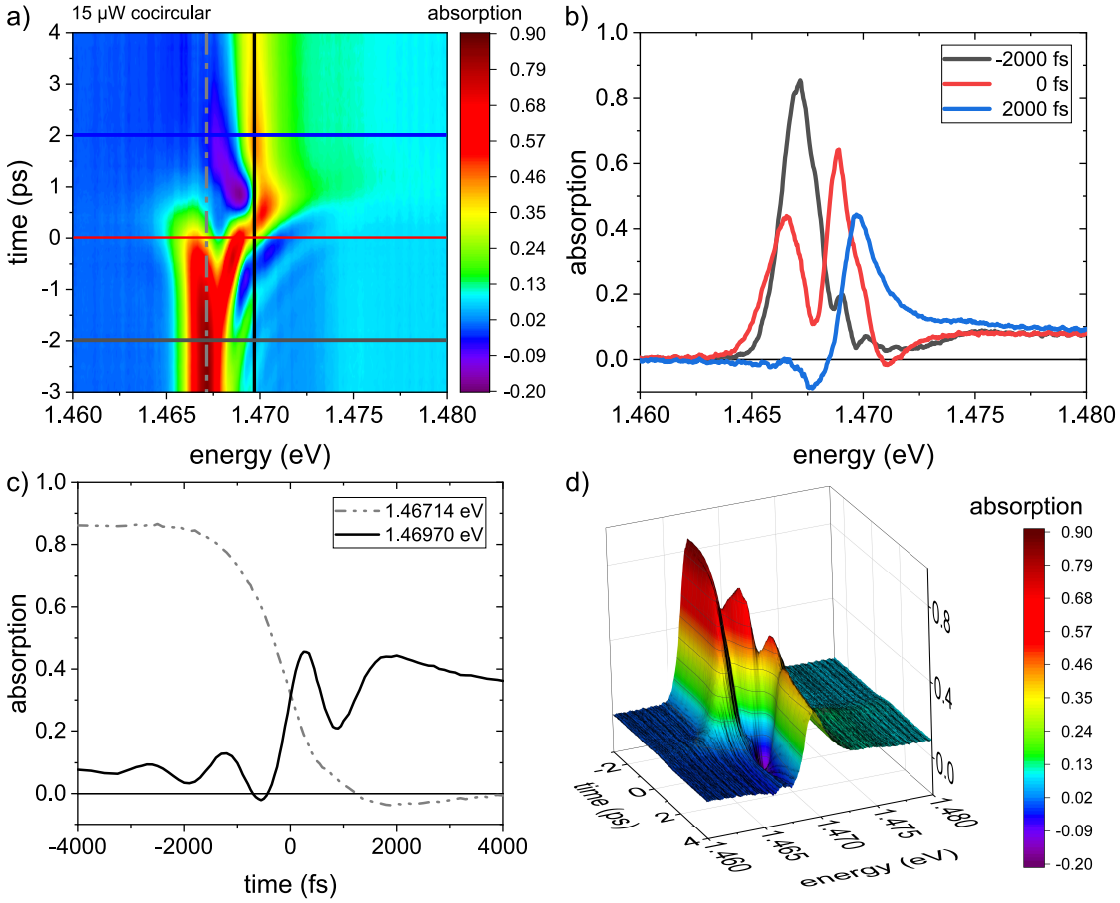

Figure 3.4: a) 2D false-color plot of the absorption of the excited type-I sample ($\Delta\alpha$L + linear absorption) with a photon density of $1.81 \cdot 10^{13}$ Ph/cm^2. In the 2D plot the color scale is tuned so that blue corresponds to transparency, positive values range drom green to red (absorption) and negative values (e.g., gain) are violet.
b) Example spectra from -2000 fs (dark grey), 0 fs (red) and 2000 fs (blue). At -2000 fs, the excitation pulse has yet to reach the sample, so only the linear absorption is observed, accompanied by small coherent oscillations at higher energy levels. At 0 fs the absorption splits into two peaks, and at 2000 fs a gain signal can be observed as well as a shift of the bleached absorption.
c) Transients from an energy of 1.46714 eV (gray dotted line, at the absorption resonance) and 1.46970 eV (black line, 2.56 meV above resonance). The absorption resonance begins to weaken around -2000 fs, eventually becoming transparent between 1200 fs and 4000 fs. The black line approaches near transparency, with oscillations visible from -3000 fs to 1750 fs. After that, a bleached absorption is visible.
d) 3D view of the same data with visible oscillations of the higher energy branch after the Rabi splitting. During the presence of the excitation laser, a negative signal (violet to dark blue) is observed, indicating a strong hyper-Raman gain.

4 Signal Analysis

This chapter provides an overview of various differential absorption signals relevant to the measurements discussed in the peer-reviewed papers. In addition, the data described in the papers will be analyzed, and other measurements not included in the papers will be presented. First, the concept of the data interpretation is given, explaining how the differential absorption signals are generated and how the transition from linear absorption to the absorption of the excited sample can be calculated.

4.1 Differential Absorption Signals

The setups described in Chapter 3 determine the change in absorption of the sample by measuring the excitation-induced transmission change. For the sake of simplicity, the linear absorption is assumed to be a simple Gaussian line shape in this subsection, as shown in Figure 4.1. If the absorption changes when the sample is excited, different characteristic line shape changes can occur. Calculating the difference between linear absorption and the absorption of the excited sample gives the change in absorption. Conversely, summing up the linear absorption αL and the change in absorption $\Delta\alpha$L allows the absorption of the excited sample to be calculated at each time step.

Without excitation, the absorption and linear absorption are the same, and there is no change in absorption; hence, the $\Delta\alpha$L signal is zero. This is also the case if the system is in equilibrium after an excitation.

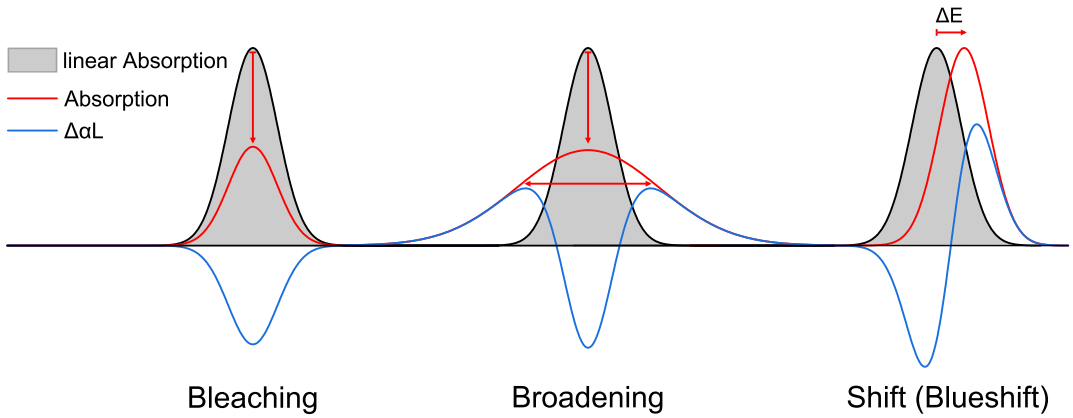

Figure 4.1: Schematic representation of the linear absorption (Gaussian curve in gray), the absorption of the excited sample in red, and the resulting $\Delta\alpha$L signal in blue. The left panel illustrates bleaching, characterized by a reduction in the spectrum's intensity without any shift of the resonance energy. The center panel displays a broadening of the resonance. The right panel depicts a shift of the resonance, specifically a blueshift, indicating a move towards higher energies. Conversely, a shift towards lower energies is a redshift.

Bleaching is observed when the absorption of the sample decreases due to the occupation of states. Since occupied states cannot be reoccupied, and the Pauli-principle forbids electrons with the same quantum numbers, there are fewer free or unoccupied states at the given transition energy. This leads to a decrease in absorption, causing the $\Delta\alpha$L signal to become negative around the resonance, as shown on the left panel of Figure 4.1.

Broadening of the absorption refers to the situation where the absorption becomes broader and has a lower amplitude at the central frequency while the area under the curve, which is often associated with the oscillator strength of the transition, remains constant. This can be caused by e.g., collisions between particles such as photons & phonons due to temperature. The broadening manifests itself in two positive components on either side of the resonance in $\Delta\alpha$L along with a negative component at the resonance center energy (see Figure 4.1 middle).

The exact opposite signal, namely **enhanced absorption** by linewidth narrowing, was measured several nanoseconds after excitation in comparable type-II samples. It was observed that type-I samples did not exhibit this enhanced absorption signal, see Ref. [140] for further analysis.

If the laser field is energetically close to but below an absorption resonance energy, it can **shift** the resonance of the sample. The absorption remains as strong as before, but is shifted to higher or lower energies, depending on the polarization configuration of the pump and probe beam. The $\Delta\alpha$L shows a negative signal (decreased absorption) at lower energies and a positive signal at higher energies in the case of a **blueshift** (see Figure 4.1 right), while in the case of a **redshift** the exact opposite occurs. These signals were observed in Paper II while tuning the pump pulse below the CTX resonance.

Furthermore, **biexcitons**, which are a bound state of two electron–hole pairs, can form depending on the polarization and energy of the excitation laser. These are generally characterized by an increase in absorption (a positive peak in the $\Delta\alpha$L signal), which appears energetically a few meV below the resonance. In addition, trions, bound states with three charged particles (two holes and one electron or two electrons and one hole), can also appear in the $\Delta\alpha$L signal.

4.2 Gain Recovery Dynamics in type-II Semiconductor Heterostructures

The following section discusses the measurements from Paper I, where I investigated a semiconductor heterostructure using the MHz OPOP setup. A prepulse was employed to simulate a laser system with the heterostructure serving as the active medium.

Gain, which refers to the amplification of incident light, plays a crucial role in laser media. Without an active medium, it is impossible to achieve population inversion (see Subsection 2.4.3). The measurement of gain in a material system can be performed by various methods, such as the stripe-length method [141], the Hakki-Paoli method [142], or, as described below, by using a transient pump-probe setup in combination with a linear absorption measurement.

Imagine a type-I semiconductor heterostructure sample has an excitonic resonance at a defined energy that is excited by a pulse of higher pump energy. As a result, the excitonic states become eventually occupied, and the absorption response decreases with increasing

intensity or photon density of the excitation beam. Consequently, the absorption of the excited sample in this energy range approaches zero, rendering the sample transparent to the incident probe light. As the power or photon density increases, the incident light may be amplified and emission (gain) instead of absorption is observed. Gain is indicated when the sum of the linear absorption and $\Delta\alpha$L results in a spectrum that is partially negative.

In measurements involving the type-II heterostructures, I observed that the gain spans across the spectral range from the 1s (Ga,In)As resonance to the CTX, as depicted by the blue curve in Figure 4.2. Within this gain range, a second laser beam is used to selectively perturb the gain. The gain recovery process was then studied by varying the density and excitation conditions of the pump pulse, as described in Paper I. In this experimental setup, the first laser pulse with an energy of 2.4 eV (515 nm) was employed at -165 ps to drive the sample into population inversion. A second laser pulse at 0 ps, specifically tuned to the gain energy, is used to perturb the gain. A third pulse probes the sample, monitors the gain recovery on a femtosecond time scale, and determines the theoretical limits of repetition rates in this material system.

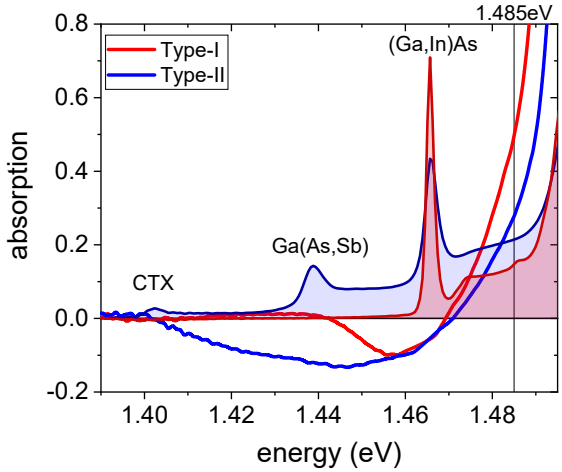

Figure 4.2: Comparison of the absorption of a type-I and a type-II sample excited with an energy of 1.485 eV and identical photon densities. The shaded regions represent the linear absorption of the samples (divided by a factor of five for better visibility) and the absorption of the excited samples ($\Delta\alpha$L + linear absorption). The gain range for the type-II sample extends from the 1s (Ga,In)As resonance to the CTX (blue line). For the type-I sample, however, the gain exhibits lower amplitude and spans a narrower energy range.

Analyzing a series of absorption spectra for the type-II sample of Paper I, captured at various time intervals ranging from -160 ps (5 ps after the **first** pump pulse) to 1.2 ps (1.2 ps after the **second** pump pulse), reveals an intriguing pattern. At -160 ps, the absorption gets weaker because excitonic states are filled, and around -136.5 ps, gain emerges, progressively intensifying until reaching its maximum at -10 ps (as illustrated in Figure 1 (b) of Paper I). 1.2 ps after the impact of the second pump pulse on the sample instantaneous transparency is observed.

Upon closer examination of smaller time intervals just before the second pump pulse interacts with the sample, as well as within the time frame of up to 15.1 ps after the second pulse, it is evident that the gain rapidly collapses (Figure 1 (c) of Paper I). However,

it then undergoes a recovery of the gain signal on a picosecond time scale, eventually converging to the original gain value.

I explore a range of carrier densities in my investigation, spanning from an excitation-induced carrier density of $0.6 \cdot 10^{12}/\mathrm{cm}^2$ to $2.4 \cdot 10^{12}/\mathrm{cm}^2$ from the first pump pulse as shown in Figure 2 (b) of Paper I. At the lower end of this density spectrum, the excitation is so weak that it generates only a minor $\Delta\alpha$L signal, leading to a reduced absorption, as indicated by the red line. As the carrier density increases, the absorption diminishes, and at a level of $0.9 \cdot 10^{12}/\mathrm{cm}^2$, the sample becomes transparent, exhibiting zero absorption within the energy range of 1.435 eV to 1.4 eV (CTX). At the highest experimental excitation level, corresponding to $2.4 \cdot 10^{12}/\mathrm{cm}^2$, I observe a broad gain extending from the CTX at 1.40 eV to 1.49 eV.

To analyze the transient gain response, I focused on the integrated energy range of 1.4 eV to 1.459 eV. The analysis involved varying photon densities for the first pump pulse, ranging from $1.0 \cdot 10^{14}$ to $8.9 \cdot 10^{14}/\mathrm{cm}^2$. For the second pump pulse, the photon density was fixed at $8.4 \cdot 10^{14}/\mathrm{cm}^2$. I applied exponential decay fits to the data collected between 2 ps and 15 ps after the second pump pulse impinged on the sample. This analysis resulted in time constants for the exponential fits ranging from 7 ps to 5 ps. This implies that, for this material system, the upper limit for the repetition rate of lasers built with this material is around 100 GHz. For more detailed information, refer to Fig. 3 (a) and (b) in Paper I.

I detune the second laser pulse to explore whether lower or higher energies enhance the gain signal. The measurements are taken at a fixed time delay of 1.5 ps after the arrival of the second pulse, as shown in Paper I, Figure 4 (a). I observe that when the energy of the second pump is matched to the spectral region of the gain at 1.459 eV, the gain can be effectively depleted. However, some gain persists even when the second pulse is slightly detuned from the peak of the gain spectrum to lower energies. As the detuning is increased to 1.494 eV, the gain depletion becomes significantly less pronounced due to the reduced spectral overlap between the material gain and the second pump pulse. If the second pulse is further detuned to 1.531 eV, entering the absorptive region of the sample, the gain increases. This increase is illustrated by the negative blue line in Figures 4 (a) and 4 (b) of Paper I. This phenomenon can be attributed to the ultrafast thermalization of the additionally injected charge carriers near the band edge. These charge carriers possess only a small excess energy compared to those generated by the first pulse. As a result, they do not require extended cooling periods and immediately contribute to an increase in the occupation levels close to the band edge.

4.3 Optical Stark Effect in type-II Semiconductor Heterostructures

The dynamic Stark effect was first studied as the splitting of atomic energy levels in a strong, optical field [143]. This optical Stark effect can also be explored in the context of excitons or energy levels in semiconductors and was first measured by *Mysyrowciz* [75] and *von Lehmen* in GaAs quantum wells [50].

In general, the optical pump pulse is energetically tuned to a region of the sample that is transparent but close to an excitonic resonance. The strong laser field interacts with the sample. It is crucial that the pump laser pulse is energetically below the observed

resonance, which otherwise could excite charge carriers and lead to bleaching and other signals.

The shift of the absorption persists only for the duration of the laser pulse that induces the field. Therefore, it is advantageous to spectrally shape the laser pulse using a pulse shaper, effectively extending its temporal duration, a technique used in Paper II. This allowed us to extend the laser pulse to a temporal width of 1.04 ps, as shown in Figure 1 (a) in Paper II.

In Figure 1 (b) of Paper II, the linear absorption of a type-II sample is shown in black, while the used pump pulse is depicted in shaded orange. The pump pulse is energetically chosen to be below the CTX resonance, thereby inducing field effects, without excitation.

I conducted two experiments with pump detuning of 5 meV below the CTX resonance. In the first experiment, I used co-circular polarization geometry, where the pump and probe pulses were circularly polarized in the same direction. In the second experiment, counter-circular polarization geometry was used, where the pump and probe pulses were circularly polarized in opposite directions. Figure 3 of Paper II shows the $\Delta\alpha$L signal of a pump photon density series from $3.8 \cdot 10^{13}$Ph/cm^2 to $3.8 \cdot 10^{14}$Ph/cm^2. The 1s resonance of the (Ga,In)As layers shows a redshift or blueshift depending on the polarization, as documented in the literature [135]. For the CTX, however, I only observe a blueshift with a small bleaching, independent of the pump polarization.

Figure 4 of Paper II shows several theoretical data points of the Stark effect for counter-circular polarized pump pulses. The pump pulse used was consistently 6 meV below the CTX, with the CTX binding energy varying in the calculations from 4.7 meV to 6.7 meV. At low CTX binding energies, the first-order contributions dominate, resulting in a net blueshift. Conversely, for high CTX binding energies, the higher-order correlations become important, leading to a redshift of the CTX resonance. At a binding energy of 5.8 meV there is hardly any redshift observed, but rather a bleaching of the resonance. When the binding energy is increased to 6.7 meV, a redshift is observed at the position of the CTX resonance.

Figure 5 of Paper II shows a 2D representation of the dynamics of the $\Delta\alpha$L signals that I measured, as well as the theoretical calculations. The top row shows the co-circular polarization configurations for experiment (left) and theory (right), while the bottom row shows the corresponding counter-circular polarization configurations. For clarity, the minimum value of the differential absorption in all contour plots is normalized to -1. In addition, the lower energy regions of the spectra containing the CTX (left of the dashed line) are scaled up by the factors indicated in the lower left corners for better visibility.

The experimental data exhibits an excellent correspondence with the theoretical predictions regarding the dynamics of the AC Stark shift for both CTXs and type-I excitons, regardless of whether co-circularly polarized or counter-circularly polarized pulses are employed. In the case of counter-circularly polarized pulses, the experimental data indicate a slight delay in the redshift for the type-I transition in comparison to the blueshift observed in the CTX resonance.

Furthermore, a minor discrepancy between theory and experiment becomes apparent at longer delay times. The experimental results show weak spectral features attributed to residual incoherent excitons in the sample, which were not accounted for in the theo-

retical framework. Despite these small deviations, the overall strong agreement between theory and experiment demonstrates the robustness of the theoretical approach. It accurately captures not only the spectral properties but also the detailed temporal dynamics, providing significant insights into the complex nonlinear physics in type-II systems.

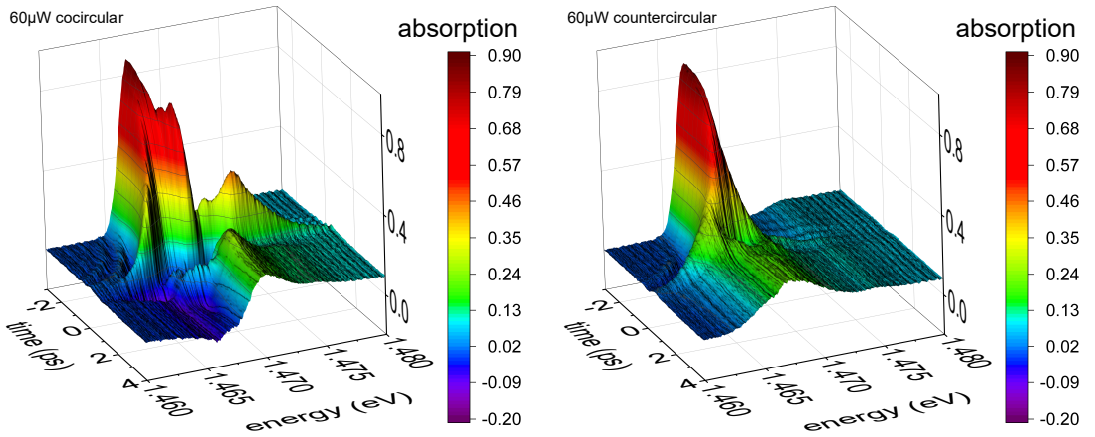

Figure 4.3: A comparison of the absorption dynamics of the (Ga,In)As MQWs for co-circular (left) and counter-circular (right) polarization, measured with the same excitation power of 60 µW (corresponding to $7.23 \cdot 10^{13}$ Ph/cm^2), identical time steps and scaling. In the counter-circular case, bleaching, broadening and a shift of the absorption is observed. In the case of co-circular polarization Rabi splitting at the 1s resonance and Rabi oscillations on the higher energy branches are visible. In the region of temporal overlap of the excitation and probe pulse, gain regions are visible, along with coherent oscillations just before the temporal overlap of the pump and probe pulse.

4.4 Dynamics of Rabi Splitting

The Rabi splitting results presented in this thesis are currently being prepared for publication in Paper III and is submitted to an academic journal. I use the two OPOP setups to measure the dynamics of Rabi splitting in MQWs as well as in a TMDC ML.

4.4.1 (Ga,In)As Multiple Quantum Well

When a sample is resonantly excited, it can exhibit Rabi splitting, where the absorption of the resonance is divided into two distinct peaks. In experiments involving semiconductor heterostructures, the excitation energy must be shifted by a few meV above the resonance peak to achieve a symmetrical splitting. During and after the first interaction of pump and probe pulse (at around 1 ps in Figure 4.3), other phenomena such as Rabi oscillations and bleaching are observed.

Ciuti et al. (Ref. [144]) investigated the dynamics of a 2D electron-hole gas under strong resonant excitation of an exciton resonance. In the study, the interaction with light reduced the Coulomb scattering, leading to the observation of Rabi oscillations and dynamic Stark splitting in the absorption. This work distinguishes between “dressed” and “undressed” states at two specific time points in the measurement: 0.4 ps (referred to as “dressed”) and 4 ps (“undressed”).

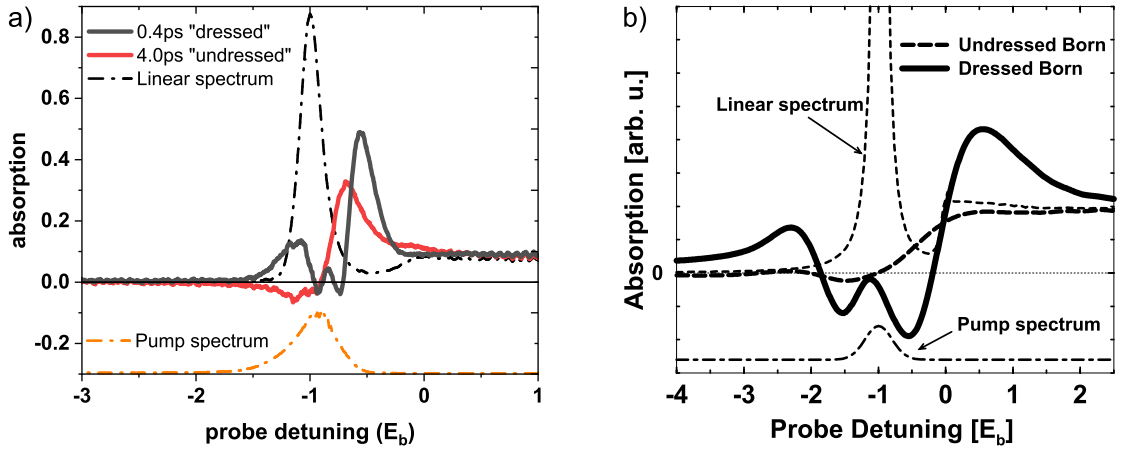

Figure 4.4: a) Measurements of a type-I semiconductor sample with the pump pulse in orange and the linear absorption as a dotted line in black. The spectrum for the dressed signal was taken 0.4 ps after the first change in absorption of the sample. For the undressed signal, a spectrum 4 ps after the pump pulse, i.e., after excitation, is used. b) Theoretical data from Ciuti *et al.* [144]. Similar measurements were conducted on other samples as reported in Ref. [77]. This work specifically studied two polarization geometries, as well as the dynamics of the Rabi splitting.

In Figure 4.4 a comparison of the experimental data I obtained from a type-I sample is shown, presented similarly to Ciuti's data from Ref. [144]. The probe energy range was chosen to ensure that the linear absorption (dot-dash) closely matches the assumed width. The signals are highly comparable, even without any scaling applied, but to investigate the splitting more precisely, detuning series and density series were conducted.

Using several spectra from the data set of the type-I MQW sample (see Figure 4.5 b)), I observe that there is an initial splitting, followed by a short gain signal around the absorption resonance, and a shift to higher energies in the case of co-circular polarization geometry. On the higher energy branch, Rabi oscillations are present in the 2D semiconductor heterostructures. In addition, coherent oscillations can be observed before the temporal overlap between the pump and probe pulses, with the oscillation period increasing as it approaches time zero [133, 134]. Depending on the excitation density, the Rabi oscillations on the higher energy branch oscillate faster, and the shift becomes larger. Additionally, different observations can be made depending on the polarization: In co-circular polarization geometry, there are distinct shifts, oscillations, and gain signals. In counter-circular polarization geometry, there is only a bleaching and small shift of the resonance with no gain and no splitting. Rabi oscillations and dynamical Stark splitting were calculated in the early 2000s [144] and previously measured for semiconductor heterostructures [77].

To achieve a clear splitting of the type-I sample, a pump energy slightly below the resonance was used, as shown in orange in the inset of Figure 4.5 a). The photon density was increased from $1.81 \cdot 10^{11}\,\mathrm{Ph/cm^2}$ (very weak excitation, nearly resembling the absorption seen in blue) to $4.22 \cdot 10^{14}\,\mathrm{Ph/cm^2}$ (red line). The individual spectra were extracted from the 2D false-color plots at each density, taken at the same time point (-300 fs). At a photon density of $6.0 \cdot 10^{12}\,\mathrm{Ph/cm^2}$, the splitting becomes visible. At even higher densities, additional peaks appear symmetrically above and below the resonance.

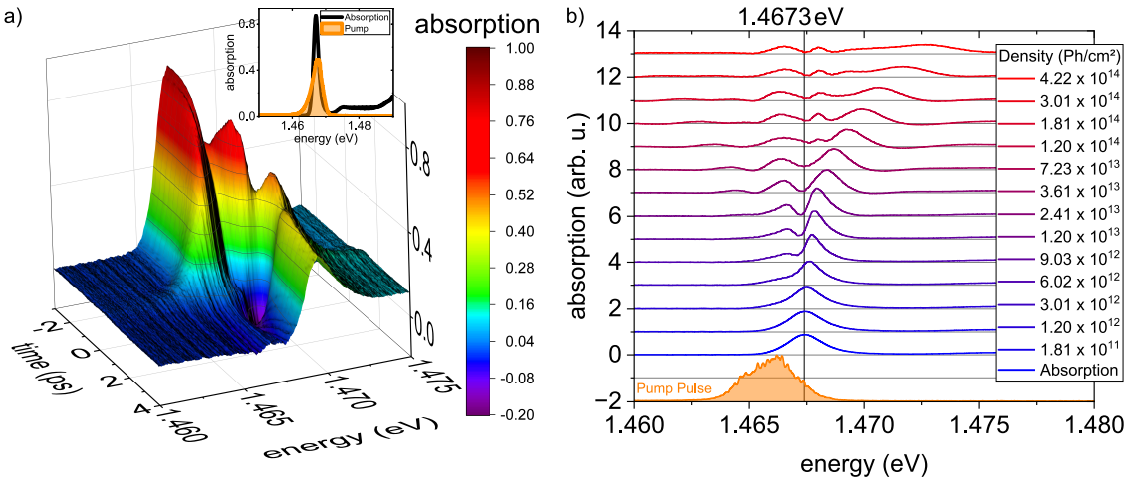

Figure 4.5: a) The 3D visualization of the absorption clearly demonstrates the phenomenon of Rabi splitting in the (Ga,In)As MQW sample. The Rabi oscillations are prominently visible on the higher energy branch, and the onset of negative absorption indicates the hyper-Raman gain. The inset illustrates the linear absorption together with the spectrum of the used pump pulse. b) The absorption is plotted for various excitation densities and a temporal delay between excitation and probing pulse of 300 fs. Rabi splitting appears at a photon density of $6.0 \cdot 10^{12}\,\mathrm{Ph/cm^2}$, with additional absorption peaks emerging at higher pump powers.

By tracing the energy positions of all four peaks against the square root of the excitation power, it is evident that the outermost initial peaks shift linearly away from the resonance with increasing excitation, as shown in Figure 4.6 a). The smaller peaks ±0.8 meV above and below the 1*s* resonance do not shift spectrally with varying excitation power.

In line with Paper I, I investigated the coherent gain region that was measured during the Rabi splitting measurements of the MQW. I integrated the gain region energy from 1.468 eV to 1.469 eV and analyzed the coherent gain using a photon density series ranging from $1.81 \cdot 10^{13}\,\mathrm{Ph/cm^2}$ to $1.81 \cdot 10^{14}\,\mathrm{Ph/cm^2}$. Figure 4.6 b) shows the transient gain measurement of the MQW. The gain has a value of -0.138 at the lowest photon density shown. As the photon density increases, the gain reaches a maximum value of -0.263 at a photon density of $4.83 \cdot 10^{13}\,\mathrm{Ph/cm^2}$. Increasing the photon density to the maximum of this measurement, in this case $1.81 \cdot 10^{14}\,\mathrm{Ph/cm^2}$, the signal loses 20% of its strength to a value of -0.210. This behavior is seen when tracing the maximal gain value against the photon density, which is shown in Figure 4.6 c) as black dots. It is demonstrated that at a photon density of $4.83 \cdot 10^{13}\,\mathrm{Ph/cm^2}$, the gain reaches its maximum and, due to saturation, cannot generate significantly higher gain in this experiment. At high repetition rates of the laser, heating of the gain medium can also prevent effective gain from being generated inside the medium and less laser power output [145].

When examining the transients of the gain, it can also be observed that at the lowest excitation of $1.81 \cdot 10^{13}\,\mathrm{Ph/cm^2}$, the gain reaches its maximum at a time delay of 0.95 ps between pump and probe pulse, see red dots in Figure 4.6 c). Tracing the time of the maximum gain against the photon density shows a temporal shift with an exponential decay to a time value of 0.11 ps.

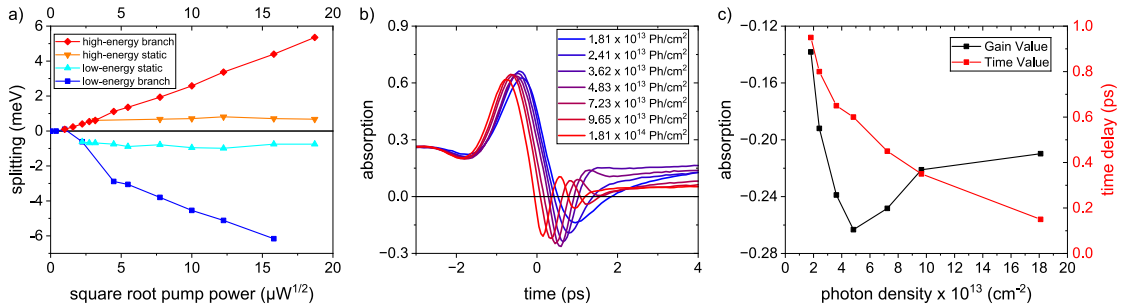

Figure 4.6: a) The splitting of the absorption peaks of the type-I sample is plotted against the square root of the pump power. The high-energy and low-energy absorption peak show a linear spectral shift with the square root of the excitation power. Two additional peaks become visible at a square root power of $3.16\,\mu W^{1/2}$. The positions of the smaller absorption peaks close to the $1s$ absorption peak remains constant. b) Transients of the coherent gain region of the MQW, integrated over an energy range of 1.468 eV to 1.469 eV. As the photon density increases, the gain signal shifts closer to zero time delay. c) Analyzing the peak values shows an increasing gain value with photon density, peaking at $4.83 \cdot 10^{13}\,Ph/cm^2$, followed by a decrease of the value (black line). The red line indicates the time at which the maximum gain occurs. As the excitation increases, the maximum transient gain shifts from 0.95 ps at the lowest excitation to 0.15 ps at the highest photon density.

In measurements of a type-II MQW sample under resonant excitation at the $1s$ excitonic resonance, I observed that the energy separation between the peaks increases proportionally to the square root of the excitation power, as depicted in Figure 4.7 on the next page. The $1s$ resonance is splitting, with the lower energy peak remaining constant and the higher energy peak shifting linearly in response to the square root of the excitation pump power.

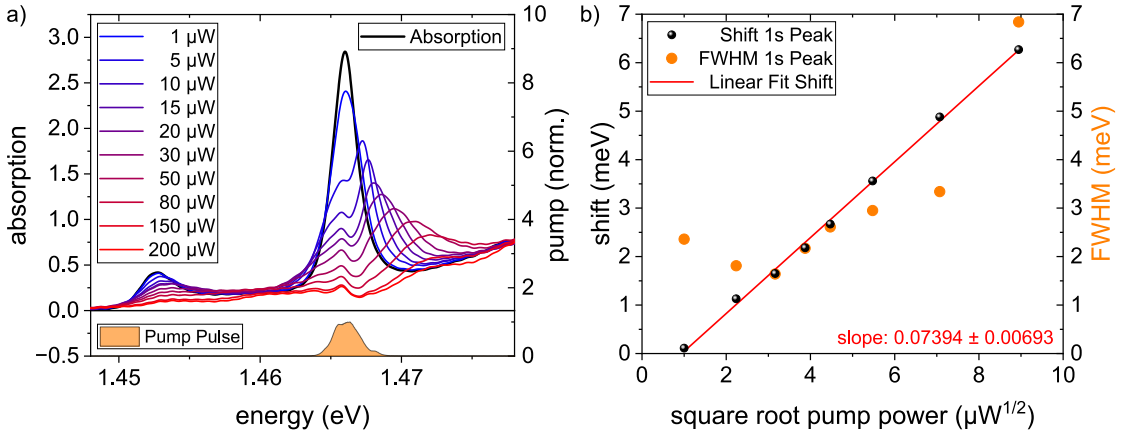

Figure 4.7: a) A pump pulse density series of a type-II multiple quantum well sample, excited at the 1s (Ga,In)As resonance exhibits bleaching, blueshift, and broadening of the resonance. Data were recorded at a nominal 0 ps delay of pump and probe pulse. At lower energies, the CTX undergoes bleaching with a slight blueshift. b) The shift of the 1s (Ga,In)As resonance is plotted against the square root of the excitation power (black dots), revealing a linear trend. Simultaneously, the FWHM of the peak (orange dots) follows the trend, showing almost the same value as the shift.

4.4.2 Monolayer $MoSe_2$

I initially measured the Rabi splitting in model system MQWs; now, I transition to a 2D monolayer TMDC sample, which exhibits a single exciton resonance in both the observed transmission spectrum and the linear absorption. This resonance is excited using a resonant laser pulse, similar to the MQW experiment. However, to study these monolayers, certain optical components were replaced to achieve smaller spot sizes for the white-light probe and pump pulses. The probing white-light supercontinuum is first expanded to a 1-inch diameter and then focused to an approximately 10 µm spot on the sample using a 1-inch lens with a 40 mm focal length.

With a probe spot size of 10 µm, the small monolayer TMDC flakes can be investigated in the modified OPOP setup. Initial measurements were performed on a $MoSe_2$ ML encapsulated in hexagonal boron nitride, placed on top of a diamond substrate. See Figure 3.2 c) for a schematic representation of the sample.

I use several spectral narrow pump energies around the 1s resonance to identify the optimal excitation conditions for Rabi splitting of the absorption. A symmetrical splitting was achieved by applying a pump pulse shifted 1.87 meV above the absorption resonance with a FWHM of 2.2 meV shaped by tilted longpass and shortpass filters (orange area in Figure 4.8 a)).

Figure 4.8 a) depicts a density series to observe the dynamics of the excitation as a function of photon density. The absorption splits into two peaks as the photon density increases. In subfigure b), the absorption peak splitting is plotted against the square root of the pump power. As the pump power increases, the higher-energy branch shifts linearly, while the lower-energy branch remains stationary.

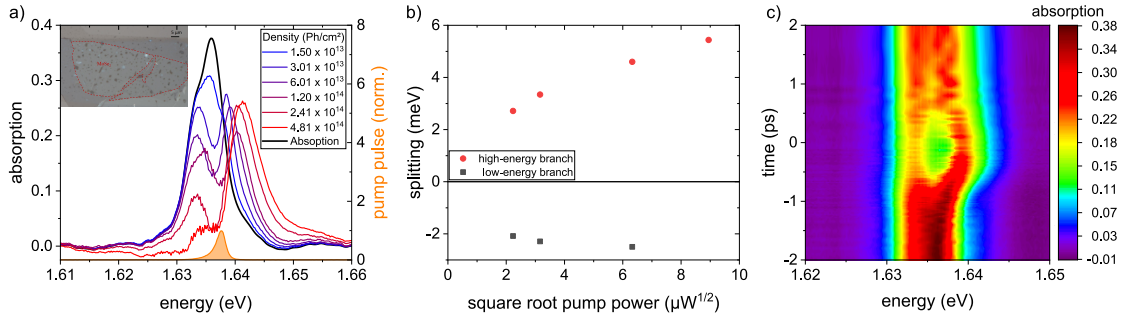

Figure 4.8: a) Linear absorption of a $MoSe_2$ ML sample (black line) with a typical pump pulse (orange) used for Paper III. The inset shows a microscope image of the sample, taken by Marzia Cuccu of the Chernikov group, the monolayer is highlighted in red. A density series of the pump pulse is shown from blue to red, revealing visible splitting of the absorption. b) By plotting the peak position energy against the square root of the pump power, a trend of increased splitting of the high-energy branch with higher excitation power becomes evident. c) 2D false-color representation of the absorption dynamics at varying time delays between the excitation and probe pulses, measured at a photon density of $5.8 \cdot 10^{13}\,\mathrm{Ph/cm^2}$ for collinear polarization.

In Figure 4.8 c), a 2D false-color representation of the dynamics of the absorption is plotted for a photon density of $5.8 \cdot 10^{13}\,\mathrm{Ph/cm^2}$. The measured 2D image closely resembles the symmetrical resonant AC Stark splitting measurements on InGaAs/GaAs QD (Ref. [146]). The splitting begins at around -500 ps delay when the 850 fs long excitation pulse starts to interact with the sample. The absorption resonance splits symmetrically into two peaks around 0 ps. After 0.5 ps, the splitting decreases, and the two absorption branches converge into a single absorption peak, which becomes broadened due to optical excitation.

Figure 4.9 presents the $\Delta\alpha$L data from the density-dependent measurements at the same time points using a) cross-linearly polarized light and b) collinear polarization. Both polarization geometries exhibit a blueshift of the excitonic 1s resonance at 1.638 eV, which scales with the photon density of the pump pulse. In the collinear case, the blueshift is much stronger than in the cross-linear case. Additionally, a change in absorption was observed at 1.6 eV. In photoluminescence measurements by the Chernikov group and other studies [147–149], this signal is attributed to the trion of the $MoSe_2$ monolayer. The inset provides a magnified view of the trion energy range. For the cross-linear polarization, an enhanced absorption signal is observed, which is nearly zero at the lowest photon density, increases at intermediate photon densities, and weakens again at higher densities, similar to the behavior of the 1s resonance. When switching to the collinear polarization, an enhanced absorption peak is also present, accompanied by a shift to lower energies that scales with the photon density. In the collinear configuration, the enhanced absorption is significantly stronger compared to the cross-linear case.

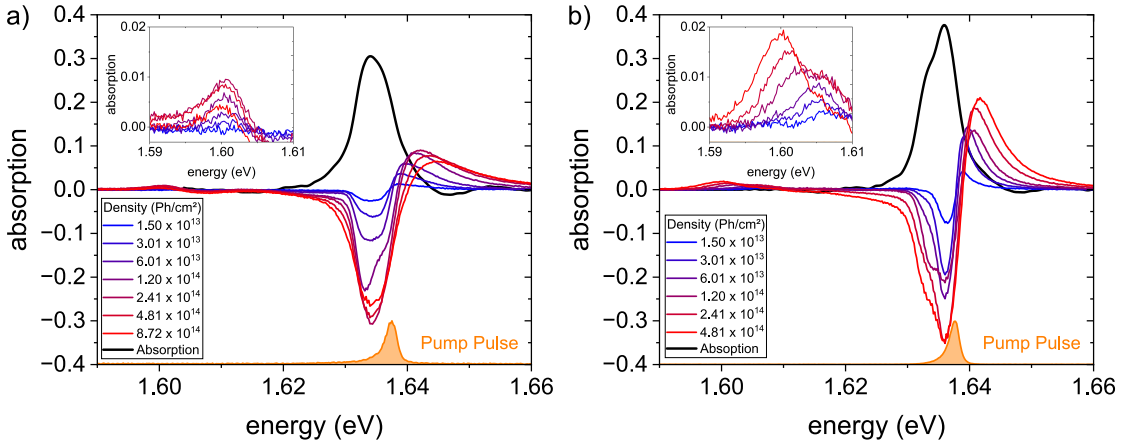

Figure 4.9: a) The cross-linear $\Delta\alpha$L signal of the $MoSe_2$ monolayer density series exhibits a blueshift of the 1s resonance and enhanced absorption at 1.6 eV. The black line represents the sample's absorption, while the orange-shaded area indicates the pump pulse used. b) The collinear $\Delta\alpha$L signal also shows a blueshift of the resonance, along with an enhanced absorption signal at the trion position, which shifts with photon density. The insets highlight the trion energy region: in the cross-linear case a), only a single enhanced absorption peak, scaling with photon density, is observed. In the collinear polarization case b), there is both an enhanced absorption peak and a peak that shifts to lower energies with increasing excitation power.

5 Summary & Outlook

During this dissertation, an ultrafast spectroscopy laboratory featuring a high-repetition-rate regenerative amplifier built from the ground up. Additionally, an existing pump-probe setup was modified to enable ultrafast, polarization-dependent optical pump–optical probe spectroscopy experiments. The first setup has a repetition rate of up to 1 MHz and a central wavelength of 1030 nm, which was used to collect data for Paper I and the $MoSe_2$ ML data for Paper III. The second system operates at a 5 kHz repetition rate system centered around 800 nm with a pulse shaper in the pump path to shape the excitation pulse to a FWHM of 2.71 meV, which was used for Paper II. Both setups employ an OPA to generate the excitation pump pulses tailored to the specific energy ranges required by the samples.

An innovative measurement software routine was developed, utilizing a transfer function that reads out different ROIs of a CCD, simultaneously recording both the reference white-light and the transmitted light spectra through the sample. This approach allows the acquisition of the $\Delta\alpha$L signal with just one spectrum per time step, compared to the previous method, which required four spectra. A key advantage of this setup is that it eliminates the need for shuttering at each time step, accelerating measurements by a factor of two to three while effectively reducing global white-light fluctuations. The most time-intensive aspect of the measurement is now the precise positioning of the translation stage with sub-femtosecond accuracy and the acquisition of a spectrum. The stage can autonomously report its exact position to the measurement program, removing the need to wait for stage movement and allowing for continuous data acquisition. In this scenario, the primary speed-limiting factor becomes the CCD's readout rate, which depends on the light intensity incident on the spectrometer to maintain an optimal signal-to-noise ratio.

Paper I demonstrates that type-II semiconductor heterostructure systems can effectively serve as gain media in high-repetition-rate lasers. My study of the gain dynamics in model type-II systems reveals ultrafast gain recovery times, occurring within just a few picoseconds after a stimulated emission process. These findings establish the physical limit for the maximum repetition rate in laser systems based on (Ga,In)As/GaAs/Ga(As,Sb) type-II heterostructures. In practical applications, pulsed semiconductor laser sources utilizing type-II multi-quantum well structures could achieve repetition rates as high as 100 GHz, making them highly viable for advanced technologies.

Paper II presents fundamental research on type-II heterostructures and their interaction with light. This study analyzes the microscopic mechanism driving the optical Stark effect in charge-transfer excitons within high-quality (Ga,In)As/GaAs/Ga(As,Sb) type-II heterostructures using a transient pump-probe measurement setup. The interaction between the CTX and the laser field was observed to depend on the polarization of the excitation and probe pulses. The blueshift of the CTX resonance, observed in both co-circular and counter-circular polarization configurations, contrasts with the shifts seen in spatially direct exciton resonances.

Paper III will investigate experimental evidence of Rabi splitting in $1s$ exciton resonances in (Ga,In)As quantum wells and $MoSe_2$ monolayers under resonant excitation conditions. Additionally, with increased excitation, I observed the emergence of additional absorption peaks, Rabi oscillations, and coherent gain in the MQW sample.

This thesis opens new pathways for both fundamental research and technological applications in semiconductor physics. The demonstrated potential of type-II heterostructures as gain media in high-repetition-rate lasers indicates promising advancements in ultrafast optical communication. The optical Stark effect in charge-transfer excitons provides valuable insights into electron dynamics in semiconductors, paving the way for advancements in the design of more efficient electronic and optoelectronic devices. Furthermore, the observed Rabi splitting and coherent gain in quantum wells and TMDC monolayers highlight exciting opportunities in quantum information processing.

Zusammenfassung & Ausblick

Im Rahmen dieser Dissertation wurde ein Labor für ultraschnelle Spektroskopie mit einem regenerativen Verstärker mit hoher Repetitionsrate von Grund auf aufgebaut und ein weiterer Anregungs-Abfragungs-Aufbau modifiziert, um die Grundlage für ultraschnelle polarisationsabhängige Absorptionsänderungen einer Probe in Transmission zu messen. Der erste Aufbau hat eine Wiederholrate von bis zu 1 MHz und eine zentrale Wellenlänge von 1030 nm, mit dem die Daten für Paper I & Paper III aufgenommen wurden. Das zweite System ist ein Laser mit einer Repetitionsrate von 5 kHz und einer zentralen Wellenlänge von 800 nm mit einem Pulsformer im Anregungspfad, um den Anregungspuls auf eine Halbwertsbreite von 2.71 meV zu bringen, was für Paper II verwendet wurde. In beiden Fällen wird ein optischer Parametrischer Verstärker verwendet, um Anregungspulse zu erzeugen, die auf die spezifischen Energiebereiche zugeschnitten sind, die von den Proben benötigt werden.

Es wurde eine innovative Messroutine entwickelt, die eine Transferfunktion benutzt, die verschiedene Bereiche auf einer CCD ausliest und somit gleichzeitig das Weißlicht-Referenzspektrum als auch das durch die Probe transmittierte Spektrum misst. Dieser Ansatz ermöglicht die Erfassung des $\Delta\alpha$L-Signals mit nur einem Spektrum pro Zeitschritt anstelle der bisherigen Methode der Erfassung von vier Spektren. Ein wesentlicher Vorteil dieser Routine ist, dass kein mechanischer Block für jeden Zeitschritt benötigt wird, was die Messungen um den Faktor zwei bis drei beschleunigt und gleichzeitig globale Weißlichtschwankungen effektiv ausgleicht. Der zeitaufwändigste Aspekt der Messung ist nun die präzise Positionierung der Verschiebungsstrecke mit einer Genauigkeit von weniger als einem Mikrometer und die Aufnahme eines Spektrums. Die Verschiebestrecke kann ihre exakte Position eigenständig an das Messprogramm melden, so dass nicht mehr auf die Bewegung der Verschiebestrecke gewartet werden muss und eine kontinuierliche Datenerfassung möglich ist. In diesem Szenario ist der primäre geschwindigkeitsbegrenzende Faktor die Ausleserate der CCD, die von der in das Spektrometer einfallenden Lichtintensität abhängt, um ein optimales Signal-Rausch-Verhältnis zu erhalten.

Paper I zeigt, dass Typ-II Halbleiter-Heterostruktursysteme als Verstärkungsmedium in Lasern mit hoher Repetitionsrate eingesetzt werden können. Meine Untersuchung der Verstärkungsdynamik in Typ-II Modellsystemen zeigt ultraschnelle Erholungszeiten der Verstärkung, die innerhalb weniger Pikosekunden nach einem stimulierten Emissionsprozess auftreten. Diese Ergebnisse setzen die physikalische Grenze für die maximale Repetitionsrate in Lasersystemen basierend auf (Ga,In)As/GaAs/Ga(As,Sb) Typ-II Heterostrukturen. In praktischen Anwendungen könnten gepulste Halbleiterlaserquellen mit Typ-II-artigen Multiquantumwell-Strukturen extreme Repetitionsraten von etwa 100 GHz erreichen, was sie für fortgeschrittene Technologien interessant macht.

Paper II stellt Grundlagenforschung zu Typ-II Heterostrukturen und deren Wechselwirkung mit Licht dar. Diese Studie analysiert den mikroskopischen Mechanismus, der den optischen Stark-Effekt in Charge-Transfer-Exzitonen in (Ga,In)As/GaAs/Ga(As,Sb) Typ-II Heterostrukturen antreibt, unter Verwendung eines Anrege-Abfrage-Messaufbaus in Transmission. Die Wechselwirkung zwischen dem CTX und dem Laserfeld wurde in Abhängigkeit von der Polarisation der Anregungs- und Abfragepulse beobachtet. Die Blauverschiebung der CTX-Resonanz sowohl in kozirkularen als auch in gegenzirkularen Polarisationskonfigurationen steht im Gegensatz zu den Verschiebungen, die bei räumlich direkten Exzitonenresonanzen beobachtet werden.

Paper III untersucht den experimentellen Nachweis von Rabi-Aufspaltung von 1s-Exzitonenresonanzen in (Ga,In)As-Quantentöpfen und $MoSe_2$ Einzelschichten unter resonanten Anregungsbedingungen. Darüber hinaus beobachtete ich das Auftreten von zusätzlichen Absorptionsmaxima, Rabi-Oszillationen und kohärenter Verstärkung der (Ga,In)As-Probe bei starker resonanter Anregung.

6 Author's Contributions

I - Gain recovery dynamics in active type-II semiconductor media, Ref. [55]

F. Schäfer, M. Stein, J. Lorenz, F. Dobener, C. Ngo, J. T. Steiner, C. Fuchs, W. Stolz, K. Volz, T. Meier, J. Hader, J. V. Moloney, S. W. Koch and S. Chatterjee

Abstract

Type-II heterostructures as active layers for semiconductor laser devices combine the advantages of a spectrally broad, temperature stable, and efficient gain with the potential for electrical injection pumping. Their intrinsic charge carrier relaxation dynamics limit the maximum achievable repetition rates beyond any constraints of cavity design or heat dissipation. Of particular interest are the initial build up of gain after high-energy injection and the gain recovery dynamics following depletion through a stimulated emission process. The latter simulates the operation condition of a pulsed laser or semiconductor optical amplifier. An optical pump pulse injects hot charge carriers that eventually build up broad spectral gain in a model (Ga,In)As/GaAs/Ga(As,Sb) heterostructure. The surplus energies of the optical pump mimic the electron energies typical for electrical injection. Subsequently, a second laser pulse tuned to the broad spectral gain region depletes the population inversion through stimulated emission. The spectrally resolved nonlinear transmission dynamics reveal gain recovery times as fast as 5 ps. These data define the intrinsic limit for the highest laser repetition rate possible with this material system in the range of 100 GHz. The experimental results are analyzed using a microscopic many-body theory identifying the origins of the broad gain spectrum.

Contribution

I designed the setup with MS and SC, built it with MS, and defined the requirements for the measurement software which was developed by FD. I modified the setup with JL to introduce a second excitation beam. Measurements were conducted with JL and MS. The experimental data were analyzed by me, and I created the graphical representations. The manuscript was written and improved in collaboration with AT, MS, TM, and SC.

Applied Physics Letters

scitation.org/journal/apl

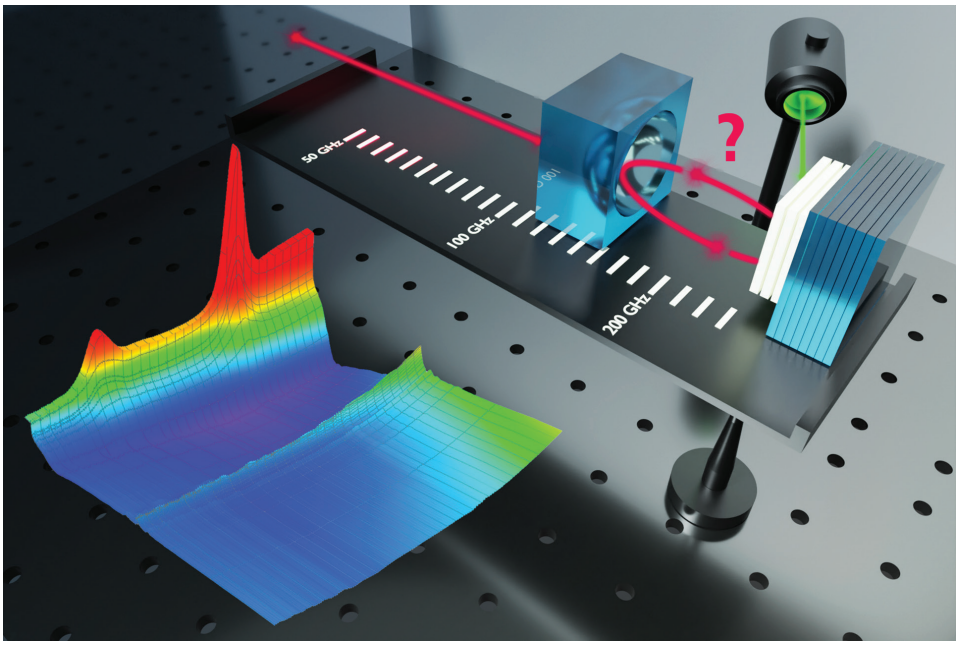

Volume 122, Issue 8, 20 Feb. 2023

Gain recovery dynamics in active type-II semiconductor heterostructures

Appl. Phys. Lett. **122**, 082104 (2023); doi: 10.1063/5.0128777

F. Schäfer, M. Stein, J. Lorenz, F. Dobener, C. Ngo, J. T. Steiner, C. Fuchs, W. Stolz, K. Volz, T. Meier, J. Hader, J. V. Moloney, S. W. Koch, and S. Chatterjee

AIP Publishing

Applied Physics Letters ARTICLE scitation.org/journal/apl

Gain recovery dynamics in active type-II semiconductor heterostructures

Cite as: Appl. Phys. Lett. **122**, 082104 (2023); doi: 10.1063/5.0128777
Submitted: 30 September 2022 · Accepted: 9 January 2023 ·
Published Online: 21 February 2023

F. Schäfer,[1] M. Stein,[1] J. Lorenz,[1] F. Dobener,[1] C. Ngo,[2] J. T. Steiner,[2] C. Fuchs,[3] W. Stolz,[3] K. Volz,[3] T. Meier,[2] J. Hader,[4] J. V. Moloney,[4] S. W. Koch,[4,5,a)] and S. Chatterjee[1,b)]

AFFILIATIONS

[1]Institute of Experimental Physics I and Center for Materials Research (LaMa), Justus-Liebig-University Giessen, Heinrich-Buff-Ring 16, D-35392 Giessen, Germany
[2]Department of Physics, Paderborn University, Warburger Strasse 100, D-33098 Paderborn, Germany
[3]Structure & Technology Research Laboratory (WZMW), Philipps-University Marburg, Hans-Meerwein-Straße 6, D-35032 Marburg, Germany
[4]Wyant College of Optical Sciences, The University of Arizona, 1630 East University Boulevard, Tucson, Arizona 85721, USA
[5]Department of Physics and Materials Sciences Center, Philipps-Universität Marburg, Renthof 5, D-35032 Marburg, Germany

[a)]Deceased.
[b)]**Author to whom correspondence should be addressed:** sangam.chatterjee@physik.uni-giessen.de

ABSTRACT

Type-II heterostructures as active layers for semiconductor laser devices combine the advantages of a spectrally broad, temperature stable, and efficient gain with the potential for electrical injection pumping. Their intrinsic charge carrier relaxation dynamics limit the maximum achievable repetition rates beyond any constraints of cavity design or heat dissipation. Of particular interest are the initial build up of gain after high-energy injection and the gain recovery dynamics following depletion through a stimulated emission process. The latter simulates the operation condition of a pulsed laser or semiconductor optical amplifier. An optical pump pulse injects hot charge carriers that eventually build up broad spectral gain in a model (Ga,In)As/GaAs/Ga(As,Sb) heterostructure. The surplus energies of the optical pump mimic the electron energies typical for electrical injection. Subsequently, a second laser pulse tuned to the broad spectral gain region depletes the population inversion through stimulated emission. The spectrally resolved nonlinear transmission dynamics reveal gain recovery times as fast as 5 ps. These data define the intrinsic limit for the highest laser repetition rate possible with this material system in the range of 100 GHz. The experimental results are analyzed using a microscopic many-body theory identifying the origins of the broad gain spectrum.

Semiconductor lasers are presumably the most versatile, compact, and energy efficient laser light source of the present age. Their advantageous properties have opened up virtually endless applications, fulfilling the prophecy of the famous quote, "a Solution Seeking a Problem".[1] In particular, pulsed-lasers are gaining more impact across all disciplines, especially for extremely fast repetition rates. Exemplary applications include processing in materials sciences and mechanical engineering,[2,3] surgeries in life sciences,[4,5] high-speed telecom applications,[6–8] and transient spectroscopy in physical sciences,[9,10] all of which will benefit from ultrafast, high-repetition-rate semiconductor lasers. Consequently, there is a tremendous research effort to develop lasers with ultra-high repetition rates. In many cases, however, these advances are not limited by the gain dynamics of the laser medium itself, but by mode-locking mechanisms, cavity designs, or heat dissipation.[7,11] Due to its great importance, gain recovery dynamics of laser media have been studied theoretically and experimentally on quantum cascade lasers[12] and quantum dot-based laser materials.[13–19] As a result, the gain recovery dynamics of some quantum dot-based structures would allow laser repetition rates beyond 200 GHz.[20,21] Much fewer experimental studies exist for quantum well (QW) structures, the gain recovery dynamics of which are generally considered to be slower than those found in quantum dot structures.[22–24] Nevertheless, QW-based semiconductor lasers dominate in many practical applications, achieving similar maximum repetition rates and shorter pulse lengths in operation than quantum dot-based devices.[25–28] The highest fundamental laser repetition rates of QW-based lasers are in the range

of 50–100 GHz,[11,29] while those of quantum dot-based lasers are in the same order of 40 to 80 GHz.[30–32]

Since subpicosecond pulses are equally necessary for ultra-high laser repetition rates in the hundred GHz range, QW-based gain media could be promising despite their slower gain recovery. Compared to regular quantum well structures, semiconductor lasers based on type-II heterostructures show promising properties like a more flexible band structure engineering or wavelength versatility and often exhibit very broad gain spectra.[33–35] Nonetheless, in these emerging type-II QW heterostructures, the gain recovery dynamics are still entirely unexplored.[36]

In this Letter, we present the ultrafast, spectrally resolved gain dynamics typical for pulsed semiconductor lasers or semiconductor optical amplifiers before and shortly after stimulated emission processes. Experimentally, the performance during operation is mimicked by studying the subpicosecond charge carrier dynamics in an (In,Ga)As/Ga(As,Sb) heterostructure with type-II band alignment as gain medium rather than performing true in-operando experiments on processed devices. We simulate the optical response after an optical pump pulse with a microscopic theory and discuss the importance of the adjacent resonances in a type-II QW. The excellent agreement supports the validity of the intrinsic material limits, i.e., the gain recovery after depletion through stimulated emission. These studies provide the theoretical maximum rate at which further laser pulses can trigger stimulated emission in this active medium and contribute to devising guidance for optimized structure design to improve repetition rates.

The heterostructures are grown by metal-organic vapor-phase epitaxy; details of the growth are given in Ref. 37. High-resolution x-ray diffraction as well as atomic force microscopy confirm the thicknesses of 7.7 and 7.5 nm for the $Ga_{0.942}In_{0.058}As$ and the $GaAs_{0.93}Sb_{0.07}$ layers, respectively. These are separated by a GaAs interlayer of 1 nm. The 50 repetitions are separated by GaAs/GaAsP/GaAs barriers, which also provide strain compensation. A schematic of the heterostructure is shown in Ref. 38 [Fig. 1(a)].

A 100 kHz repetition rate regenerative ytterbium-doped potassium gadolinium tungstate (Yb:KGW) amplifier system provides 200 fs pulses centered around 1030 nm with a pulse energy of 20 μJ. About 75 % of the amplifier emission drive an optical parametric amplifier (OPA); the rest generates a white-light supercontinuum in a 4 mm thick sapphire crystal. The main output of the OPA provides tunable central wavelength pulses, which are compressed to about 70 fs using a prism compressor. These are tuned to spectrally overlap with the material gain in the sample mounted in a helium-cooled cold-finger cryostat that cools the sample to a fixed temperature of 6 K. A residual output of the OPA delivers pulse energies up to 5 μJ at 515 nm to optically excite the sample with a preceeding laser pulse. Here, this first excitation pulse is used to drive the sample into optical inversion. We use the additional second optical pulse from the OPA to impinge on the sample with a defined time delay and harvest the previously generated optical gain expanding the scope of conventional optical pump-optical probe experiments. All beams are focused onto the sample; the two excitation beams have spot sizes of 250 μm, while the white-light supercontinuum is focused to 140 μm. We use a wedged beam splitter in the white-light beam path to split the light into two beams. One part is focused onto the sample to probe the sample's excitation-induced absorption changes and the other part is used as a reference pulse.

The white-light supercontinuum passing through the sample and the reference pulse are simultaneously and independently analyzed using an imaging spectrometer with a 500 lines/mm grating and a Si-CCD camera utilizing separate regions of interest on the chip [see Fig. 1(a)]. The spectra of both pulses are compared and a transfer function (T_f) converts the spectrum of the reference pulse (T_{ref}) into the spectrum of the pulse transmitted through the unexcited sample. The reference path, thus, provides the spectrum of the unexcited sample at any time and is independent of fluctuations in the spectrum of the white-light, as the transfer function is determined by the optical pathway through the setup and consequently does not change in time. By adding the optical excitation, we thus simultaneously obtain the transmission through the excited sample (T_P) and the transmission through the unexcited sample (T_0). Taking into account the photoluminescence (T_{Pl}) and the scattered-light background (T_{Bg}) for both white-light beam paths at the beginning of the measurement yields the differential absorption at each time step according to

$$\Delta\alpha L = -ln\left[(T_P - T_{Pl})/(T_f \cdot (T_{ref} - T_{Bg}))\right].$$

The measurements of the transmission through the excited and the unexcited sample (via the reference path) are simultaneous and, thus, not distorted by white-light fluctuations, and each time step is measured in real time just by reading out the spectrometer. These advantages provide an extremely accurate, fast, and low-noise method to determine the differential absorption.

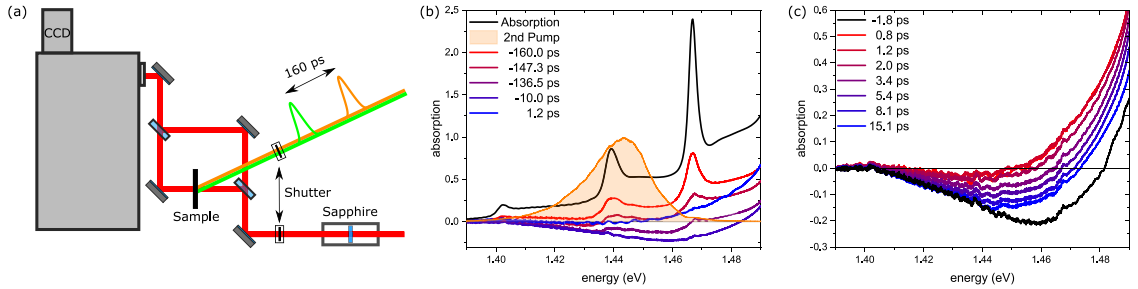

FIG. 1. (a) Schematic of the experimental optical pump—optical probe setup. The green and orange pulses have a time delay of 160 ps and are used to excite the sample, while the white-light pulses (shown as a red line) generated in the sapphire crystal probe the carrier dynamics induced by the excitation. (b) Linear absorption spectrum (black), spectrum of the second pump pulse with a central energy of 1.442 eV (orange-shaded area), and the transient absorption data for different time delays after the initial pump pulse. (c) Absorption spectra of the sample immediately before and after the second pump pulse impinges on the sample.

Adding the differential absorption to the linear absorption then yields the absorption of the excited sample, where a negative absorption corresponds to optical amplification, i.e., optical gain.

Figure 1(b) shows the linear absorption of the unexcited sample (black line). The spectrum exhibits three distinct peaks, one at 1.465 eV corresponding to the exciton peak in the (Ga,In)As layer, one at 1.440 eV representing the Ga(As,Sb) layer exciton, and one at 1.402 eV. The latter is identified as the absorption peak of the charge transfer exciton (CTX).

The times given refer to the temporal separation between the white-light pulse and the second excitation pulse that impinges on the sample at $t = 0$ ps. Excitation of the first pulse at $t = -160$ ps with 2.4 eV and a photon density of $8.9 \cdot 10^{14}/\mathrm{cm}^2$ creates hot charge carriers with significant excess energy, which corresponds to typical excitation conditions in electrically pumped GaAs-based semiconductor lasers, i.e., for injection from (Al,Ga)As barriers. After excitation, the charge carriers relax toward the bandgap on a fast, subpicosecond timescale and thermalize into hot quasi-equilibrium distributions. After that the distributions cool via phonon emission leading to rising occupations at the bandgap. This leads to a continuously increasing bleaching of the absorption, eventually resulting in population inversion observable as negative absorption and, hence, optical gain at $t = -136.5$ ps. A broad optical gain is finally present at $t = -10$ ps, extending from roughly 1.40 to 1.48 eV. Thus, the gain extends from the CTX resonance to slightly above the exciton resonance associated with the (Ga,In)As layer. This describes very well the conditions prevailing when the second pulse impinges on the sample with a photon density of $8.4 \cdot 10^{14}/\mathrm{cm}^2$ at $t = 0$ ps. The second pump pulse that is used to stimulate emission is shown as an orange line with orange shading at a central energy of 1.442 eV in Fig. 1(b). The spectrum ranges approximately from 1.41 to 1.47 eV and is, therefore, spectrally overlapping with the material gain created by the first pulse. Accordingly, the second pulse is able to cause stimulated emission and reduce the population inversion.

This behavior is clearly visible in Fig. 1(c), which shows an enlarged section of the absorption spectra for times close to the arrival of the second pulse. The optical gain disappears almost entirely right after the second pulse hits the sample, as can be seen for $t = 0.8$ ps. The gain subsequently recovers on a picosecond timescale. After about 15 ps, the gain in the spectral range from 1.40 to 1.44 eV is approximately the same as the gain immediately before the arrival of the second pulse. The gain also recovers in the higher energy spectral range from 1.44 to 1.47 eV; however, it does not reach the values prior to the arrival of the second pulse. This is attributed to the refilling of the vacated states at lower energies, i.e., between 1.40 and 1.44 eV, which are populated by the relaxation of carriers occupying the transition energy range from 1.44 to 1.47 eV.

We use a fully microscopic many-body theory to analyze the experimental observations. The model solves the semiconductor Bloch equations, i.e., the equations of motion for the microscopic optical polarizations and carrier distributions to calculate the absorption and gain spectra.[39,40] Here, coherent Coulomb effects like exciton resonances, Coulomb enhancement of the continuum absorption, and density-dependent bandgap renormalizations are fully taken into account. Also, electron–electron and electron–phonon collisions are included explicitly in second Born–Markov approximation leading to quantum-Boltzmann type scattering equations. The single-particle properties are obtained by evaluating an 8×8 $\mathbf{k} \cdot \mathbf{p}$ model for the designed heterostructure to determine the band structure and the electron and hole wavefunctions.[41] Strain effects between the different layers of the semiconductor heterostructure are treated as described in Ref. 42. Deformations of the confinement potentials due to local electron–hole charge imbalances are included by solving the corresponding Poisson–Schrödinger problem. The inhomogeneous line broadening observed in the sample absorption is taken into account through a Gaussian broadening with a width of 4 meV.

This microscopic approach has shown excellent agreement with experimental findings for a wide variety of materials covering the mid-IR to the UV wavelength regimes.[43] In particular, it has been shown to be very successful in the design and analysis of type-II QW systems as investigated here.[33,44–46]

Figure 2(a) shows the theoretical absorption spectrum for various carrier densities. Similar to the experimental absorption in Fig. 1(b), the low density absorption shows three excitonic resonances at 1.46,

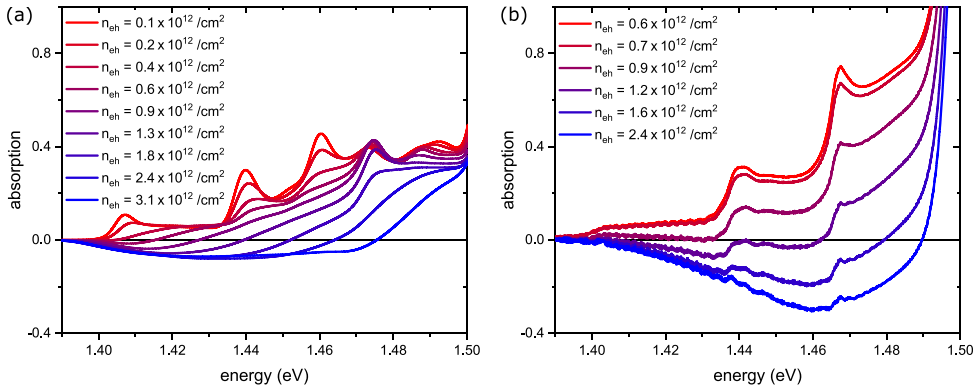

FIG. 2. (a) Theoretical absorption of the sample after optical excitation by the first pump pulse. The absorption is shown for various excitation-induced carrier densities ranging from $n_{eh} = 0.1 \cdot 10^{12}/\mathrm{cm}^2$ to $n_{eh} = 3.1 \cdot 10^{12}/\mathrm{cm}^2$. (b) Experimentally measured absorption for comparable excitation densities.

1.44, and 1.407 eV. The theory allows us to identify these as excitons where electrons and holes are both localized in the (Ga,In)As layer, both in the Ga(As,Sb) layer and where the electron is in the (Ga,In)As layer and the hole is in the Ga(As,Sb) layer, respectively. The latter represents the CTX. For high charge carrier densities of $n_{eh} = 2.4 \cdot 10^{12}/\mathrm{cm}^2$, which we obtain from a photon density of $8.9 \cdot 10^{14}/\mathrm{cm}^2$, we observe a broad gain spectrum as in the experiment in Fig. 2(b). The energetically broad gain spectrum allows for a reduced temperature sensitivity for laser and amplifier applications. In type-I QWs, the optical gain is usually dominated by the transitions between the lowest electron and hole subband since electrons and holes are localized in the same layer and the transitions have the strongest wavefunction overlap. Here, the wavefunction overlap between states in the lowest electron and hole subband is limited since the carriers are not localized in the same layer. While fewer carriers occupy the second electron and hole subbands, the overlap of these states with the energetically lowest states localized in the same layer is larger. This allows the higher subband transitions to contribute to the gain spectrum to a similar extent as the lowest subband transition leading to a spectrally wider gain—although with a somewhat lower amplitude for a given density.

The spectrally integrated transient absorption reveals detailed insights into the dynamics of the gain recovery. The transient data integrated across the energy range from 1.425 to 1.466 eV are shown in Fig. 3(a) for several photon densities of the first pump pulse. An incident photon density of $1.0 \cdot 10^{14}/\mathrm{cm}^2$ is insufficient to generate any optical gain. In this case, however, the second pulse is partially absorbed and leads to a decrease of the absorption in the sample. A photon density of $2.1 \cdot 10^{14}/\mathrm{cm}^2$ causes—on average over the integrated spectral range—a transparency in the sample as seen by the spectrally integrated absorption of zero. Higher photon densities of the first pulse generate gain in the sample. Notably, the spectrally integrated absorption is constant at values around −0.1 on a picosecond timescale before the second pump pulse hits the sample for initial pulse excitation photon densities above $3.0 \cdot 10^{14}/\mathrm{cm}^2$. The second pulse then completely dumps the spectrally integrated gain to zero, i.e., transparency is reached within the time resolution of our experiment. Unfortunately, the data recorded during the temporal overlap of the second pump pulse and the white-light pulse are obscured by two-photon absorption processes; therefore, we grayed out this time domain. The gain transiently recovers within 15 ps after the second pulse has passed the sample. The increase of the absorption at 16 ps is caused by the double pass of the second pulse reflected from the back side of the sample.

An exponential fit to the transients quantifies the recovery time constant of the gain to about 5 ps. This corresponds to the minimum time separation between two successive light pulses that can be amplified in this material system. Interestingly, this is very comparable to the gain recovery dynamics observed in type-I quantum well structures.[23,24,47] Speculations that the gain recovery is slowed down in type-II heterostructures can therefore not be confirmed experimentally.[36] Assuming that it takes about two time constants to recover a significant portion of the gain, this gives a maximum possible repetition rate of about 100 GHz. Note that our experiments are performed at liquid helium temperatures. We expect similar behavior for elevated temperatures of the crystal lattice since the relaxation dynamics at elevated excitation densities are mainly governed by Coulomb interaction rather than by phonon scattering. The calculated exponential times for several photon densities of the first pump pulse as well as the change of the absorption (step height) immediately before and after the second pulse are given in Fig. 3(b). The gain recovers slightly faster with increasing carrier densities injected by the first pulse, cf., Fig. 3(b). This can be explained by the larger reservoir of occupied states at energies above the gain region, which allows for a faster refilling. At the same time, as the excitation density of the first pulse increases, the step height, i.e., the change in absorption due to the second pulse impinging on the sample increases. Here, stronger excitations by the first pulse lead to more gain that can be depleted by the second pulse. For lower excitation densities, there is no or hardly any gain, and accordingly, the step height approaches zero. Overall, the gain recovery dynamics are quite robust for different excitation conditions. In addition, we have also performed measurements for different time delays

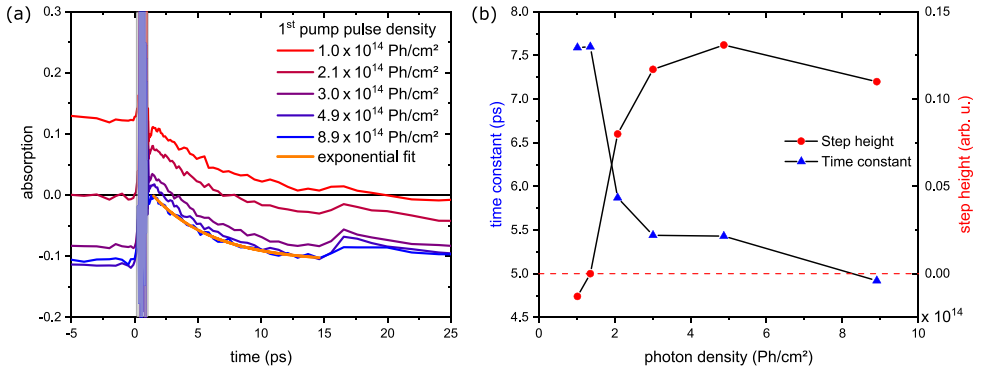

FIG. 3. (a) Spectrally integrated transients for different photon densities of the first pump pulse close to $t = 0$ ps, where the second pulse with a fixed photon density of $8.4 \cdot 10^{14}/\mathrm{cm}^2$ impinges on the sample. The second pulse depletes the gain, if present, and the subsequent gain recovery time can be extracted by an exponential fit to the transients. The temporal overlap between second pump pulse and white-light probe is grayed out due to two-photon absorption artifacts. (b) Time constants of the exponential fits together with the step height, i.e., the initial change of the absorption due to the second pulse.

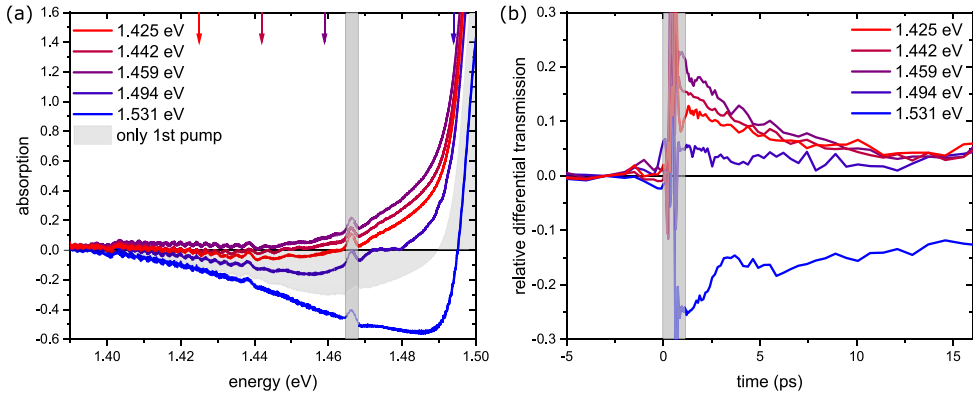

FIG. 4. (a) Gain spectra 1.5 ps after incidence of the second pulses with different central energies (indicated by arrows) on the sample. The gray shaded energy range is distorted by experimental artifacts due to strong exciton absorption at this position and the sample not being perfectly homogeneous. (b) Corresponding relative differential transmission data integrated from 1.40 to 1.49 eV. Here, the differential transmission is set to zero, shortly before the second pulse hits the sample. This allows a more direct comparison of the changes caused by the second pulses with different central energy.

between the first and the second pump pulse, ranging from 90 to 230 ps. This hardly affects the gain recovery dynamics. This corroborates the suggested similarities of the gain recovery dynamics for cw excitation or electrical injection.

In Fig. 4(a), we show the absorption spectra at 1.5 ps, i.e., shortly after the second pump pulse stimulates the sample with different central energies. Shaded in gray is the absorption spectrum at the same time delay when only the first pulse hits the sample. When the spectrum of the second pulse matches the spectral region of the material gain, the optical gain at hand is almost completely depleted. However, some gain remains when the second pulse is slightly detuned from the gain spectrum, i.e., to 1.425 eV. Larger detunings to 1.494 eV lead to far less gain depletion as the spectral overlap between the material gain and the second pulse is severely reduced. If the second pulse is detuned to 1.531 eV, i.e., into the absorptive region above the gain, the gain increases quasi-instantaneously [blue line in Figs. 4(a) and 4(b)]. This can be explained by the ultrafast thermalization of the additionally injected charge carriers close to the band edge. Since these charge carriers only have a small excess energy compared to the carriers generated by the first pulse, they do not need to cooldown for extended periods of time and, thus, immediately lead to an increase of the occupations close to the band edge.

In conclusion, the detailed gain dynamics in model type-II systems yield ultrafast gain recovery times within a few picoseconds after a stimulated emission process. These data demonstrate the physical limit to the maximum repetition rate for laser systems based on (Ga,In)As/GaAs/Ga(As,Sb) type-II heterostructures. In practice, pulsed semiconductor laser sources based on type-II multi-quantum well structures with extreme repetition rates around 100 GHz are feasible.

Financial support from the Deutsche Forschungsgemeinschaft via the Collaborative Research Center No. 223848855-SFB 1083, the European Regional Development Fund (ERDF) through the innovation laboratory high-performance materials FPG990 0005/2018, as well as the Air Force Office of Scientific Research under Award Nos. FA9550-19-1-0032 and FA9550-21-1-0463 is gratefully acknowledged.

AUTHOR DECLARATIONS

Conflict of Interest

The authors have no conflicts to disclose.

Author Contributions

Felix Schäfer: Conceptualization (equal); Data curation (equal); Formal analysis (equal); Investigation (equal); Methodology (equal); Software (equal); Visualization (equal); Writing – original draft (equal); Writing – review & editing (equal). **Torsten Meier:** Formal analysis (equal); Funding acquisition (equal); Supervision (equal); Writing – original draft (equal); Writing – review & editing (equal). **Jorg Hader:** Formal analysis (equal); Resources (equal); Software (equal); Writing – review & editing (equal). **Jerome V. Moloney:** Funding acquisition (equal); Supervision (equal); Writing – review & editing (equal). **Stephan W. Koch:** Conceptualization (equal); Funding acquisition (equal); Resources (equal); Supervision (equal). **Sangam Chatterjee:** Conceptualization (equal); Funding acquisition (equal); Methodology (equal); Project administration (equal); Resources (equal); Supervision (equal); Validation (equal); Writing – review & editing (equal). **Markus Stein:** Conceptualization (lead); Data curation (equal); Formal analysis (equal); Investigation (equal); Methodology (equal); Resources (supporting); Supervision (equal); Validation (equal); Writing – original draft (equal); Writing – review & editing (equal). **Janine Lorenz:** Data curation (supporting); Formal analysis (equal); Investigation (equal); Methodology (equal); Visualization (supporting); Writing – original draft (supporting); Writing – review & editing (equal). **Florian Dobener:** Data curation (supporting); Software (lead). **Cong Ngo:** Data curation (supporting); Formal analysis (supporting); Software (equal); Writing – review &

editing (equal). **Johannes T. Steiner:** Data curation (equal); Formal analysis (equal); Writing – original draft (equal); Writing – review & editing (equal). **Christian Fuchs:** Resources (lead). **Wolfgang Stolz:** Resources (equal); Supervision (supporting). **Kerstin Volz:** Funding acquisition (equal); Resources (lead); Supervision (supporting).

DATA AVAILABILITY

The data that support the findings of this study are available from the corresponding author upon reasonable request.

REFERENCES

[1]T. H. Maiman, "Stimulated optical radiation in ruby," Nature **187**, 493 (1960).
[2]K. C. Phillips, H. H. Gandhi, E. Mazur, and S. Sundaram, "Ultrafast laser processing of materials: A review," Adv. Opt. Photonics **7**, 684–712 (2015).
[3]M. Malinauskas, A. Žukauskas, S. Hasegawa, Y. Hayasaki, V. Mizeikis, R. Buividas, and S. Juodkazis, "Ultrafast laser processing of materials: From science to industry," Light **5**, e16133–e16133 (2016).
[4]K. E. Donaldson, R. Braga-Mele, F. Cabot, R. Davidson, D. K. Dhaliwal, R. Hamilton, M. Jackson, L. Patterson, K. Stonecipher, S. H. Yoo *et al.*, "Femtosecond laser-assisted cataract surgery," J. Cataract Refractive Surg. **39**, 1753–1763 (2013).
[5]C. L. Hoy, O. Ferhanoğlu, M. Yildirim, K. H. Kim, S. S. Karajanagi, K. M. C. Chan, J. B. Kobler, S. M. Zeitels, and A. Ben-Yakar, "Clinical ultrafast laser surgery: Recent advances and future directions," IEEE J. Sel. Top. Quantum Electron. **20**, 242–255 (2014).
[6]T. J. Kippenberg, R. Holzwarth, and S. A. Diddams, "Microresonator-based optical frequency combs," Science **332**, 555–559 (2011).
[7]A. S. Mayer, C. Phillips, and U. Keller, "Watt-level 10-gigahertz solid-state laser enabled by self-defocusing nonlinearities in an aperiodically poled crystal," Nat. Commun. **8**, 1673 (2017).
[8]V. Torres-Company, J. Schröder, A. Fülöp, M. Mazur, L. Lundberg, Ó. B. Helgason, M. Karlsson, and P. A. Andrekson, "Laser frequency combs for coherent optical communications," J. Lightwave Technol. **37**(7), 1663–1670 (2019).
[9]R. Berera, R. van Grondelle, and J. Kennis, "Ultrafast transient absorption spectroscopy: Principles and application to photosynthetic systems," Photosynth. Res. **101**, 105–118 (2009).
[10]M. Maiuri, M. Garavelli, and G. Cerullo, "Ultrafast spectroscopy: State of the art and open challenges," J. Am. Chem. Soc. **142**, 3–15 (2020).
[11]M. Mangold, C. A. Zaugg, S. M. Link, M. Golling, B. W. Tilma, and U. Keller, "Pulse repetition rate scaling from 5 to 100 GHz with a high-power semiconductor disk laser," Opt. Express **22**, 6099–6107 (2014).
[12]H. Choi, L. Diehl, Z.-K. Wu, M. Giovannini, J. Faist, F. Capasso, and T. B. Norris, "Gain recovery dynamics and photon-driven transport in quantum cascade lasers," Phys. Rev. Lett. **100**, 167401 (2008).
[13]N. Majer, K. Lüdge, and E. Schöll, "Cascading enables ultrafast gain recovery dynamics of quantum dot semiconductor optical amplifiers," Phys. Rev. B **82**, 235301 (2010).
[14]J. Gomis-Bresco, S. Dommers, V. V. Temnov, U. Woggon, M. Lämmlin, D. Bimberg, E. Malic, M. Richter, E. Schöll, and A. Knorr, "Impact of coulomb scattering on the ultrafast gain recovery in ingaas quantum dots," Phys. Rev. Lett. **101**, 256803 (2008).
[15]W. W. Chow and S. W. Koch, "Theory of semiconductor quantum-dot laser dynamics," IEEE J. Quantum Electron. **41**, 495–505 (2005).
[16]T. W. Berg, S. Bischoff, I. Magnusdottir, and J. Mork, "Ultrafast gain recovery and modulation limitations in self-assembled quantum-dot devices," IEEE Photonics Technol. Lett. **13**, 541–543 (2001).
[17]A. J. Zilkie, J. Meier, P. W. Smith, M. Mojahedi, J. S. Aitchison, P. J. Poole, C. N. Allen, P. Barrios, and D. Poitras, "Femtosecond gain and index dynamics in an InAs/InGaAsp quantum dot amplifier operating at 1.55 μm," Opt. Express **14**, 11453–11459 (2006).
[18]K. Kim, J. Urayama, T. B. Norris, J. Singh, J. Phillips, and P. Bhattacharya, "Gain dynamics and ultrafast spectral hole burning in In(Ga)As self-organized quantum dots," Appl. Phys. Lett. **81**, 670–672 (2002).
[19]B. Herzog, N. Owschimikow, J.-H. Schulze, R. Rosales, Y. Kaptan, M. Kolarczik, T. Switaiski, A. Strittmatter, D. Bimberg, U. W. Pohl *et al.*, "Fast gain and phase recovery of semiconductor optical amplifiers based on submonolayer quantum dots," Appl. Phys. Lett. **107**, 201102 (2015).
[20]S. Dommers, V. V. Temnov, U. Woggon, J. Gomis, J. Martinez-Pastor, M. Laemmlin, and D. Bimberg, "Complete ground state gain recovery after ultrashort double pulses in quantum dot based semiconductor optical amplifier," Appl. Phys. Lett. **90**, 033508 (2007).
[21]E. U. Rafailov, M. A. Cataluna, and W. Sibbett, "Mode-locked quantum-dot lasers," Nat. Photonics **1**, 395–401 (2007).
[22]A. J. Zilkie, J. Meier, M. Mojahedi, P. J. Poole, P. Barrios, D. Poitras, T. J. Rotter, C. Yang, A. Stintz, K. J. Malloy *et al.*, "Carrier dynamics of quantum-dot, quantum-dash, and quantum-well semiconductor optical amplifiers operating at 1.55 μm," IEEE J. Quantum Electron. **43**, 982–991 (2007).
[23]L. Zhang, I. Kang, A. Bhardwaj, N. Sauer, S. Cabot, J. Jaques, and D. Neilson, "Reduced recovery time semiconductor optical amplifier using p-type-doped multiple quantum wells," IEEE Photonics Technol. Lett. **18**, 2323–2325 (2006).
[24]G. Eisenstein, J. Wiesenfeld, M. Wegener, G. Sucha, D. Chemla, S. Weiss, G. Raybon, and U. Koren, "Ultrafast gain dynamics in 1.5 μm multiple quantum well optical amplifiers," Appl. Phys. Lett. **58**, 158–160 (1991).
[25]A. C. Tropper, A. H. Quarterman, and K. G. Wilcox, "Ultrafast vertical-external-cavity surface-emitting semiconductor lasers," in *Semiconductors and Semimetals* (Elsevier, 2012), Vol. 86, pp. 269–300.
[26]J. Lee, R. Oszwałdowski, C. Gøthgen, and I. Žutić, "Mapping between quantum dot and quantum well lasers: From conventional to spin lasers," Phys. Rev. B **85**, 045314 (2012).
[27]A. H. Quarterman, K. G. Wilcox, V. Apostolopoulos, Z. Mihoubi, S. P. Elsmere, I. Farrer, D. A. Ritchie, and A. Tropper, "A passively mode-locked external-cavity semiconductor laser emitting 60-fs pulses," Nat. Photonics **3**, 729–731 (2009).
[28]D. Waldburger, S. M. Link, M. Mangold, C. G. Alfieri, E. Gini, M. Golling, B. W. Tilma, and U. Keller, "High-power 100 fs semiconductor disk lasers," Optica **3**, 844–852 (2016).
[29]D. Lorenser, D. J. Maas, H. J. Unold, A.-R. Bellancourt, B. Rudin, E. Gini, D. Ebling, and U. Keller, "50-GHz passively mode-locked surface-emitting semiconductor laser with 100-mW average output power," IEEE J. Quantum Electron. **42**, 838–847 (2006).
[30]M. Laemmlin, G. Fiol, C. Meuer, M. Kuntz, F. Hopfer, A. R. Kovsh, N. N. Ledentsov, and D. Bimberg, "Distortion-free optical amplification of 20–80 GHz modelocked laser pulses at 1.3 μm using quantum dots," Electron. Lett. **42**, 697–699 (2006).
[31]G. Fiol, D. Arsenijević, D. Bimberg, A. Vladimirov, M. Wolfrum, E. Viktorov, and P. Mandel, "Hybrid mode-locking in a 40 GHz monolithic quantum dot laser," Appl. Phys. Lett. **96**, 011104 (2010).
[32]A. Zhukov, M. Maksimov, and A. Kovsh, "Device characteristics of long-wavelength lasers based on self-organized quantum dots," Semiconductors **46**, 1225–1250 (2012).
[33]C. Berger, C. Möller, P. Hens, C. Fuchs, W. Stolz, S. W. Koch, A. Ruiz Perez, J. Hader, and J. V. Moloney, "Novel type-II material system for laser applications in the near-infrared regime," AIP Adv. **5**, 047105 (2015).
[34]C. Möller, C. Fuchs, C. Berger, A. Ruiz Perez, M. Koch, J. Hader, J. V. Moloney, S. W. Koch, and W. Stolz, "Type-II vertical-external-cavity surface-emitting laser with Watt level output powers at 1.2 μm," Appl. Phys. Lett. **108**, 071102 (2016).
[35]C. Fuchs, A. Baeumner, A. Brueggemann, C. Berger, C. Moeller, S. Reinhard, J. Hader, J. V. Moloney, S. W. Koch, and W. Stolz, "Temperature-dependent spectral properties of (GaIn) As/Ga (AsSb)/(GaIn) As W-quantum well heterostructure lasers," arXiv:2012.01522 (2020).
[36]I. Kilen, S. W. Koch, J. Hader, and J. Moloney, "Mode-locking in vertical external-cavity surface-emitting lasers with type-II quantum-well configurations," Appl. Phys. Lett. **114**, 252102 (2019).
[37]M. Stein, C. Lammers, P.-H. Richter, C. Fuchs, W. Stolz, M. Koch, O. Vänskä, M. J. Weseloh, M. Kira, and S. W. Koch, "Dynamics of charge-transfer excitons in type-II semiconductor heterostructures," Phys. Rev. B **97**, 125306 (2018).

[38]M. Fey, M. Stein, C. Fuchs, W. Stolz, K. Volz, and S. Chatterjee, "Phase relaxation control in heterostructures featuring charge-transfer excitons," Phys. Rev. B **106**, 165303 (2022).
[39]M. Kira and S. W. Koch, *Semiconductor Quantum Optics* (Cambridge University Press, 2011).
[40]H. Haug and S. W. Koch, *Quantum Theory of the Optical and Electronic Properties of Semiconductors* (World Scientific Publishing Company, 2009).
[41]W. W. Chow, S. W. Koch, and M. I. Sargent, *Semiconductor-Laser Physics* (Springer Science & Business Media, 2012).
[42]S. L. Chuang, "Efficient band-structure calculations of strained quantum wells," Phys. Rev. B **43**, 9649 (1991).
[43]See http://www.nlcstr.com/publications.htm and http://www.nlcstr.com/examples0.htm for more details about the microscopic approach.
[44]J. Hader, J. V. Moloney, S. W. Koch, I. Vurgaftman, and J. R. Meyer, "Microscopic analysis of mid-infrared type-II 'W' diode lasers," Appl. Phys. Lett. **94**, 061106 (2009).
[45]C. Fuchs, C. Berger, C. Möller, M. Weseloh, S. Reinhard, J. Hader, J. V. Moloney, S. W. Koch, and W. Stolz, "Electrical injection type-II (gain) As/Ga(AsSb)/(GaIn) As single 'W'-quantum well laser at 1.2 μm," Electron. Lett. **52**, 1875–1877 (2016).
[46]C. Lammers, M. Stein, C. Berger, C. Möller, C. Fuchs, A. Ruiz Perez, A. Rahimi-Iman, J. Hader, J. Moloney, W. Stolz *et al.*, "Gain spectroscopy of a type-II VECSEL chip," Appl. Phys. Lett. **109**, 232107 (2016).
[47]S. Weiss, J. Wiesenfeld, D. Chemla, G. Raybon, G. Sucha, M. Wegener, G. Eisenstein, C. Burrus, A. Dentai, U. Koren *et al.*, "Carrier capture times in 1.5 μm multiple quantum well optical amplifiers," Appl. Phys. Lett. **60**, 9–11 (1992).

II - Optical Stark effect in type-II semiconductor heterostructures, Ref. [76]

F. Schäfer, A. Trautmann, C. Ngo, J. T. Steiner, C. Fuchs, K. Volz, F. Dobener, M. Stein, T. Meier and S. Chatterjee

Abstract

Charge-transfer excitons feature a permanent dipole moment introduced by the spatial charge separation of electron and hole wave functions. This directly influences and qualitatively modifies the coherent nonlinear optical response monitored in high-quality (Ga,In)As/Ga(As,Sb) type-II heterostructures through an optical-pump optical-probe experiment. A microscopic analysis based on the semiconductor Bloch equations reveals that the spatial inhomogeneity native to such type-II heterostructures introduces already on the Hartree-Fock a finite coupling between excitons of opposite spins which is pivotal for optical Stark effect experiments. This result in a blueshift of the charge-transfer exciton when pumping below the resonance for both, co-circular and counter-circular polarization configurations, contrary to well-known and observed shifts of spatially direct exciton resonances.

Contribution

I designed the setup with MS and SC, built it with MS, and specified the requirements for the measurement software which was developed by FD. Measurements were conducted by MS and me. The experimental data were analyzed by me, and I created the graphical representations. The manuscript was written and improved in collaboration with AT, MS, TM, and SC.

Optical Stark effect in type-II semiconductor heterostructures

F. Schäfer,[1] A. Trautmann,[2] C. Ngo,[2] J. T. Steiner,[2] C. Fuchs,[3] K. Volz,[3]
F. Dobener,[1] M. Stein,[1] T. Meier,[2] and S. Chatterjee[1,*]

[1]*Institute of Experimental Physics I and Center for Materials Research (LaMa), Justus-Liebig-University Giessen, Heinrich-Buff-Ring 16, D-35392 Giessen, Germany*

[2]*Department of Physics, Paderborn University, Warburger Strasse 100, D-33098 Paderborn, Germany*

[3]*Structure & Technology Research Laboratory (WZMW), Philipps-University Marburg, Hans-Meerwein-Straße 6, D-35032 Marburg, Germany*

(Received 9 October 2023; accepted 16 January 2024; published 2 February 2024)

Charge-transfer excitons feature a permanent dipole moment introduced by the spatial charge separation of electron and hole wave functions. This directly influences and qualitatively modifies the coherent nonlinear optical response monitored in high-quality (Ga, In)As/Ga(As, Sb) type-II heterostructures through an optical-pump optical-probe experiment. A microscopic analysis based on the semiconductor Bloch equations reveals that the spatial inhomogeneity native to such type-II heterostructures introduces already on the Hartree-Fock a finite coupling between excitons of opposite spins which is pivotal for optical Stark effect experiments. This result in a blueshift of the charge-transfer exciton when pumping below the resonance for both, co-circular and counter circular polarization configurations, contrary to well-known and observed shifts of spatially direct exciton resonances.

DOI: 10.1103/PhysRevB.109.075301

I. INTRODUCTION

The nonlinear optical response of excitons has been a topic of great interest in condensed-matter physics for several decades [1,2]. In particular, the nonlinear optical response of spatially direct excitons has been extensively investigated. These quasiparticles dominate the spectral responses in the vicinity of the band gap and are very pronounced in low-dimensional systems such as two-dimensional (2D) materials or, historically, in type-I semiconductor quantum well (QW) systems. The quality of the latter structures have been continuously advanced for many decades, which has consistently led to a deeper understanding of the underlying microscopic physics [1,3–5]. Consequently, semiconductor QW structures are at the heart of many virtually indispensable devices such as semiconductor lasers. This presumably most wide-spread technological application relies on population inversion or, physically speaking on the charge-carrier dynamics. Others, particularly switching applications more often rely on even faster electric field related effects such as the quantum-confined Stark effect [6]. It is widely used in the development of electro-optic modulators [5,7], optical switches [8,9], optoelectronic logic [10], and similar devices. The related optical Stark effect in semiconductor quantum structures is lately being applied in the growing fields of quantum information processing [11,12] and quantum cryptography [13,14].

Recently, high-quality type-II heterostructures featuring spatially indirect charge-transfer excitons (CTXs) as the lowest-energy resonances have become available [15–18]. These structures are composed of two different materials with different band offsets, creating a type-II band alignment at their interface. This inherently results in a spatial separation of the electron wave functions and the hole wave functions. In turn, several significant differences compared with the established type-I QW systems result such as the CTXs featuring a nonzero permanent dipole moment. Most prominently, however, the type-II transition is shifted toward lower energies. Consequently, such heterostructures appear ideal for laser applications in the near infrared and midinfrared, e.g., as active media in W-type semiconductor laser structures [19–21]. They feature a broad gain bandwidth [18] while exhibiting lower Auger losses in the constituent materials [22–24]. These advantageous features should also render such structures viable candidate systems for other devices exploiting their nonlinearities. However, their coherent nonlinear response remains virtually unexplored to date. Previous studies on the influence of carrier-order correlation effects have focused on pump-probe (PP) experiments in type-I heterostructures [25–28]. To comprehend the fundamental physical properties of CTXs more closely, it is essential to consider the spatially separated excitations, which inherently result in a net permanent dipole moment. Furthermore, they exhibit a finite coupling between excitons with opposite spins, which is already present on the Hartree-Fock (HF) level [29]. This coupling plays a crucial role for absorption changes when opposite circularly polarized pump and probe pulses are employed for studying the optical Stark effect.

In this paper, we discuss the influence of carrier-correlation effects on the pump-induced absorption and present an analysis in the coherent $\chi^{(3)}$ limit [26,27,30–36]. Section II presents the type-II QW structure, including the relevant selection

*sangam.chatterjee@physik.uni-giessen.de

rules, gives the relevant details about the PP setup, summarizes the experimental parameters, and presents prototypical data for the nonlinear optical response. These are analyzed using a microscopic theory based on the semiconductor Bloch equations (SBE) [34,35] incorporating coherent biexcitonic many-body correlations up to the third order in the optical fields. Section III, introduces this, briefly describing the one-dimensional (1D) tight-binding model by introducing the relevant equations of motion to determine the nonlinear response within the coherent $\chi^{(3)}$ limit. This work focuses on the nonlinear optical response of CTX resonance for excitations detuned below its transition energy and compares with the established observations for the energetically higher type-I exciton transitions as a reference. Varying the magnitude of the permanent dipole moment contribution clearly dominates the spectral changes observed at the CTX transition energies while having virtually no influence on the spatially direct transitions because they do not feature any such contribution. The comparison of the differential absorption spectra in Sec. IV shows the qualitatively excellent agreement between experiment and theory. The microscopic analysis thus clearly reveals that the spatial inhomogeneity native to CTXs results in additional Coulomb related contributions. Therefore, these additional contributions to the pump-induced absorption changes need to be considered even at the HF level to correctly describe the CTX dynamics for all high-quality systems containing charge-transfer contributions, including molecular heterostructures or 2D heterostructures unless such intricate intrinsic spectral features are fogged by disorder or defect-related signatures.

II. EXPERIMENTAL SETUP AND PROCEDURES

A 5 kHz repetition rate regenerative amplifier system generates 50 fs pulses centered around 800 nm with a pulse energy of 1.6 mJ. Approximately 30% of the amplifier emission is used to generate a white-light supercontinuum in a 6-mm-thick sapphire crystal, while the remaining 70% drives an optical parametric amplifier (OPA). The main output of the OPA provides short pulses with tunable central wavelength. These are spectrally tailored, using a grating pulse shaper set up in reflection geometry, to a full width at half maximum (FWHM) of about 2.71 meV/1.6 nm resulting in a pulse duration of 1.04 ps. The excitation beam is focused onto the sample to a spot size of 300 μm diameter. The sample is held at liquid helium temperatures in a cold-finger cryostat. A wedge beam splitter divides the white-light beam into two. One part serves as a reference pulse which is directly propagated to the spectrometer. The other part is focused to a spot diameter of 200 μm on the sample where it probes the sample's excitation-induced absorption changes. Both white-light beams are spectrally analyzed using an imaging spectrometer equipped with a 600 lines/mm grating and a scientific complementary metal-oxide semiconductor (sCMOS) camera (see Fig. 1). It has 2160 lines that can be read out individually and allows multiple lines to be combined into a region of interest (ROI). The imaging allows for reading out both pulses simultaneously and independently. This enables the comparison of spectra between the two pulses, leading to the calculation of a transfer function T_f that converts the spectrum of the reference

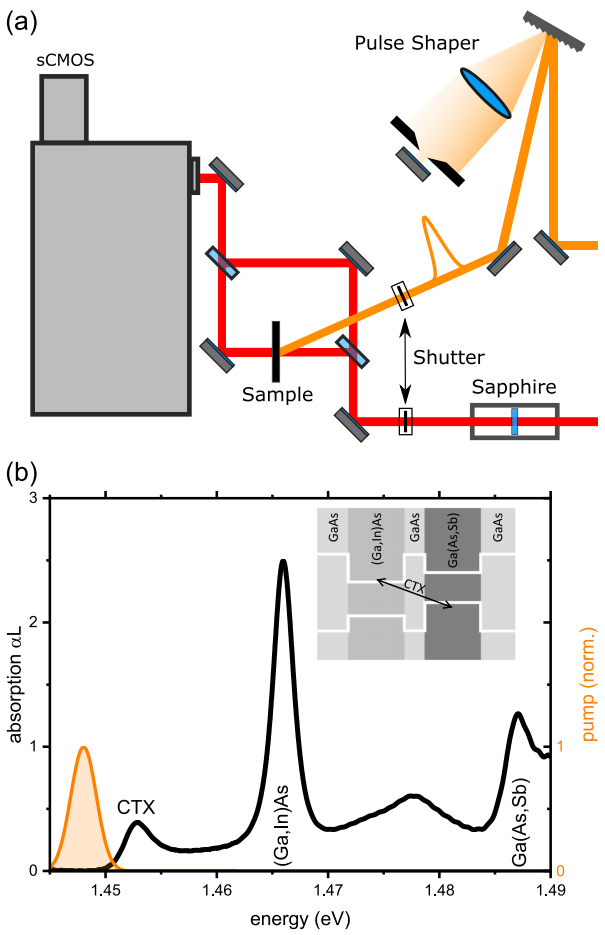

FIG. 1. (a) Schematic of the experimental setup for optical pump-optical probe measurements, incorporating a pulse shaper for the pump pulse. Two wedge beam splitters are employed to establish a reference path, compensating for white-light fluctuations, in conjunction with a sCMOS chip and a transfer function. Mechanical shutters are utilized to capture background and photoluminescence spectra, as well as to measure the transmission through the sample. (b) The linear absorption spectrum of the sample (black line) superimposed with the applied pump pulse (shaded orange) at an energy of 1.448 eV (4.8 meV below the CTX). The inset illustrates the schematic band structure of the sample, emphasizing the spatially indirect CTX transition indicated by an arrow within a type-II heterostructure system.

pulse (T_{ref}) into the spectrum of the pulse transmitted through the unexcited sample. Consequently, introducing the optical excitation then simultaneously determines the transmission through the excited sample (T_P) and the transmission through the unexcited sample (T_0). Taking into account the photoluminescence background (T_{Pl}) and the scattered light background (T_{Bg}) in both paths at the beginning of each set of pump pulse parameters then yields the differential absorption $\Delta\alpha L$ for each time step according to

$$\Delta\alpha L = -\ln\left(\frac{T_P - T_{Pl}}{T_f(T_{ref} - T_{Bg})}\right). \quad (1)$$

Furthermore, removing the sample from the beam path yields the transfer function that converts the reference path to the spectrum of the pulse transmitted through the sample holder. The sample is then placed back into the beam path, allowing us to measure the transmission through the unexcited sample and calculate the linear absorption.

The sample under investigation is a type-II band alignment multi QW sample grown using metal organic vapor phase epitaxy in an AIXTRON AIX 200 Gas Foil Rotation (GFR) reactor system. The active layer of the type-II system comprises 50 repetitions of compressively strained (Ga, In)As/GaAs/Ga(As, Sb) layers, which are separated by thick, tensilely strained GaAs/Ga(As, P)/GaAs barriers. The latter provide strain compensation and electronic decoupling of the individual repetitions. High-resolution x-ray diffraction and atomic force microscopy analyses confirm the layer thicknesses of 7.7, 7.5, and 1 nm for $Ga_{0.942}In_{0.058}As$, $GaAs_{0.967}Sb_{0.033}$, and the GaAs interlayer, respectively [15]. In these compositions, the maximum of the electron wave function in the conduction band is in the (Ga, In)As layer, while the center-of-gravity of the highest energy hole wave function in the valence band is in the Ga(As, Sb) layer. The intentionally low concentrations of In and Sb result in shallow QWs with depths of only a few tens of meV. In combination with the electronically almost negligible thin interlayer, this leads to a significant overlap of the electron and hole wave functions. Consequently, these high-quality heterostructures show several clearly resolved resonances in the linear absorption spectrum, exhibiting significant oscillator strength. The lowest-energy transition is associated with the CTX and is clearly visible despite the lower oscillator strength expected for spatially separated transitions. The higher-energy resonances are associated with spatially direct exciton transitions. Figure 1 shows the linear absorption of the unexcited type-II sample (black line). The linear absorption spectrum reveals three distinct peaks at 1.452, 1.467, and 1.487 eV. The lowest energy peak corresponds to the CTX transition, the other two to the type-I heavy-hole exciton peak in the (Ga, In)As layer and the Ga(As, Sb) layer, respectively. A fourth peak at 1.478 eV is attributed to the transition from the first hole state in Ga(As, Sb) to the second electron state in the (Ga, In)As quantum well. The light holes are intentionally shifted to higher energies due to residual strain to result in more clear polarization-resolved features.

III. THEORETICAL DESCRIPTION

The SBE represent a powerful framework to describe the optical properties of virtually all semiconducting systems. Due to their microscopic nature, i.e., the inclusion of relevant states and processes in the system Hamiltonian and the systematic treatment of many-body interactions, they even offer predictive capabilities including the interplay and formation as well as decay dynamics of many-body correlations [37,38].

The description of heterostructures featuring charge-transfer excitons requires the inclusion of a nonlocal dipole interaction, i.e., the permanent dipole moment of the charge-transfer exciton in addition to its interband transition dipole moment. This permanent dipole moment is not present for quasiparticles in spatially symmetric systems such as excitons in type-I quantum wells.

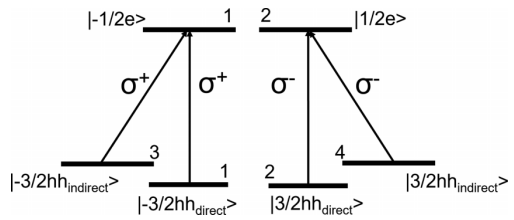

FIG. 2. Schematical illustration of the energetically lowest optical interband transitions within a type-II QW system. The selection corresponds to zincblende materials, such as GaAs-based semiconductor nanostructures. The numbers label the considered heavy-hole valence bands and the conduction bands.

Therefore, to theoretically describe the optical excitations of the type-II quantum-well system investigated here, besides spatially direct optical intrawell transitions, also spatially indirect optical interwell transitions need to be considered. In the latter process, the photoexcitation moves the electron from one well to the other. The interband excitations with the lowest energies can qualitatively be described by the six level scheme given in Fig. 2. This scheme visualizes the relevant polarization selection rules for the interband transitions that start from the energetically highest heavy-hole bands of the two quantum wells. The type-I intrawell optical transitions are given by the well-established selection rules for zincblende materials near the Γ point, i.e., circularly polarized light labeled by the subscripts "direct" [34,35]. The spatially indirect transitions of the type-II heterostructure are accounted for by including two additional valence bands ($v_{3,4}$) which are located in the other well. These optical transitions also follow the well-established selection rules for zincblende materials, i.e., involve circularly polarized transitions which are labeled by the subscripts "indirect." As described in Sec. II, in the investigated type-II heterostructure the transition frequency of the indirect excitations is smaller than that of the direct excitations.

It has been shown in several previous studies that many-body correlations, i.e., terms describing effects of the many-body Coulomb interaction beyond the time-dependent Hartree-Fock approximation, are required in order to properly describe the dependence of pump-probe and four-wave-mixing experiments on the polarization directions of the incident pulses, see, e.g., Refs. [26,27,33,34,35].

In this paper, we include biexcitonic coherences which represent four-particle correlations within the framework of the coherent $\chi^{(3)}$ limit in our theoretical and numerical analysis. Numerically, we evaluate the resulting SBE for a one-dimensional tight-binding model, see, e.g., Refs. [26,27,34–36].

We extend the models used previously by adding the indirect transitions including the permanent dipole moment of the charge-transfer exciton.

The Hamiltonian that describes the nonlinear optical response is given by [34,35]

$$\hat{H} = \hat{H}_0 + \hat{H}_{L-M} + \hat{H}_{\mathrm{C}}. \tag{2}$$

It includes the single-particle Hamiltonian $\hat{H}_0$, the dipole interaction between light and matter $\hat{H}_{L-M}$, and the many-body Coulomb interaction $\hat{H}_C$. The Hamiltonian $\hat{H}_C$ contains the repulsion between electrons, the repulsion between holes, and the electron-hole attraction and gives rise to the formation of bound electron-hole complexes such as excitons and biexcitons.

As is well known, the many-body Coulomb interaction $\hat{H}_C$ introduces an infinite hierarchy problem where lower-order equations of motion couple to higher orders. Here, we truncate the many-body hierarchy by limiting the optical response to the third-order and additionally assume fully coherent dynamics, i.e., we apply the dynamics-controlled truncation scheme to obtain the SBE in the coherent $\chi^{(3)}$ limit [18,26,27,30,32,34–36].

This yields a closed set of differential equations that describe the coupled dynamics of single-exciton p_{12}^{vc} and two-exciton coherences $\overline{B}_{ba12}^{v'c'vc}$. For the one-dimensional tight-binding model the equation of motion for the single-exciton coherence reads [26,35,36]

$$\begin{aligned}
-i\hbar\frac{d}{dt}p_{12}^{vc} = &-\sum_j T_{2j}^{c} p_{1j}^{vc} - \sum_i T_{i1}^{v} p_{i2}^{vc} + V_{12}^{vc} p_{12}^{vc} \\
&+ \mathbf{E}(t)\cdot\Bigg[\left(\mu_{12}^{vc}\right)^* - \sum_{abv'c'}\left(\mu_{1b}^{vc'}\right)^*\left(p_{ab}^{v'c'}\right)^* p_{a2}^{v'c} \\
&+ \left(\mu_{b2}^{v'c}\right)^*\left(p_{ba}^{v'c'}\right)^* p_{1a}^{vc'}\Bigg] \\
&+ \sum_{abv'c'}\left(V_{a2}^{c'c} - V_{a1}^{c'v} - V_{b2}^{v'c} + V_{b1}^{v'v}\right) \\
&\times\left[\left(p_{ba}^{v'c'}\right)^* p_{b2}^{v'c} p_{1a}^{vc'} - \left(p_{ba}^{v'c'}\right)^* p_{ba}^{v'c'} p_{12}^{vc}\right. \\
&\left.- \left(p_{ba}^{v'c'}\right)^* \overline{B}_{ba12}^{v'c'vc}\right]. \qquad (3)
\end{aligned}$$

Here, the subscripts i and j denote sites in real space. The considered relevant valence and conduction bands are labeled by $v = 1, 2, 3, 4$ and $c = 1, 2$, respectively, see Fig. 2. The matrices $T_{i,j}^{v/c}$ include the energies of electrons and holes on their diagonals and the tight-binding coupling in the first off-diagonals. The equation of motion for the single-exciton amplitude, Eq. (3), includes in the first line the band energies and tight-binding couplings, and the electron-hole attraction V_{12}^{vc}. The second and third lines of Eq. (3) describe the light-matter interaction including the linear source term $[\mathbf{E}(t)\cdot\boldsymbol{\mu}]$ and nonlinearities which are known as Pauli-blocking or phase-space filling $[\mathbf{E}(t)\cdot\boldsymbol{\mu}p^*p]$ [34,35,39]. The Coulomb interaction gives rise to two inhomogeneities, the first-order Coulomb interaction ($CI_{1st} \propto p^*pp$), which represents a nonlinearity that arises in the time-dependent Hartree-Fock approximation, and the term ($CI_{\mathrm{corr}} \propto Vp^*B$) [26,33], which describes biexcitonic many-body correlations. Due to the additive appearance of the different inhomogeneities in Eq. (3) the contributions to the differential absorption from the three nonlinear processes can be analyzed separately and the total signal is simply given by their sum. The equation of motion for the two-exciton coherence $\overline{B}_{ba12}^{v'c'vc}$ is given by [26,35,36]

$$\begin{aligned}
-i\hbar\frac{d}{dt}\overline{B}_{ba12}^{v'c'vc} = &-\sum_i\Big(T_{2i}^{c'}\overline{B}_{ba1i}^{v'c'vc} + T_{i1}^{v'}\overline{B}_{bai2}^{v'c'vc} \\
&+ T_{ai}^{c'}\overline{B}_{bi12}^{v'c'vc} + T_{ib}^{v'}\overline{B}_{ia12}^{v'c'vc}\Big) \\
&+ \left(V_{ba}^{v'c'} + V_{b2}^{v'c} + V_{1a}^{vc'} + V_{12}^{vc}\right. \\
&\left.- V_{b1}^{v'v} - V_{a2}^{c'c}\right)\overline{B}_{ba12}^{v'c'vc} \\
&- \left(V_{ba}^{v'c'} + V_{12}^{vc} - V_{b1}^{v'v} - V_{a2}^{c'c}\right)p_{1a}^{vc'}p_{b2}^{v'c} \\
&+ \left(V_{1a}^{vc'} + V_{b2}^{v'c} - V_{b1}^{v'v} - V_{a2}^{c'c}\right)p_{ba}^{v'c'}p_{12}^{vc}. \qquad (4)
\end{aligned}$$

The first two lines of Eq. (4) contain the electronic energies and the tight-binding couplings. The third line includes the six terms describing the Coulomb interaction between the four particles, i.e., the four attractive electron-hole interaction terms and the two repulsive ones between two electrons and two holes, respectively. The two-exciton amplitude $\overline{B}_{ba12}^{v'c'vc}$ describes both bound biexcitons, which can form by the attractive interaction between two excitons with opposite spin, and unbound continuum states. The sources of $\overline{B}_{ba12}^{v'c'vc}$ are induced by the many-body Coulomb interaction Vpp.

For type-I structures, the linear response originating from intrawell excitations is fully described by p^{11} and p^{22}. Additional contributions from the interwell exciton coherences p^{31} and p^{42} have to be considered for type-II structures. Two-exciton coherences $\overline{B}$ are generated in second order by interacting once with the pump and once with the probe field. For co-circular excitation conditions ($\sigma^+\sigma^+$), only unbound continuum states are excited, whereas bound biexcitons contribute for counter-circularly polarized fields ($\sigma^+\sigma^-$). The total nonlinear response in third order within the coherent $\chi^{(3)}$ limit is given by p^{11} (X), p^{22} (X), p^{31} (CTX), and p^{42} (CTX).

The nonlinear optical response depends strongly on the polarization directions of the pump and probe fields. We therefore account for the vector nature of the dipole matrix element $\boldsymbol{\mu}$, the electric field $\mathbf{E}$, and the resulting optical polarization $\mathbf{P}$. The latter is obtained by summing up over all microscopic single-exciton polarizations $\mathbf{P}$ [34,35]:

$$\mathbf{P} = \sum_{ijvc}\boldsymbol{\mu}_{ij}^{vc}p_{ij}^{vc}. \qquad (5)$$

The experiment is performed with two pulses that propagate in the directions $\mathbf{k}_1$ and $\mathbf{k}_2$. Hence, we describe the incident electric field within the rotating wave approximation (RWA) by [26,35]

$$\begin{aligned}
\mathbf{E}(t) &= \mathbf{e}_1E_1(t)e^{i(\mathbf{k}_1\cdot\mathbf{r}-\omega_1t)} + \mathbf{e}_2E_2(t)e^{i(\mathbf{k}_2\cdot\mathbf{r}-\omega_2t)}, \\
&\text{with } E_1(t) \propto e^{-\left(\frac{t+\tau}{\Delta t_1}\right)^2} \text{ and } E_2(t) \propto e^{-\left(\frac{t}{\Delta t_2}\right)^2}. \qquad (6)
\end{aligned}$$

The polarization vectors of the electric fields are denoted $\mathbf{e}_1$ and $\mathbf{e}_2$, ω_1 and ω_2 (Δt_1 and Δt_2) represent their central frequencies (duration), respectively, and τ denotes the time delay between the two pulses. Following Refs. [26,34,35] we obtain the differential absorption which is measured in a pump-probe

experiment via

$$\Delta\alpha(\omega,\tau) \propto \mathrm{Im}\left[\int (\mathbf{e}_2)^* \cdot \delta\mathbf{P}(t,\tau)e^{i\omega t}dt\right]. \tag{7}$$

The numerical parameters in this simulation are quite similar to those used in several previous studies, see, e.g., Ref. [35] and references therein. These values are chosen in order to match known properties of the investigated quantum-well systems, e.g., the exciton and biexciton binding energies, as well as the dephasing times, and the strength of exciton resonances in the linear absorption. Here we use tight-binding couplings $T_{ij}^{v/c} = J_{v/c}$ with $|i-j| = 1$ of $J_c = 14$ meV and $J_v = 0.7$ meV describing the couplings between neighboring sites in the conduction bands and the heavy-hole (hh) bands, respectively.

The dipole matrix elements are denoted μ_{ij}^{vc} and the nonvanishing transitions are given by

$$\mu_{ij}^{11} = \delta_{ij}\frac{\mu_{\text{type I}}}{\sqrt{2}}\begin{pmatrix}1\\ i\end{pmatrix}, \quad \mu_{ij}^{22} = \delta_{ij}\frac{\mu_{\text{type I}}}{\sqrt{2}}\begin{pmatrix}1\\ -i\end{pmatrix},$$

$$\mu_{ij}^{31} = \delta_{ij}\frac{\mu_{\text{type II}}}{\sqrt{2}}\begin{pmatrix}1\\ i\end{pmatrix}, \quad \mu_{ij}^{42} = \delta_{ij}\frac{\mu_{\text{type II}}}{\sqrt{2}}\begin{pmatrix}1\\ -i\end{pmatrix}. \tag{8}$$

Thus there is no optical coupling between the spin subspaces, i.e., $\mu_{ij}^{12} = \mu_{ij}^{21} = 0$ and $\mu_{ij}^{32} = \mu_{ij}^{41} = 0$. For the relative strength of the direct and indirect dipole matrix elements we use $\mu_{\text{type II}} = 0.4\mu_{\text{type I}}$ which provides good agreement with the measured ratio of the optical absorption of the direct and the indirect exciton. Additionally, we use phenomenological dephasing times $\frac{1}{\gamma_p}$ and $\gamma_B = 2\gamma_p$. The dephasing times of the X and CTX are taken as $T_p = 0.8$ ps and $T_p = 4$ ps, respectively, which again matches experimental results [17].

The Coulomb matrix elements are given by

$$V_{ij}^{vv'} = U_0\frac{1}{|i-j| + a^{vv'}}, \tag{9}$$

with the regularization parameter $a^{vv'}$. For the Coulomb interactions within a quantum well, the regularization parameter is chosen, as in several previous studies, see, e.g., [35] and references therein, as $a^X = 0.5$. Together with taking the strength of the interaction as $U_0 = 8.3$ meV this leads to a binding energy of the direct exciton X of about 7 meV and also a binding energy of the direct biexciton which matches experimental results [15]. To describe the reduced attraction between electrons and holes in different quantum wells the regularization parameters a^{31} and a^{42} are increased to $a^{CTX} = 0.72$ which leads to a CTX binding energy of about 4.7 meV, in agreement with experiment.

Within our model, for type-I QW systems the differential absorption for counter-circularly polarized pump and probe pulses ($\sigma^+\sigma^-$) is entirely given by the correlation contribution CI_{corr} [26,27,35].

For $\sigma^+\sigma^-$ excitation the Pauli blocking (PB) contribution vanishes since the optical transitions do not couple the two spin subspaces. The CI_{1st} Hartree-Fock contribution $\propto p_{ba}^{v'c'*} p_{ba}^{v'c'} p_{12}^{vc}$ has a structure that in general may lead to a coupling between the spin subspaces:

$$\partial_t p_{12}^{vc} \propto \sum_{abv'c'} \left(V_{a2}^{c'c} - V_{a1}^{c'v} - V_{b2}^{v'c} + V_{b1}^{v'v}\right)\left(p_{ba}^{v'c'}\right)^* p_{ba}^{v'c'} p_{12}^{vc}. \tag{10}$$

However, for homogeneous systems the right-hand side of Eq. (10) vanishes. This can be easily understood by the fact that, in a homogeneous system, the relation $p_{ba}^{vc} = p_{ab}^{vc}$ is fulfilled since the electron-hole coherence depends only on the relative distance. Thus, the product between the coherences on the right-hand side of Eq. (10) is a symmetric function $g(a,b) = g(b,a) = (p_{ba}^{v'c'})^* p_{ba}^{v'c'} p_{12}^{vc} = (p_{ab}^{v'c'})^* p_{ab}^{v'c'} p_{12}^{vc}$ with respect to interchanging the site indices a and b. However, the prefactor $f(a,b) = (V_{a2}^{c'c} - V_{a1}^{c'v} - V_{b2}^{v'c} + V_{b1}^{v'v})$ changes its sign when a and b are interchanged. Consequently, the sum over the sites a and b appearing in Eq. (10) vanishes and a CI_{1st} contribution does not exist in a homogeneous system [26,27,29,35].

The situation changes when spatially indirect transitions are included by the valence bands $v = 3, 4$, see Fig. 2. In this case $p_{ba}^{vc} = p_{ab}^{vc}$ is still fulfilled and a and b denote spatial sites in a direction within the plane of the quantum wells. However, $f(a,b) = (V_{a2}^{c'c} - V_{a1}^{c'v} - V_{b2}^{v'c} + V_{b1}^{v'v})$ is no longer asymmetric with respect to interchanging a and b because we have to take into account the different Coulomb interactions within one well and between the two wells, i.e., the different regularization parameters a^X and a^{CTX}. This leads to a finite coupling of the spin subspaces already on the time-dependent Hartree-Fock level which, as is shown below, significantly modifies the nonlinear optical response of the CTX. As a result, in particular, the polarization direction dependence of the absorption changes at the CTX differ qualitatively from that at the direct exciton.

IV. RESULTS AND DISCUSSION

Experimental differential absorption signals ($\Delta\alpha L$) obtained at optimal temporal overlap for circularly polarized pump and probe pulses are presented in Fig. 3. The left-hand panel depicts the data for the co-circular polarization geometry while the right-hand panel presents the corresponding data for the counter-circular polarization-geometry data. Significant differential absorption signatures are only observed when the pump and the probe overlap in time. Both polarization configurations exhibit similar spectral characteristics in the differential absorption of the CTX resonance. This includes a discernible bleaching signature accompanied by a substantial blueshift, which remains consistent regardless of the polarization configuration of the pump and probe pulses. However, the differential signal is more pronounced for co-circular polarization compared with the counter-circular polarization configuration.

These coherent nonlinear optical responses of the CTX distinctly contrast the AC Stark effect observed in spatially direct QWs [27,40,41]. Notably, the nonlinearities for the spatially direct exciton resonances in the type-II heterostructure show a behavior consistent with the well-established AC Stark effect in spatially direct structures where lower energy states for electrons or holes are not present in adjacent layers. Co-circularly polarized pulses induce a blueshift in the

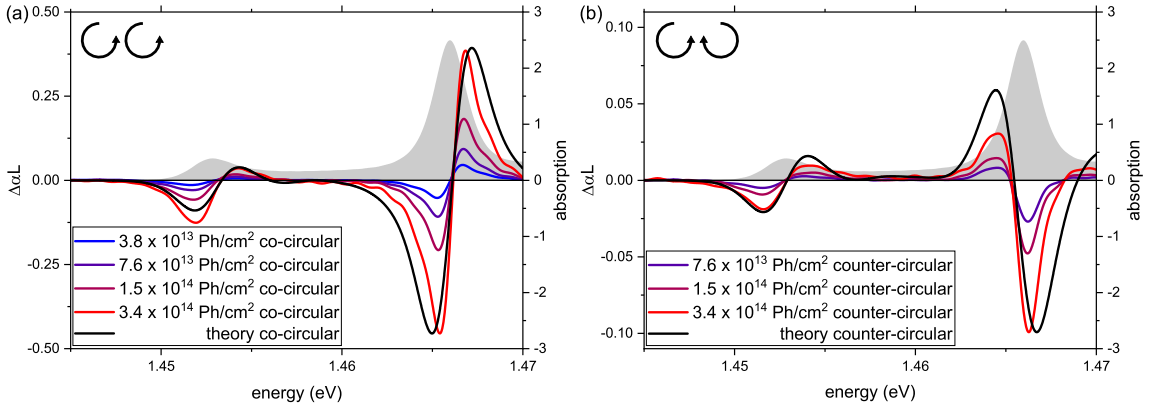

FIG. 3. Differential absorption signals ($\Delta\alpha L$) obtained experimentally for various pump pulse densities. Panel (a) shows data for the co-circular polarization geometry, while panel (b) shows data for the counter-circular polarization geometry. For reference, the linear absorption spectrum of the sample is given as a gray-shaded area. Both polarization configurations show a blueshift and a bleaching of the CTX absorption line while the spatially direct exciton in the (Ga, In)As layer (1.467 eV) exhibits the established responses, i.e., a blueshift for co-circular polarization and a redshift for counter-circular polarization of the pump and probe pulses. The solid black lines in both graphs represent the theoretical curves, normalized with respect to the minimum of the direct exciton absorption signal for the maximum pump density.

spatially direct resonance, while counter-circularly polarized pulses result in a redshift. This observation effectively negates any suggestions that the blueshift observed for the CTX could be attributed to disorder-induced effects.

Comparing the differential absorption spectra of the two types of QW excitons, namely, CTX and spatially direct excitons, in a PP configuration reveals key differences in their nonlinear response when pumping below the CTX resonance. These differences are a direct consequence of the distinct spatial configurations of the electrons and holes in the two types of structures. Comparing the experimental pump-induced absorption changes to the results from the calculations in Fig. 3 clearly shows that the theory correctly describes the AC Stark effect at both, the CTX and the type-I exciton resonance of the (Ga, In)As QW at 1.467 eV [27]. Specifically, both theory and experiment reveal a slightly asymmetric blueshift accompanied by a decrease in absorption at the CTX resonance for both polarization configurations. The nonlinear response at the CTX resonance exhibits similarities to the blueshift observed at the direct excitons in the (Ga, In)As layer when employing co-circularly polarized pulses. However, the additional bleaching of the absorption is specific to the CTX resonance and is not observed at the regular exciton resonance. This high level of agreement indicates that the outlined theoretical framework effectively captures all necessary features. The few remaining differences between the experimental and calculated spectra, particularly in the amount of bleaching at the CTX resonance for co-circularly polarized pulses, suggest the presence of additional factors influencing the nonlinear response at the CTX resonance that are not accounted for in the current theoretical analysis. A clear distinction in the response of the CTX compared with the type-I excitons becomes apparent for counter-circular polarization conditions. In this scenario, the CTX resonance exhibits a blueshift, contrasting with type-I QW heterostructures where the presence of bound biexcitons leads to a redshift. The origin of this blueshift becomes evident through the theoretical switch-off analysis shown in Fig. 4. Here, only the first-order Coulomb interaction leads to a blueshift of the CTX resonance for a counter-circular polarization geometry. This first-order

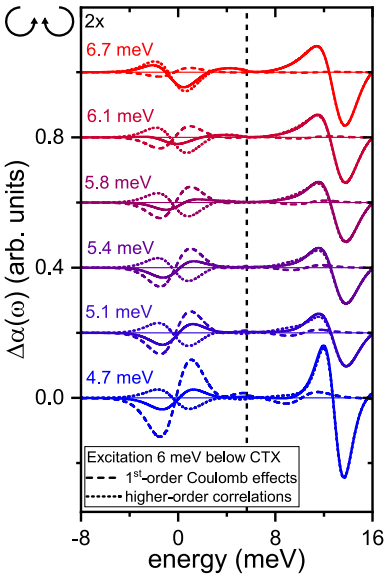

FIG. 4. Variation of the CTX binding energy with a fixed excitation detuning of 6 meV below the CTX resonance for counter-circular pump-probe polarizations. The dashed line corresponds to the first-order Coulomb contributions, while the dotted line represents higher-order Coulomb correlations. At low CTX binding energies, the first-order contributions dominate, inducing a net blueshift. Conversely, for high CTX binding energies, the higher-order correlations become prominent, leading to a redshift of the CTX. Please note that the zero of the energy scale corresponds to the CTX resonance and the CTX components are multiplied by a factor of two for better visibility.

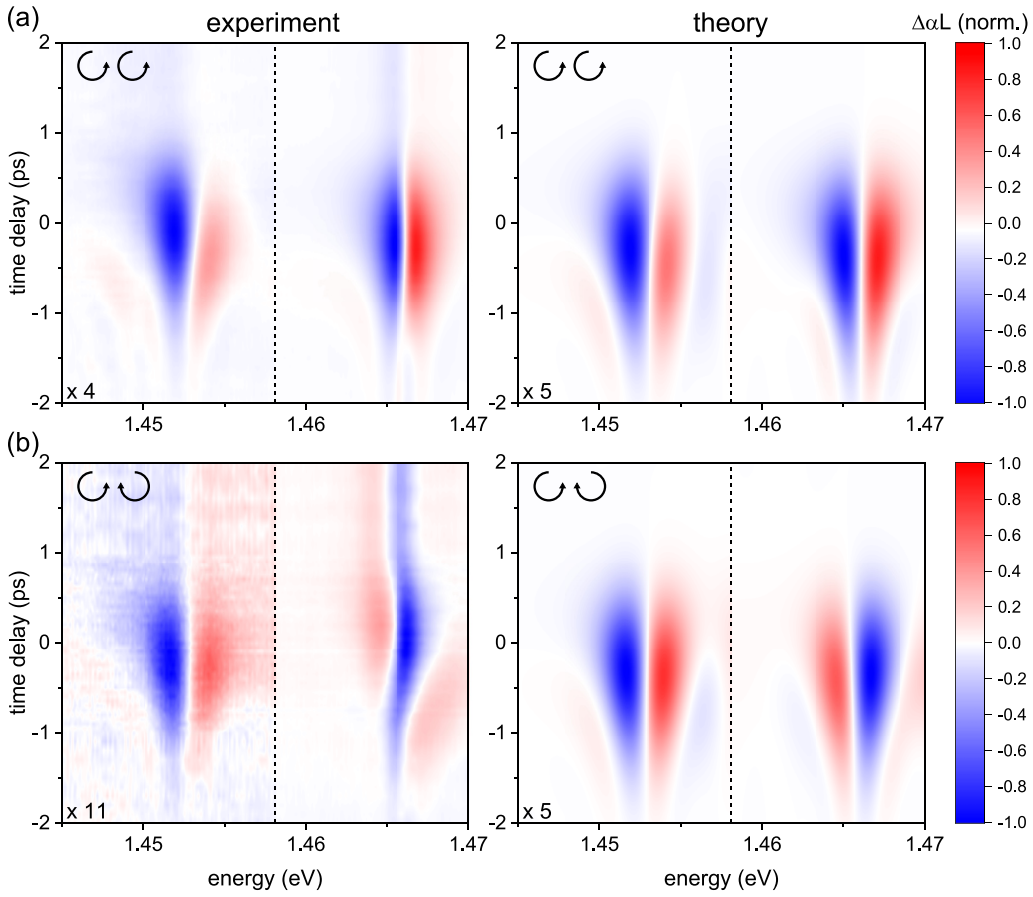

FIG. 5. 2D representation of the dynamics of the $\Delta\alpha L$ signals in both experiment and theory. The top row shows the co-circular polarization configurations for experiment (left) and theory (right). The bottom row shows the corresponding counter-circular polarization configurations. To enhance visibility, both the minimum value of the differential absorption in all contour plots is normalized to -1 at the energy associated with the type-I exciton transition in the (Ga, In)As layer and the lower-energy parts of the spectra containing the CTX (left side of the dotted line) are magnified by the factors are given in the respective bottom-left corners.

Coulomb interaction is uniquely present in inhomogeneous systems and dominates the redshifting higher-order correlations for CTX binding energies below 6 meV.

Closely analyzing the CI_{1st} term reveals that the hole and electron involved correspond to spatially separated layers, with $v = 4$ and $c = 2$, respectively.

Performing calculations for different binding energies of the CTX (which is achieved by varying the regularization parameter a^{CTX} which is described in Sec. III) for a fixed-detuning of 6 meV below the CTX resonance yields observable changes in the absorption response (refer to Fig. 4). A comparatively small binding energy of 4.7 meV, which describes the experimental data well, leads to a blueshift. Increasing the CTX binding energy in the theoretical calculations to around 6 meV leads to the appearance of a bleaching effect only. Here, the first-order contributions and the higher-order correlations are approximately equal and compensate each other. Any further increases of the binding energy weaken the first-order effect while the higher-order effects persist which then results in a redshift of the signal rather than the originally observed blueshift. Notably, at the direct X resonance, only the signal amplitude changes for the different CTX binding energies, while the spectral shift consistently remains a redshift.

The theoretical framework extends beyond spectral properties to include dynamic predictions within the coherent $\chi^{(3)}$ limit, which is applicable to negative time delays and near zero time. This dynamic facet of the analysis is visualized in Fig. 5, where we compare the temporal dynamics of the observed AC Stark shifts between experimental data and theory. Remarkably, our theoretical model not only impeccably reproduces the spectral properties when there is perfect temporal overlap of pump and probe pulses but also provides an accurate description of the temporal evolution of the AC Stark shifts. In particular, we find excellent agreement between the experimental and theoretical dynamics of the AC Stark shift for both the CTXs and type-I excitons, for both the co-circularly polarized pulses and the counter-circularly polarized pulses. However, for the latter case, the type-I transition exhibits a slightly delayed appearance of the redshift in the experimental results compared with the blueshift observed in the CTX resonance which is not reflected in our theoretical predictions.

Additionally, a minor deviation between theory and experiment surfaces at later delay times. Here, the experiment reveals weak spectral features due to residual incoherent excitons in the sample not considered in the theoretical framework. Overall, the remarkable agreement between theory and experiment underlines the comprehensive capability of our applied theoretical framework. It successfully predicts not only the spectral properties but also the intricate temporal dynamics, thereby providing valuable insights into the underlying nonlinear physics governing type-II systems.

V. CONCLUSION

We present a comprehensive experimental and theoretical analysis aimed at revealing the microscopic mechanism behind the optical Stark effect in charge-transfer excitons in high-quality (Ga, In)As/Ga(As, Sb) type-II heterostructures. The experimental pump probe spectra are well described by a microscopic model based on the SBE taking into account the permanent dipole moment inherent to the CTXs. A switch-off analysis reveals its importance for the observed differential absorption features and how it results in a blueshift of the CTX resonance for both, co-circular and counter circular polarization configurations, contrary to shifts of spatially direct exciton resonances.

ACKNOWLEDGMENTS

Financial support from the Deutsche Forschungsgemeinschaft via the Collaborative Research Center SFB 1083 (Project No. 223848855) and the Transregional Collaborative Research Center TRR 142 "Tailored Nonlinear Photonics" (Project No. 231447078, Subproject No. A10) is gratefully acknowledged. We thank the Paderborn Center for Parallel Computing (PC^2) for a computing time grant.

[1] J. Shah, *Ultrafast Spectroscopy of Semiconductors and Semiconductor Nanostructures*, Springer Series in Solid-State Sciences (Springer, Berlin, Heidelberg, 2013).
[2] J. Singh, in *Optical Properties of Condensed Matter and Applications*, edited by J. Singh (John Wiley & Sons, 2006), Vol. 6.
[3] S. Schmitt-Rink, D. Chemla, and D. A. Miller, Adv. Phys. **38**, 89 (1989).
[4] A. Von Lehmen, D. S. Chemla, J. Zucker, and J. P. Heritage, Opt. Lett. **11**, 609 (1986).
[5] Y.-H. Kuo, Y. K. Lee, Y. Ge, S. Ren, J. E. Roth, T. I. Kamins, D. A. Miller, and J. S. Harris, Nature (London) **437**, 1334 (2005).
[6] D. A. B. Miller, D. S. Chemla, T. C. Damen, A. C. Gossard, W. Wiegmann, T. H. Wood, and C. A. Burrus, Phys. Rev. Lett. **53**, 2173 (1984).
[7] M. Stepanenko, I. Kulinich, and I. Yunusov, J. Phys.: Conf. Ser. **1145**, 012028 (2019).
[8] H. Yamamoto, M. Asada, and Y. Suematsu, J. Lightwave Technol. **6**, 1831 (1988).
[9] T. Aizawa, K. Ravikumar, S. Suzaki, T. Watanabe, and R. Yamauchi, IEEE J. Quantum Electron. **30**, 585 (1994).
[10] A. Barenco, D. Deutsch, A. Ekert, and R. Jozsa, Phys. Rev. Lett. **74**, 4083 (1995).
[11] T. Unold, K. Mueller, C. Lienau, T. Elsaesser, and A. D. Wieck, Phys. Rev. Lett. **92**, 157401 (2004).
[12] C. Chakraborty, K. M. Goodfellow, S. Dhara, A. Yoshimura, V. Meunier, and A. N. Vamivakas, Nano Lett. **17**, 2253 (2017).
[13] A. Muller, W. Fang, J. Lawall, and G. S. Solomon, Phys. Rev. Lett. **103**, 217402 (2009).
[14] A. Laucht, J. M. Villas-Bôas, S. Stobbe, N. Hauke, F. Hofbauer, G. Böhm, P. Lodahl, M.-C. Amann, M. Kaniber, and J. J. Finley, Phys. Rev. B **82**, 075305 (2010).
[15] M. Stein, C. Lammers, P.-H. Richter, C. Fuchs, W. Stolz, M. Koch, O. Vänskä, M. J. Weseloh, M. Kira, and S. W. Koch, Phys. Rev. B **97**, 125306 (2018).
[16] C. Meineke, M. Prager, J. Hayes, Q. Wen, L. Z. Kastner, D. Schuh, K. Fritsch, O. Pronin, M. Stein, F. Schäfer, S. Chatterjee, M. Kira, R. Huber, and D. Bougeard, Light: Sci. Appl. **11**, 151 (2022).
[17] M. Fey, M. Stein, C. Fuchs, W. Stolz, K. Volz, and S. Chatterjee, Phys. Rev. B **106**, 165303 (2022).
[18] F. Schäfer, M. Stein, J. Lorenz, F. Dobener, C. Ngo, J. T. Steiner, C. Fuchs, W. Stolz, K. Volz, T. Meier, J. Hader, J. V. Moloney, S. W. Koch, and S. Chatterjee, Appl. Phys. Lett. **122**, 082104 (2023).
[19] C. Berger, C. Möller, P. Hens, C. Fuchs, W. Stolz, S. W. Koch, A. Ruiz Perez, J. Hader, and J. V. Moloney, AIP Adv. **5**, 047105 (2015).
[20] C. Möller, C. Fuchs, C. Berger, A. Ruiz Perez, M. Koch, J. Hader, J. V. Moloney, S. W. Koch, and W. Stolz, Appl. Phys. Lett. **108**, 071102 (2016).
[21] C. Lammers, M. Stein, C. Berger, C. Möller, C. Fuchs, A. Ruiz Perez, A. Rahimi-Iman, J. Hader, J. V. Moloney, W. Stolz, S. W. Koch, and M. Koch, Appl. Phys. Lett. **109**, 232107 (2016).
[22] G. G. Zegrya and A. D. Andreev, Appl. Phys. Lett. **67**, 2681 (1995).
[23] J. I. Malin, J. R. Meyer, C. L. Felix, J. R. Lindle, L. Goldberg, C. A. Hoffman, F. J. Bartoli, C.-H. Lin, P. C. Chang, S. J. Murry, R. Q. Yang, and S.-S. Pei, Appl. Phys. Lett. **68**, 2976 (1996).
[24] J. R. Meyer, C. L. Felix, W. W. Bewley, I. Vurgaftman, E. H. Aifer, L. J. Olafsen, J. R. Lindle, C. A. Hoffman, M.-J. Yang, B. R. Bennett, B. V. Shanabrook, H. Lee, C.-H. Lin, S. S. Pei, and R. H. Miles, Appl. Phys. Lett. **73**, 2857 (1998).
[25] W. H. Knox, D. S. Chemla, D. A. B. Miller, J. B. Stark, and S. Schmitt-Rink, Phys. Rev. Lett. **62**, 1189 (1989).
[26] C. Sieh, T. Meier, A. Knorr, F. Jahnke, P. Thomas, and S. W. Koch, Eur. Phys. J. B **11**, 407 (1999).
[27] C. Sieh, T. Meier, F. Jahnke, A. Knorr, S. W. Koch, P. Brick, M. Hübner, C. Ell, J. Prineas, G. Khitrova, and H. M. Gibbs, Phys. Rev. Lett. **82**, 3112 (1999).
[28] S. W. Koch, C. Sieh, T. Meier, F. Jahnke, A. Knorr, P. Brick, M. Hübner, C. Ell, J. Prineas, G. Khitrova, and H. Gibbs, J. Lumin. **83-84**, 1 (1999).

[29] A. Trautmann, M. Stein, F. Schäfer, D. Anders, C. Ngo, J. T. Steiner, M. Reichelt, S. Chatterjee, and T. Meier, Proc. SPIE **12419**, 124190A (2023).
[30] M. Lindberg, Y. Z. Hu, R. Binder, and S. W. Koch, Phys. Rev. B **50**, 18060 (1994).
[31] V. M. Axt and A. Stahl, Z. Phys. B: Condens. Matter **93**, 195 (1994).
[32] V. M. Axt and A. Stahl, Z. Phys. B: Condens. Matter **93**, 205 (1994).
[33] W. Schäfer, D. S. Kim, J. Shah, T. C. Damen, J. E. Cunningham, K. W. Goossen, L. N. Pfeiffer, and K. Köhler, Phys. Rev. B **53**, 16429 (1996).
[34] H. Haug and S. W. Koch, *Quantum Theory of the Optical and Electronic Properties of Semiconductors*, 5th ed. (World Scientific, Singapore, 2009).
[35] T. Meier, P. Thomas, and S. W. Koch, *Coherent Semiconductor Optics: From Basic Concepts to Nanostructure Applications* (Springer, New York, 2007).
[36] S. Weiser, T. Meier, J. Möbius, A. Euteneuer, E. J. Mayer, W. Stolz, M. Hofmann, W. W. Rühle, P. Thomas, and S. W. Koch, Phys. Rev. B **61**, 13088 (2000).
[37] S. Chatterjee, C. Ell, S. Mosor, G. Khitrova, H. M. Gibbs, W. Hoyer, M. Kira, S. W. Koch, J. P. Prineas, and H. Stolz, Phys. Rev. Lett. **92**, 067402 (2004).
[38] W. Hoyer, C. Ell, M. Kira, S. W. Koch, S. Chatterjee, S. Mosor, G. Khitrova, H. M. Gibbs, and H. Stolz, Phys. Rev. B **72**, 075324 (2005).
[39] J. E. Sipe and E. Ghahramani, Phys. Rev. B **48**, 11705 (1993).
[40] P. Brick, C. Ell, S. Chatterjee, G. Khitrova, H. M. Gibbs, T. Meier, C. Sieh, and S. W. Koch, Phys. Rev. B **64**, 075323 (2001).
[41] N. S. Köster, K. Kolata, R. Woscholski, C. Lange, G. Isella, D. Chrastina, H. von Känel, and S. Chatterjee, Appl. Phys. Lett. **98**, 161103 (2011).

In preparation III - Rabi Splitting in Confined Semiconductors: $MoSe_2$ Monolayers vs. (Ga,In)As Quantum Wells

F. Schäfer, H. Mittenzwey, M. Stein, I. Müller, L. Greten, D. Anders, F. Dobener, M. Cuccu, C. Fuchs, K. Watanabe, T. Taniguchi, A. Chernikov, K. Volz, A. Knorr and S. Chatterjee

Abstract

Rabi splitting, a fundamental phenomenon in light-matter interaction, occurs when a two-level system is resonantly driven, creating doublets separated by the Rabi energy. We investigate the Rabi splitting dynamics in two paradigmatic 2D solid-state systems: a hBN-encapsulated $MoSe_2$ monolayer and a (Ga,In)As multiple quantum well structure. These systems show features beyond the Rabi splitting such as asymmetric Rabi oscillations in the time domain, the emergence of additional spectral resonances, and coherent gain. A microscopic theory based on Heisenberg equations of motion and an exciton expansion captures all observed phenomena and reveals the influence of many-body Coulomb correlations.

Contribution

I designed the setup with MS and SC, built it with MS as well as IM, and defined the requirements for the measurement software which was developed by FD. Measurements were conducted by me assisted by IM and MS. The experimental data were analyzed by me, and I created the graphical representations. The manuscript was written and improved in collaboration with HM, MS, DA, AC, AK, and SC.

Additional Publications as co-author

- "Exciton Dynamics Below Resonance: Unveiling Photon-Dressed Exciton States"

  Daniel Anders, Florian Dobener, **Felix Schäfer**, Sangam Chatterjee and Markus Stein submitted to *Physical Review Letters* (2025)

- "Inhibited Inelastic Scattering of Incoherent Excitons for Near-Band Edge Excitations", Ref. [80]

  Daniel Anders, Florian Dobener, **Felix Schäfer**, Sangam Chatterjee and Markus Stein in *Physical Review Letters* 132, 106901 (2024)

  `https://journals.aps.org/prl/abstract/10.1103/PhysRevLett.132.106901`

- "Experimental studies of the excitonic nonlinear response of GaAs-based type-I and type-II quantum well structures interacting with optical and terahertz fields", Ref. [150]

  Markus Stein, **Felix Schäfer**, Daniel Anders, Jan H. Littmann, Melanie Fey, Alexander Trautmann, Cong Ngo, Johannes T. Steiner, Matthias Reichelt, Christian Fuchs, Kerstin Volz, Torsten Meier and Sangam Chatterjee in *Proceedings Volume 12419, Ultrafast Phenomena and Nanophotonics XXVII*; 1241909 (2023)

  `https://spie.org/Publications/Proceedings/Paper/10.1117/12.2650291`

- "Analysis of the nonlinear optical response of excitons in type-I and type-II quantum wells including many-body correlations", Ref. [64]

  Alexander Trautmann, Markus Stein, **Felix Schäfer**, Daniel Anders, Cong Ngo, Johannes T. Steiner, Matthias Reichelt, Sangam Chatterjee and Torsten Meier in *Proceedings Volume 12419, Ultrafast Phenomena and Nanophotonics XXVII*; 1241909 (2023)

  `https://spie.org/Publications/Proceedings/Paper/10.1117/12.2650169`

- "Multiple pump-probe experiments reveal the ultrafast gain recovery in model active semiconductor media", Ref. [138]

  Felix Schäfer, Janine Lorenz, Markus Stein, Christian Fuchs, Kerstin Volz and Sangam Chatterjee in *Proceedings Volume 12415, Physics and Simulation of Optoelectronic Devices XXXI*; 1241504 (2023)

  `https://spie.org/Publications/Proceedings/Paper/10.1117/12.2650335`

- "Scalable high-repetition-rate sub-half-cycle terahertz pulses from spatially indirect interband transitions", Ref. [53]

  Christian Meineke, Michael Prager, Johannes Hayes, Qiannan Wen, Lukas Zheyi Kastner, Dieter Schuh, Kilian Fritsch, Oleg Pronin, Markus Stein, **Felix Schäfer**, Sangam Chatterjee, Mackillo Kira and Rupert Huber in *Light: Science & Applications* Volume 11, Article number: 151 (2022)

  `https://www.nature.com/articles/s41377-022-00824-6`

Bibliography

[1] Otfried Madelung. "Grundbegriffe der Halbleiterphysik". In: *Heidelberger Taschenbücher*. Springer Berlin Heidelberg, 1970. DOI: 10.1007/978-3-642-95158-9_1.

[2] A. H. Wilson. "The Theory of Electronic Semi-Conductors". In: *Proceedings of the Royal Society A: Mathematical, Physical and Engineering Sciences* 133.822 (1931), pp. 458–491. DOI: 10.1098/rspa.1931.0162.

[3] J. Bardeen and W. H. Brattain. "The Transistor, A Semi-Conductor Triode". In: *Physical Review* 74.2 (1948), pp. 230–231. DOI: 10.1103/physrev.74.230.

[4] W. Shockley and G. L. Pearson. "Modulation of Conductance of Thin Films of Semi-Conductors by Surface Charges". In: *Physical Review* 74.2 (1948), pp. 232–233. DOI: 10.1103/physrev.74.232.

[5] Rolf Sauer. *Halbleiterphysik*. Gruyter, Walter de GmbH, 2010. DOI: 10.1524/9783486598506.

[6] Gordon E. Moore. "Cramming more components onto integrated circuits, Reprinted from Electronics, volume 38, number 8, April 19, 1965, pp.114 ff." In: *IEEE Solid-State Circuits Society Newsletter* 11.3 (2006), pp. 33–35. DOI: 10.1109/n-ssc.2006.4785860.

[7] A. Y. Cho and J. R. Arthur. "Molecular beam epitaxy". In: *Progress in Solid State Chemistry* 10 (1975), pp. 157–191. DOI: 10.1016/0079-6786(75)90005-9.

[8] Marian A. Herman and Helmut Sitter. *Molecular Beam Epitaxy*. Springer Berlin Heidelberg, 1996. DOI: 10.1007/978-3-642-80060-3.

[9] Gerald B. Stringfellow. *Organometallic Vapor-Phase Epitaxy*. Elsevier Science, 1989. 398 pp. DOI: 10.1016/C2009-0-22261-6.

[10] Philippe Caroff et al. "High-Quality InAs/InSb Nanowire Heterostructures Grown by Metal–Organic Vapor-Phase Epitaxy". In: *Small* 4.7 (2008), pp. 878–882. DOI: 10.1002/smll.200700892.

[11] D. Spirkoska et al. "Structural and optical properties of high quality zinc-blende / wurtzite GaAs nanowire heterostructures". In: *Phys. Rev. B* 80.24 (2009). DOI: 10.1103/physrevb.80.245325.

[12] Katherine C. Phillips et al. "Ultrafast laser processing of materials: a review". In: *Advances in Optics and Photonics* 7.4 (2015), pp. 684–712. DOI: 10.1364/aop.7.000684.

[13] Mangirdas Malinauskas et al. "Ultrafast laser processing of materials: from science to industry". In: *Light: Science & Applications* 5.8 (2016), e16133–e16133. DOI: 10.1038/lsa.2016.133.

[14] Kendall E. Donaldson et al. "Femtosecond laser–assisted cataract surgery". In: *Journal of Cataract & Refractive Surgery* 39.11 (2013), pp. 1753–1763. DOI: 10.1016/j.jcrs.2013.09.002.

[15] Christopher L. Hoy et al. "Clinical ultrafast laser surgery: recent advances and future directions". In: *IEEE Journal of Selected Topics in Quantum Electronics* 20.2 (2013), pp. 242–255. DOI: 10.1109/jstqe.2013.2287098.

[16] Tobias J. Kippenberg, Ronald Holzwarth, and Scott A. Diddams. "Microresonator-based optical frequency combs". In: *Science* 332.6029 (2011), pp. 555–559. DOI: 10.1126/science.1193968.

[17] Aline S. Mayer, Cynthia R. Phillips, and Ursula Keller. "Watt-level 10-gigahertz solid-state laser enabled by self-defocusing nonlinearities in an aperiodically poled crystal". In: *Nature Communications* 8.1 (2017), pp. 1–8. DOI: 10.1038/s41467-017-01999-y.

[18] Jochen Schröder et al. "Laser frequency combs for coherent optical communications". In: *Journal of Lightwave Technology* 37.7 (2019), pp. 1663–1670. DOI: 10.1109/jlt.2019.2894170.

[19] Rudi Berera, Rienk van Grondelle, and John Kennis. "Ultrafast transient absorption spectroscopy: principles and application to photosynthetic systems". In: *Photosynthesis research* 101.2 (2009), pp. 105–118. DOI: 10.1007/s11120-009-9454-y.

[20] Margherita Maiuri, Marco Garavelli, and Giulio Cerullo. "Ultrafast spectroscopy: state of the art and open challenges". In: *Journal of the American Chemical Society* 142.1 (2019), pp. 3–15. DOI: 10.1021/jacs.9b10533.

[21] Hyunyong Choi et al. "Gain recovery dynamics and photon-driven transport in quantum cascade lasers". In: *Phys. Rev. Lett.* 100.16 (2008), p. 167401. DOI: 10.1103/physrevlett.100.167401.

[22] Niels Majer, Kathy Lüdge, and Eckehard Schöll. "Cascading enables ultrafast gain recovery dynamics of quantum dot semiconductor optical amplifiers". In: *Phys. Rev. B* 82.23 (2010), p. 235301. DOI: 10.1103/physrevb.82.235301.

[23] Jordi Gomis-Bresco et al. "Impact of Coulomb scattering on the ultrafast gain recovery in InGaAs quantum dots". In: *Phys. Rev. Lett.* 101.25 (2008), p. 256803. DOI: 10.1103/physrevlett.101.256803.

[24] Weng W. Chow and Stephan W. Koch. "Theory of semiconductor quantum-dot laser dynamics". In: *IEEE Journal of Quantum Electronics* 41.4 (2005), pp. 495–505. DOI: 10.1109/jqe.2005.843948.

[25] Tommy W. Berg et al. "Ultrafast gain recovery and modulation limitations in self-assembled quantum-dot devices". In: *IEEE Photonics Technology Letters* 13.6 (2001), pp. 541–543. DOI: 10.1109/68.924013.

[26] Aaron J. Zilkie et al. "Femtosecond gain and index dynamics in an InAs/InGaAsP quantum dot amplifier operating at 1.55 µm". In: *Optics Express* 14.23 (2006), pp. 11453–11459. DOI: 10.1364/oe.14.011453.

[27] K. Kim et al. "Gain dynamics and ultrafast spectral hole burning in In (Ga) As self-organized quantum dots". In: *Applied Physics Letters* 81.4 (2002), pp. 670–672. DOI: 10.1063/1.1493665.

[28] Bastian Herzog et al. "Fast gain and phase recovery of semiconductor optical amplifiers based on submonolayer quantum dots". In: *Applied Physics Letters* 107.20 (2015), p. 201102. DOI: 10.1063/1.4935792.

[29] Sabine Dommers et al. "Complete ground state gain recovery after ultrashort double pulses in quantum dot based semiconductor optical amplifier". In: *Applied Physics Letters* 90.3 (2007), p. 033508. DOI: 10.1063/1.2431789.

[30] Edik U. Rafailov, Maria Ana Cataluna, and Wilson Sibbett. "Mode-locked quantum-dot lasers". In: *Nature Photonics* 1.7 (2007), pp. 395–401. DOI: 10.1038/nphoton.2007.120.

[31] Aaron J. Zilkie et al. "Carrier Dynamics of Quantum-Dot, Quantum-Dash, and Quantum-Well Semiconductor Optical Amplifiers Operating at 1.55 µm". In: *IEEE*

Journal of Quantum Electronics 43.11 (2007), pp. 982–991. DOI: 10.1109/JQE.2007.904474.

[32] L. Zhang et al. "Reduced recovery time semiconductor optical amplifier using p-type-doped multiple quantum wells". In: *IEEE photonics technology letters* 18.22 (2006), pp. 2323–2325. DOI: 10.1109/lpt.2006.882225.

[33] G. Eisenstein et al. "Ultrafast gain dynamics in 1.5 µm multiple quantum well optical amplifiers". In: *Applied Physics Letters* 58.2 (1991), pp. 158–160. DOI: 10.1063/1.105237.

[34] Anne C. Tropper, Adrian H. Quarterman, and Keith G. Wilcox. "Ultrafast vertical-external-cavity surface-emitting semiconductor lasers". In: *Semiconductors and Semimetals*. Vol. 86. Elsevier, 2012, pp. 269–300. DOI: 10.1016/b978-0-12-391066-0.00007-1.

[35] Jeongsu Lee et al. "Mapping between quantum dot and quantum well lasers: From conventional to spin lasers". In: *Phys. Rev. B* 85.4 (2012), p. 045314. DOI: 10.1103/physrevb.85.045314.

[36] Adrian H. Quarterman et al. "A passively mode-locked external-cavity semiconductor laser emitting 60-fs pulses". In: *Nature Photonics* 3.12 (2009), pp. 729–731. DOI: 10.1038/nphoton.2009.216.

[37] Dominik Waldburger et al. "High-power 100 fs semiconductor disk lasers". In: *Optica* 3.8 (2016), pp. 844–852. DOI: 10.1364/optica.3.000844.

[38] Dirk Lorenser et al. "50-GHz passively mode-locked surface-emitting semiconductor laser with 100-mW average output power". In: *IEEE Journal of Quantum Electronics* 42.8 (2006), pp. 838–847. DOI: 10.1109/jqe.2006.878183.

[39] Mario Mangold et al. "Pulse repetition rate scaling from 5 to 100 GHz with a high-power semiconductor disk laser". In: *Optics Express* 22.5 (2014), pp. 6099–6107. DOI: 10.1364/oe.22.006099.

[40] M. Laemmlin et al. "Distortion-free optical amplification of 20-80 GHz modelocked laser pulses at 1.3 µm using quantum dots". In: *Electronics Letters* 42.12 (2006), p. 1. DOI: 10.1049/el:20061256.

[41] G. Fiol et al. "Hybrid mode-locking in a 40 GHz monolithic quantum dot laser". In: *Applied Physics Letters* 96.1 (2010), p. 011104. DOI: 10.1063/1.3279136.

[42] A. E. Zhukov, M. V. Maksimov, and A. R. Kovsh. "Device characteristics of long-wavelength lasers based on self-organized quantum dots". In: *Semiconductors* 46.10 (2012), pp. 1225–1250. DOI: 10.1134/s1063782612100223.

[43] C. Berger et al. "Novel type-II material system for laser applications in the near-infrared regime". In: *Aip Advances* 5.4 (2015), p. 047105. DOI: 10.1063/1.4917180.

[44] C. Möller et al. "Type-II vertical-external-cavity surface-emitting laser with Watt level output powers at 1.2 µm". In: *Applied Physics Letters* 108.7 (2016), p. 071102. DOI: 10.1063/1.4942103.

[45] Christian Fuchs et al. "Temperature-dependent spectral properties of (GaIn) As/Ga (AsSb)/(GaIn) As W-quantum well heterostructure lasers". In: *arXiv preprint* (2020). DOI: 10.48550/arXiv.2012.01522.

[46] I. Kilen et al. "Mode-locking in vertical external-cavity surface-emitting lasers with type-II quantum-well configurations". In: *Applied Physics Letters* 114.25 (2019), p. 252102. DOI: 10.1063/1.5098903.

[47] J. Shah. *Ultrafast Spectroscopy of Semiconductors and Semiconductor Nanostructures*. Springer Series in Solid-State Sciences. Springer Berlin Heidelberg, 2013. ISBN: 9783662037706. DOI: 10.1007/978-3-662-03299-2.

[48] Jai Singh. *Optical properties of condensed matter and applications*. Vol. 6. John Wiley & Sons, 2006. DOI: 10.1002/0470021942.

[49] S. Schmitt-Rink, D. S. Chemla, and David A. B. Miller. "Linear and nonlinear optical properties of semiconductor quantum wells". In: *Advances in Physics* 38.2 (1989), pp. 89–188. DOI: 10.1080/00018738900101102.

[50] A. Von Lehmen et al. "Optical Stark effect on excitons in GaAs quantum wells". In: *Optics Letters* 11.10 (1986), pp. 609–611. DOI: 10.1364/ol.11.000609.

[51] Yu-Hsuan Kuo et al. "Strong quantum-confined Stark effect in germanium quantum-well structures on silicon". In: *Nature* 437.7063 (2005), pp. 1334–1336. DOI: 10.1038/nature04204.

[52] M. Stein et al. "Dynamics of charge-transfer excitons in type-II semiconductor heterostructures". In: *Phys. Rev. B* 97.12 (12 2018), p. 125306. DOI: 10.1103/physrevb.97.125306.

[53] Christian Meineke et al. "Scalable high-repetition-rate sub-half-cycle terahertz pulses from spatially indirect interband transitions". In: *Light: Science & Applications* 11.1 (May 2022). ISSN: 2047-7538. DOI: 10.1038/s41377-022-00824-6.

[54] M. Fey et al. "Phase relaxation control in heterostructures featuring charge-transfer excitons". In: *Phys. Rev. B* 106 (16 2022), p. 165303. DOI: 10.1103/physrevb.106.165303.

[55] F. Schäfer et al. "Gain recovery dynamics in active type-II semiconductor heterostructures". In: *Applied Physics Letters* 122.8 (2023). DOI: 10.1063/5.0128777.

[56] Christian Lammers et al. "Gain spectroscopy of a type-II VECSEL chip". In: *Applied Physics Letters* 109.23 (2016), p. 232107. DOI: 10.1063/1.4971333.

[57] Georgy G. Zegrya and Aleksey D. Andreev. "Mechanism of suppression of Auger recombination processes in type-II heterostructures". In: *Applied Physics Letters* 67.18 (1995), pp. 2681–2683. DOI: 10.1063/1.114291.

[58] J. I. Malin et al. "Type II mid-infrared quantum well lasers". In: *Applied Physics Letters* 68.21 (1996), pp. 2976–2978. DOI: 10.1063/1.116374.

[59] J. R. Meyer et al. "Auger coefficients in type-II InAs/Ga 1- x In x Sb quantum wells". In: *Applied Physics Letters* 73.20 (1998), pp. 2857–2859. DOI: 10.1063/1.122609.

[60] W. H. Knox et al. "Femtosecond ac Stark effect in semiconductor quantum wells: Extreme low-and high-intensity limits". In: *Phys. Rev. Lett.* 62.10 (1989), p. 1189. DOI: 10.1103/PhysRevLett.62.1189.

[61] C. Sieh et al. "Influence of carrier correlations on the excitonic optical response including disorder and microcavity effects". In: *Eur. Phys. J. B* 11.3 (1999), p. 407. ISSN: 1434-6036. DOI: 10.1007/BF03219177.

[62] C. Sieh et al. "Coulomb Memory Signatures in the Excitonic Optical Stark Effect". In: *Phys. Rev. Lett.* 82 (15 1999), p. 3112. DOI: 10.1103/PhysRevLett.82.3112.

[63] S. W. Koch et al. "Theory of coherent effects in semiconductors". In: *J. Lumin* 83 (1999), p. 1. ISSN: 0022-2313. DOI: 10.1016/s0022-2313(99)00065-4.

[64] A. Trautmann et al. "Analysis of the nonlinear optical response of excitons in type-I and type-II quantum wells including many-body correlations". In: *Ultrafast Phenomena and Nanophotonics XXVII*. Vol. 12419. International Society for Optics and Photonics. SPIE, Mar. 2023, 124190A. DOI: 10.1117/12.2650169.

[65] D. A. B. Miller et al. "Band-edge electroabsorption in quantum well structures: The quantum-confined Stark effect". In: *Phys. Rev. Lett.* 53.22 (1984), p. 2173. DOI: 10.1103/physrevlett.53.2173.

[66] M. Stepanenko, I. Kulinich, and I. Yunusov. "Optimization of RF electrodes for electro-optic modulator based on quantum-confined Stark effect". In: *Journal of Physics: Conference Series*. Vol. 1145. IOP Publishing. 2019, p. 012028. DOI: 10.1088/1742-6596/1145/1/012028.

[67] Hiroaki Yamamoto, Masahiro Asada, and Yasuharu Suematsu. "Theory of refractive index variation in quantum well structure and related intersectional optical switch". In: *Journal of lightwave technology* 6.12 (1988), pp. 1831–1840. DOI: 10.1109/50.9252.

[68] Takuya Aizawa et al. "Polarization-independent quantum-confined stark effect in an InGaAs/InP tensile-strained quantum well". In: *IEEE Journal of Quantum Electronics* 30.2 (1994), pp. 585–592. DOI: 10.1109/3.283807.

[69] Adriano Barenco et al. "Conditional quantum dynamics and logic gates". In: *Phys. Rev. Lett.* 74.20 (1995), p. 4083. DOI: 10.1103/physrevlett.74.4083.

[70] Mark A. Kasevich. "Coherence with atoms". In: *Science* 298.5597 (2002), pp. 1363–1368. DOI: 10.1126/science.1079430.

[71] Annkatrin Sommer et al. "Attosecond nonlinear polarization and light–matter energy transfer in solids". In: *Nature* 534.7605 (2016), pp. 86–90. DOI: 10.1038/nature17650.

[72] Aviv Karnieli et al. "The coherence of light is fundamentally tied to the quantum coherence of the emitting particle". In: *Science Advances* 7.18 (2021). DOI: 10.1126/sciadv.abf8096.

[73] S. H. Autler and C. H. Townes. "Stark effect in rapidly varying fields". In: *Physical Review* 100.2 (1955), p. 703. DOI: 10.1103/PhysRev.100.703.

[74] A. M. Bonch-Bruevich et al. "Changes in the atomic absorption spectrum in the field of a light wave I". In: *Sov. Phys. JETP* 29.1 (1969), pp. 82–85.

[75] A. Mysyrowicz et al. ""Dressed excitons" in a multiple-quantum-well structure: evidence for an optical Stark effect with femtosecond response time". In: *Phys. Rev. Lett.* 56.25 (1986), p. 2748. DOI: 10.1103/PhysRevLett.56.2748.

[76] F. Schäfer et al. "Optical Stark effect in type-II semiconductor heterostructures". In: *Phys. Rev. B* 109.7 (Feb. 2024), p. 075301. ISSN: 2469-9969. DOI: 10.1103/physrevb.109.075301.

[77] Michele Saba et al. "Direct observation of the excitonic ac Stark splitting in a quantum well". In: *Phys. Rev. B* 62 (24 2000), R16322–R16325. DOI: 10.1103/PhysRevB.62.R16322.

[78] Hailin Wang et al. "Transient nonlinear optical response from excitation induced dephasing in GaAs". In: *Phys. Rev. Lett.* 71.8 (1993), p. 1261. DOI: 10.1103/PhysRevLett.71.1261.

[79] Florian Katsch, Malte Selig, and Andreas Knorr. "Exciton-scattering-induced dephasing in two-dimensional semiconductors". In: *Phys. Rev. Lett.* 124.25 (2020), p. 257402. DOI: 10.1103/PhysRevLett.124.257402.

[80] D. Anders et al. "Inhibited Inelastic Scattering of Incoherent Excitons for Near-Band Edge Excitations". In: *Phys. Rev. Lett.* 132 (10 2024), p. 106901. DOI: 10.1103/PhysRevLett.132.106901.

[81] F. Quochi et al. "Strongly Driven Semiconductor Microcavities: From the Polariton Doublet to an ac Stark Triplet". In: *Phys. Rev. Lett.* 80 (21 1998), pp. 4733–4736. DOI: 10.1103/PhysRevLett.80.4733.

[82] Francesco Quochi et al. "Direct observation of an ac Stark splitting in semiconductor microcavities excited above the continuum onset". In: *Phys. Rev. B* 61.8 (2000), R5113. DOI: 10.1103/PhysRevB.61.R5113.

[83] A. Schülzgen et al. "Direct observation of excitonic Rabi oscillations in semiconductors". In: *Phys. Rev. Lett.* 82.11 (1999), p. 2346. DOI: 10.1103/PhysRevLett.82.2346.

[84] J. F. Dynes et al. "ac Stark Splitting and Quantum Interference with Intersubband Transitions in Quantum Wells". In: *Phys. Rev. Lett.* 94.15 (2005), p. 157403. DOI: 10.1103/PhysRevLett.94.157403.

[85] Mark D. Frogley et al. "Gain without inversion in semiconductor nanostructures". In: *Nature Materials* 5.3 (2006), pp. 175–178. DOI: 10.1038/nmat1586.

[86] Martin Wagner et al. "Observation of the intraexciton Autler-Townes effect in GaAs/AlGaAs semiconductor quantum wells". In: *Phys. Rev. Lett.* 105.16 (2010), p. 167401. DOI: 10.1103/PhysRevLett.105.167401.

[87] B. Ewers et al. "Ionization of coherent excitons by strong terahertz fields". In: *Phys. Rev. B* 85.7 (2012), p. 075307. DOI: 10.1103/PhysRevB.85.075307.

[88] M. Teich et al. "Semiconductor quantum well excitons in strong, narrowband terahertz fields". In: *New Journal of Physics* 15.6 (2013), p. 065007. DOI: 10.1088/1367-2630/15/6/065007.

[89] M. Teich et al. "Systematic investigation of terahertz-induced excitonic Rabi splitting". In: *Phys. Rev. B* 89.11 (2014), p. 115311. DOI: 10.1103/PhysRevB.89.115311.

[90] Niko S. Köster et al. "Controlling the polarization dynamics by strong THz fields in photoexcited germanium quantum wells". In: *New Journal of Physics* 15.7 (2013), p. 075004. DOI: 10.1088/1367-2630/15/7/075004.

[91] Shaojun Wang et al. "Coherent coupling of WS2 monolayers with metallic photonic nanostructures at room temperature". In: *Nano Letters* 16.7 (2016), pp. 4368–4374. DOI: 10.1021/acs.nanolett.6b01475.

[92] Di Zheng et al. "Manipulating coherent plasmon–exciton interaction in a single silver nanorod on monolayer WSe2". In: *Nano Letters* 17.6 (2017), pp. 3809–3814. DOI: 10.1021/acs.nanolett.7b01176.

[93] Xiaobo Han et al. "Rabi splitting in a plasmonic nanocavity coupled to a WS2 monolayer at room temperature". In: *ACS Photonics* 5.10 (2018), pp. 3970–3976. DOI: 10.1021/acsphotonics.8b00931.

[94] Mingsong Wang et al. "Tunable fano resonance and plasmon–exciton coupling in single au nanotriangles on monolayer WS2 at room temperature". In: *Advanced Materials* 30.22 (2018), p. 1705779. DOI: 10.1002/adma.201705779.

[95] Bowen Li et al. "Large Rabi splitting obtained in Ag-WS2 strong-coupling heterostructure with optical microcavity at room temperature". In: *Opto-Electronic Advances* 2.5 (2019), p. 190008. DOI: 10.29026/oea.2019.190008.

[96] Min Zhang et al. "Observation of ultra-large Rabi splitting in the plasmon-exciton polaritons at room temperature". In: *Nanophotonics* 12.16 (2023), pp. 3267–3275. DOI: 10.1515/nanoph-2023-0162.

[97] Chaw-Keong Yong et al. "Valley-dependent exciton fine structure and Autler–Townes doublets from Berry phases in monolayer MoSe2". In: *Nature Materials* 18.10 (2019), pp. 1065–1070. DOI: 10.1038/s41563-019-0447-8.

[98] Rudolf Huebener. *Leiter, Halbleiter, Supraleiter - Eine Einführung in die Festkörperphysik*. Springer Berlin Heidelberg, 2013. DOI: 10.1007/978-3-642-34879-2.

[99] Charles Kittel. *Introduction to solid state physics*. Wiley, 2005, p. 680. ISBN: 047141526X.

[100] K.-H. Hellwege. *Einführung in die Festkörperphysik*. Springer Berlin Heidelberg, 1976. ISBN: 9783642963018. DOI: 10.1007/978-3-642-96301-8.

[101] Babu V. Suresh. *Solid State Devices And Technology*. Pearson Education India, 2010.

[102] Peter Y. Yu and Manuel Cardona. *Fundamentals of Semiconductors*. Springer Berlin Heidelberg, 2010. DOI: 10.1007/978-3-642-00710-1.

[103] Marian A. Herman, Wolfgang Richter, and Helmut Sitter. *Epitaxy*. Springer Berlin Heidelberg, 2004. DOI: 10.1007/978-3-662-07064-2.

[104] M. Stein. "Ladungsträgerdynamik in räumliche indirekten Halbleiterheterostruktur". Masterarbeit. Philipps-Universität Marburg, 2015.

[105] E. Schrödinger. "Quantisierung als Eigenwertproblem". In: *Annalen der Physik* 385.13 (1926), pp. 437–490. DOI: 10.1002/andp.19263851302.

[106] D. A. B. Miller. "Optical Physics of Quantum Wells". In: *Quantum Dynamics of Simple Systems* (1996). URL: https://ee.stanford.edu/~dabm/181.pdf.

[107] Markus Stein et al. "Direct Probe of Room-Temperature Quantum-Tunneling Processes in Type-II Heterostructures Using Terahertz Emission Spectroscopy". In: *Phys. Rev. Appl.* 13 (5 2020), p. 054073. DOI: 10.1103/PhysRevApplied.13.054073.

[108] Manish Chhowalla et al. "The chemistry of two-dimensional layered transition metal dichalcogenide nanosheets". In: *Nature Chemistry* 5.4 (Mar. 2013), pp. 263–275. ISSN: 1755-4349. DOI: 10.1038/nchem.1589.

[109] Andrea Splendiani et al. "Emerging Photoluminescence in Monolayer MoS2". In: *Nano Letters* 10.4 (Mar. 2010), pp. 1271–1275. ISSN: 1530-6992. DOI: 10.1021/nl903868w.

[110] B. Radisavljevic et al. "Single-layer MoS2 transistors". In: *Nature Nanotechnology* 6.3 (Jan. 2011), pp. 147–150. ISSN: 1748-3395. DOI: 10.1038/nnano.2010.279.

[111] Won Seok Yun et al. "Thickness and strain effects on electronic structures of transition metal dichalcogenides: 2H-MX_2 semiconductors (M = Mo, W; x = S, Se, Te)". In: *Physical Review B* 85.3 (Jan. 2012), p. 033305. ISSN: 1550-235X. DOI: 10.1103/physrevb.85.033305.

[112] Claudia Ruppert, Burak Aslan, and Tony F. Heinz. "Optical Properties and Band Gap of Single- and Few-Layer MoTe2 Crystals". In: *Nano Letters* 14.11 (Oct. 2014), pp. 6231–6236. ISSN: 1530-6992. DOI: 10.1021/nl502557g.

[113] Qing Hua Wang et al. "Electronics and optoelectronics of two-dimensional transition metal dichalcogenides". In: *Nature Nanotechnology* 7.11 (Nov. 2012), pp. 699–712. ISSN: 1748-3395. DOI: 10.1038/nnano.2012.193.

[114] Michelle Saliba et al. "Molybdenum disulfide, exfoliation methods and applications to photocatalysis: a review". In: *Nanoscale Advances* 5.24 (2023), pp. 6787–6803. ISSN: 2516-0230. DOI: 10.1039/d3na00741c.

[115] Xingli Wang et al. "Chemical Vapor Deposition Growth of Crystalline Monolayer MoSe2". In: *ACS Nano* 8.5 (Apr. 2014), pp. 5125–5131. ISSN: 1936-086X. DOI: 10.1021/nn501175k.

[116] S. Cincotti and J. P. Rabe. "Self-assembled alkane monolayers on MoSe2 and MoS2". In: *Applied Physics Letters* 62.26 (June 1993), pp. 3531–3533. ISSN: 1077-3118. DOI: 10.1063/1.109017.

[117] Sefaattin Tongay et al. "Thermally Driven Crossover from Indirect toward Direct Bandgap in 2D Semiconductors: MoSe2 versus MoS2". In: *Nano Letters* 12.11 (Oct. 2012), pp. 5576–5580. ISSN: 1530-6992. DOI: 10.1021/nl302584w.

[118] Zhonghui Nie et al. "Broadband nonlinear optical response of monolayer MoSe2 under ultrafast excitation". In: *Applied Physics Letters* 112.3 (Jan. 2018). ISSN: 1077-3118. DOI: 10.1063/1.5010060.

[119] K. S. Novoselov et al. "Electric Field Effect in Atomically Thin Carbon Films". In: *Science* 306.5696 (Oct. 2004), pp. 666–669. ISSN: 1095-9203. DOI: 10.1126/science.1102896.

[120] Sajedeh Manzeli et al. "2D transition metal dichalcogenides". In: *Nature Reviews Materials* 2.8 (June 2017). ISSN: 2058-8437. DOI: 10.1038/natrevmats.2017.33.

[121] Eugene Hecht. *Optics, Global Edition*. Pearson Higher Education & Professional Group, 2016, p. 704. ISBN: 9781292096933.

[122] Wolfgang Demtröder. *Experimentalphysik 3*. Springer Berlin Heidelberg, 2016. ISBN: 9783662490945. DOI: 10.1007/978-3-662-49094-5.

[123] S. B. Nam et al. "Free-exciton energy spectrum in GaAs". In: *Phys. Rev. B* 13.2 (1976), pp. 761–767. DOI: 10.1103/physrevb.13.761.

[124] W. Shockley and W. T. Read. "Statistics of the Recombinations of Holes and Electrons". In: *Physical Review* 87.5 (1952), pp. 835–842. DOI: 10.1103/physrev.87.835.

[125] Ulrich Platt and Jochen Stutz. *Differential Optical Absorption Spectroscopy. Principles and Applications (Physics of Earth and Space Environments)*. Springer, 2008, p. 605. ISBN: 9783540211938.

[126] S. Arlt et al. "Ultrafast dephasing of continuum transitions in bulk semiconductors". In: *Phys. Rev. B* 59.23 (1999), pp. 14860–14863. DOI: 10.1103/physrevb.59.14860.

[127] Jagdeep Shah, ed. *Hot Carriers in Semiconductor Nanostructures*. Elsevier, 1992. ISBN: 978-0-12-638140-5. DOI: 10.1016/c2009-0-22204-5.

[128] Anthony E. Siegman. *Lasers*. University Science Books, 1990. ISBN: 9780935702118.

[129] Peter W. Milonni. *Lasers Physics*. John Wiley & Sons, 2010. ISBN: 9780470387719.

[130] Ansheng Liu. "Rabi splitting of the optical intersubband absorption line of multiple quantum wellsinside a Fabry-Pérot microcavity". In: *Physical Review B* 55.11 (Mar. 1997), pp. 7101–7109. ISSN: 1095-3795. DOI: 10.1103/physrevb.55.7101.

[131] G. Khitrova et al. "Vacuum Rabi splitting in semiconductors". In: *Nature Physics* 2.2 (Feb. 2006), pp. 81–90. ISSN: 1745-2481. DOI: 10.1038/nphys227.

[132] Sebastian Unsleber et al. "Observation of resonance fluorescence and the Mollow triplet from a coherently driven site-controlled quantum dot". In: *Optica* 2.12 (2015), p. 1072. ISSN: 2334-2536. DOI: 10.1364/optica.2.001072.

[133] B. Fluegel et al. "Femtosecond Studies of Coherent Transients in Semiconductors". In: *Physical Review Letters* 59.22 (Nov. 1987), pp. 2588–2591. ISSN: 0031-9007. DOI: 10.1103/physrevlett.59.2588.

[134] J. P. Sokoloff et al. "Transient oscillations in the vicinity of excitons and in the band of semiconductors". In: *Physical Review B* 38.11 (Oct. 1988), pp. 7615–7621. ISSN: 0163-1829. DOI: 10.1103/physrevb.38.7615.

[135] Peter Brick. *Coherent optical nonlinearities in semiconductor microstructures*. 2001. URL: http://hdl.handle.net/10150/280073.

[136] M. Stein, F. Schäfer, and L. Gomell. "Inelastic electron-exciton scattering in bulk germanium". In: *Phys. Rev. B* 99.14 (Apr. 2019), p. 144310. ISSN: 2469-9969. DOI: 10.1103/physrevb.99.144310.

[137] Markus Stein. *Dynamics of Excitons in Semiconductors*. Philipps-Universität Marburg, 2019. DOI: 10.17192/Z2019.0513.

[138] F. Schäfer et al. "Multiple pump-probe experiments reveal the ultrafast gain recovery in model active semiconductor media". In: *Physics and Simulation of Optoelectronic Devices XXXI*. Vol. 12415. International Society for Optics and Photonics. SPIE, 2023, p. 1241504. DOI: 10.1117/12.2650335.

[139] Max Born et al. *Principles of Optics: Electromagnetic Theory of Propagation, Interference and Diffraction of Light*. Cambridge University Press, 1999. ISBN: 9781139644181. DOI: 10.1017/cbo9781139644181.

[140] M. Stein et al. "Enhanced Absorption by Linewidth Narrowing in Optically Excited Type-II Semiconductor Heterostructures". In: *Phys. Rev. Lett.* 121 (1 2018), p. 017401. DOI: 10.1103/PhysRevLett.121.017401.

[141] K. L. Shaklee and R. F. Leheny. "DIRECT DETERMINATION OF OPTICAL GAIN IN SEMICONDUCTOR CRYSTALS". In: *Applied Physics Letters* 18.11 (Oct. 2003), pp. 475–477. ISSN: 0003-6951. DOI: 10.1063/1.1653501.

[142] Basil W. Hakki and Thomas L. Paoli. "cw degradation at 300°K of GaAs double-heterostructure junction lasers. II. Electronic gain". In: *Journal of Applied Physics* 44.9 (1973), pp. 4113–4119. DOI: 10.1063/1.1662905.

[143] C. Cohen-Tannoudji, G. Grynberg, and J. Dupont-Roc. *Atom-Photon Interactions: Basic Processes and Applications*. New York: Wiley, 1992.

[144] C. Ciuti et al. "Strongly Driven Exciton Resonances in Quantum Wells: Light-Induced Dressing versus Coulomb Scattering". In: *Phys. Rev. Lett.* 84 (8 2000), pp. 1752–1755. DOI: 10.1103/PhysRevLett.84.1752.

[145] V. I. Donin, D. V. Yakovin, and A. V. Gribanov. "Diode-pumped green Nd:YAG laser with Q-switch and mode locking". In: *Optics Letters* 37.3 (Jan. 2012), p. 338. ISSN: 1539-4794. DOI: 10.1364/ol.37.000338.

[146] S. J. Boyle et al. "Beating of Exciton-Dressed States in a Single Semiconductor InGaAs/GaAs Quantum Dot". In: *Physical Review Letters* 102.20 (May 2009), p. 207401. ISSN: 1079-7114. DOI: 10.1103/physrevlett.102.207401.

[147] S Anghel et al. "Coupled exciton-trion spin dynamics in a MoSe 2 monolayer". In: *2D Materials* 5.4 (2018), p. 045024. ISSN: 2053-1583. DOI: 10.1088/2053-1583/aadbd8.

[148] G. Wang et al. "Polarization and time-resolved photoluminescence spectroscopy of excitons in MoSe2 monolayers". In: *Applied Physics Letters* 106.11 (2015). ISSN: 1077-3118. DOI: 10.1063/1.4916089.

[149] Fabian Cadiz et al. "Ultra-low power threshold for laser induced changes in optical properties of 2D molybdenum dichalcogenides". In: *2D Materials* 3.4 (2016), p. 045008. ISSN: 2053-1583. DOI: 10.1088/2053-1583/3/4/045008.

[150] M. Stein et al. "Experimental studies of the excitonic nonlinear response of GaAs-based type I and type II quantum well structures interacting with optical and terahertz fields". In: *Ultrafast Phenomena and Nanophotonics XXVII*. SPIE, Mar. 2023. DOI: 10.1117/12.2650291.

Selbstständigkeitserklärung

Ich erkläre:

Ich habe die vorgelegte Dissertation selbstständig und ohne unerlaubte fremde Hilfe und nur mit den Hilfen angefertigt, die ich in der Dissertation angegeben habe. Alle Textstellen, die wörtlich oder sinngemäß aus veröffentlichten Schriften entnommen sind, und alle Angaben, die auf mündlichen Auskünften beruhen, sind als solche kenntlich gemacht. Ich stimme einer evtl. Überprüfung meiner Dissertation durch eine Antiplagiat-Software zu. Bei den von mir durchgeführten und in der Dissertation erwähnten Untersuchungen habe ich die Grundsätze guter wissenschaftlicher Praxis, wie sie in der „Satzung der Justus-Liebig-Universität Gießen zur Sicherung guter wissenschaftlicher Praxis“ niedergelegt sind, eingehalten.

Gießen, 11.12.2025

Felix Schäfer

Danksagung

Ich möchte allen danken, die diese Dissertation ermöglicht haben. Zunächst gilt mein Dank meinem Betreuer, Prof. Dr. Sangam Chatterjee, der mich in die Arbeitsgruppe aufgenommen und von Anfang an großes Vertrauen in mich gesetzt hat. Ebenso danke ich der Zweitgutachterin, Prof. Dr. Marina Gerhard, für die Übernahme der Bewertung dieser Arbeit. Mein Dank geht zudem an den restlichen Prüfungsausschuss: Prof. Dr. Torsten Meier, der die theoretischen Berechnungen zu den beiden veröffentlichten Papers betreut hat, sowie PD Dr. Mattias Elm, der sich bereit erklärt hat, als weiterer Prüfer zu agieren.

Ein herzlicher Dank gilt allen Mitarbeitenden und Ehemaligen der AG Spektroskopie und Optik, die ich während meiner Zeit dort kennenlernen durfte, insbesondere meinen Bürokollegen Daniel Anders, Lukas Gümbel und Marius Müller, mit denen ich die täglichen Herausforderungen und Traditionen genossen habe und auch abseits der Arbeit gemeinsame Unternehmungen und Zeit verbracht habe.

Ich danke Dr. Markus Stein für seine stetige Bereitschaft, all meine Fragen zu beantworten, beim Aufbau der Experimente zu unterstützen, gemeinsame Messsessions durchzuführen, wertvolle Tipps bei der Auswertung zu geben und beim Schreiben der Papers zu helfen. Ebenso danke ich Dr. Florian Dobener für die Programmierung und Anpassung der LabVIEW-Programme sowie der Messroutinen, ohne die die Durchführung meiner Messungen nicht möglich gewesen wäre.

Dank gebührt auch meinen ehemaligen Kommilitonen Dr. Melanie Fey, Patrick Gebhard, Max Vaupel, Dr. David Leimbach und Nils Mengel, mit denen ich mein Studium absolviert habe. Ihre Unterstützung, ihre konstruktiven Anmerkungen und ihr hilfreiches Feedback zu dieser Arbeit waren von unschätzbarem Wert.

Ein weiterer Dank geht an das gesamte Organisationsteam, insbesondere an die Sekretärinnen Daniela Musaeus und Anja Denhardt, die mir im bürokratischen Dschungel den Weg gewiesen und unzählige Bestellungen für mich durchgeführt haben. Mein Dank gilt ebenfalls der Heliumbeschaffung, die die hunderten Stunden an Experimenten bei 4 K ermöglicht hat, sowie der Feinmechanik- und Elektronikwerkstatt, die stets Probleme mit der Hardware des Aufbaus beheben konnte.

Ich danke auch den Bachelor- und Masterstudierenden, die ich betreut habe und von denen ich wertvolles Feedback erhalten habe. Ich hoffe, ich konnte ihnen den Umgang im Labor, die Datenanalyse und die Vorteile von Vektorgrafiken anschaulich vermitteln.

Abschließend möchte ich meinen Eltern danken, die mir all dies ermöglicht haben und immer hinter mir standen – bei jeder Entscheidung – sowie für ihr Verständnis, wenn ich nicht so oft zu Besuch in der Heimat war.